

**COLOSSAL PERMITTIVITY AND LOW DIELECTRIC LOSS  
OF  $\text{LaAl}_{0.67-x}\text{Ca}_x\text{Mn}_{0.33}\text{O}_3$  CERAMICS**

*A Dissertation Submitted to the Department Of Physics,  
Bangladesh University of Engineering & Technology, Dhaka, in  
Partial Fulfillment of the Requirement for the Degree of Master of Science  
(M. Sc.) in Physics*

**SUBMITTED**

**By**

**MD. ABDULLAH AL NOMAN**

**STUDENT NO. : 1017142513**

**SESSION : October, 2017**



**DEPARTMENT OF PHYSICS  
BANGLADESH UNIVERSITY OF ENGINEERING & TECHNOLOGY  
DHAKA 1000, BANGLADESH**

# CANDIDATE'S DECLARATION

BANGLADESH UNIVERSITY OF ENGINEERING & TECHNOLOGY (BUET), DHAKA  
DEPARTMENT OF PHYSICS



## *Certification of Thesis*

The thesis titled “**COLOSSAL PERMITTIVITY AND LOW DIELECTRIC LOSS OF  $\text{LaAl}_{0.67-x}\text{Ca}_x\text{Mn}_{0.33}\text{O}_3$  CERAMICS**” submitted by **MD. ABDULLAH AL NOMAN** Roll No. 1017142513F, Session: October/2017, has been accepted as satisfactory in partial fulfillment of the requirement for the degree of **Masters of Science (M.Sc.)** in Physics on 20 November, 2019.

## BOARD OF EXAMINERS

*A. Hossain*

**Dr. A. K. M. Akther Hossain** (Supervisor)  
Professor  
Department of Physics, BUET, Dhaka

Chairman

*Dr. Md. Forhad Mina*

**Dr. Md. Forhad Mina**  
Professor and Head  
Department of Physics, BUET, Dhaka-1000

Member (Ex-Officio)

**Dr. Md. Feroz Alam Khan**  
Professor  
Department of Physics, BUET, Dhaka-1000

Member

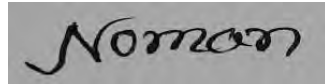
**Dr. Mohammad Khurshed Alam**  
Assistant Professor  
Department of Physics, BUET, Dhaka-1000

Member

**Dr. Khandker Saadat Hossain**  
Professor  
Department of Physics  
University of Dhaka, Dhaka-1000

Member (External)

It is hereby declared that this thesis or any part of it has not been submitted elsewhere for the award of any degree or diploma.



---

**MD. ABDULLAH AL NOMAN**

*DEDICATED TO  
MY  
PARENTS*

## **ACKNOWLEDGEMENTS**

*First of all, I express all my admiration and devotion to the almighty Allah, the most beneficent who has enabled me to perform this research work and to submit this thesis.*

*I express my profound gratitude to my honorable supervisor Prof. Dr. A.K.M. Akther Hossain, Department of Physics, Bangladesh University of Engineering and Technology (BUET), for his constant direction, constructive criticism and inspiration in pursuing the whole investigation of the present research. Words are always insufficient to express his working capacities and unending enthusiasm for scientific rigorousness for innovative investigations. This always becomes the everlasting source of inspiration for his students.*

*I am extremely grateful to Prof. Dr. Md. Forhad Mina, Head, Department of Physics, BUET, for kindly permitting me to carry out this research in the Physics Lab. and to the BUET authorities for providing the necessary financial grant for the research.*

*I would like to express my gratitude to Prof. Dr. Jiban Podder, Prof. Dr. Md. Feroz Alam Khan, Mrs. Fahima Khanam, Prof. Dr. Md. Mostak Hossain, Prof. Dr. Md. Rafi Uddin, Prof. Dr. Nasreen Akter, Prof. Dr. Mohammed Abdul Basith, Dr. Mohammad Jellur Rahman, Dr. Mohammad Abu Sayem Karal, Dr. Muhammad Samir Ullah, Dr. Md. Azizar Rahman, Dr. Muhammad Rakibul Islam and all other teachers of Department of Physics, BUET for their sincere cooperation. I would also like to convey my thanks to the employees of the Department of Physics, BUET for their co-operation.*

*I am very much thankful to Mithun Kumar Das, Assistant Professor, Department of Physics, Comilla University, Abdulla Al-Momin, Assistant Professor, Department of Physics, Jagannat University, Bablu Chandra Das, Assistant Professor, Nila Rani Kundu, Senior Scientific Officer, Md. Harun-Or-Rashid, Assistant Professor, Moiful Alam, Assistant Professor, Roksana Pervin, Md. Zahidur Rahaman, Md. Mehedi Hasan and all other members of solid state physics laboratory, BUET for their support, advice and assistance throughout the whole research work.*

*Finally, I would mention a very special gratefulness for the moral support and sustaining inspiration provided by the members of my family. This dissertation would never have been possible without their love and affection.*

***The Author***

***Md. Abdullah Al Noman***

## ABSTRACT

The exploration of colossal dielectric permittivity materials with low dielectric loss in a wide range of frequencies continues to attract considerable interest. The compounds with a colossal dielectric permittivity have attracted a lot of attention because of their applications in high-energy density storage and microelectronics as a result of the continually increasing demands of microelectronics applications. Ca and Mn co-doped  $\text{LaAl}_{0.67-x}\text{Ca}_x\text{Mn}_{0.33}\text{O}_3$  ( $x = 0.00, 0.02, 0.04, 0.05$ ) ceramics were prepared by a solid-state reaction method. Pellet shaped samples prepared from each composition were sintered at 1723 K for 5 h. X-ray diffraction (XRD) and Field Emission Scanning Electron Microscope (FESEM) are used to carry out the structural and surface morphology analyses. The dielectric constant ( $\epsilon'$ ), dielectric loss ( $\tan\delta_E$ ), ac-conductivity ( $\sigma_{ac}$ ) and complex impedance spectra analysis of the  $\text{LaAl}_{0.67-x}\text{Ca}_x\text{Mn}_{0.33}\text{O}_3$  ceramics were studied in detail. Colossal permittivity up to  $10^3$  was obtained across the frequency range up to  $10^6$  Hz. The impedance analysis of the co-doped  $\text{LaAlO}_3$  ceramics indicated that the colossal permittivity phenomenon has been explained by the Koops theory based on Maxwell–Wagner model. The values of ( $\tan\delta_E$ ) sharply decreases as frequency increases in the low frequency region. While in the high frequency region,  $\tan\delta_E$  increases with the increase in frequency. However, in the intermediate frequencies, the values of  $\tan\delta_E$  are minimum which indicates that the compositions are of good quality material in this range. A high precision impedance analyzer has been also used to study the frequency dependent initial permeability.

# CONTENTS

|                         |     |
|-------------------------|-----|
| <b>ACKNOWLEDGEMENTS</b> | V   |
| <b>ABSTRACT</b>         | VI  |
| <b>CONTENTS</b>         | VII |
| <b>LIST OF FIGURES</b>  | XI  |
| <b>LIST OF TABLES</b>   | XIV |

## CHAPTER 1

### INTRODUCTION

|     |                                |   |
|-----|--------------------------------|---|
| 1.1 | Motivation                     | 1 |
| 1.2 | Objectives of the present work | 3 |
| 1.3 | Outline of the Thesis          | 4 |
|     | References                     | 4 |

## CHAPTER 2

### LITERATURE REVIEW

|     |   |    |
|-----|---|----|
| 2.1 | Introduction                            | 8  |
| 2.2 | Origin of colossal dielectric constants | 9  |
|     | 2.2.1 Ferroelectricity                  | 9  |
|     | 2.2.2 Charge-density waves              | 11 |
|     | 2.2.3 Hopping charge transport          | 11 |
|     | 2.2.4 Metal-insulator transition        | 13 |
| 2.3 | General Features of $\text{LaAlO}_3$    | 13 |
|     | 2.3.1 Perovskite structure              | 14 |
| 2.4 | Dielectrics                             | 15 |

|         |  |    |
|---------|--|----|
| 2.4.1   | Polarization   | 17 |
| 2.4.2   | Macroscopic and microscopic polarization               | 18 |
| 2.4.3   | Frequency dependence of polarization                   | 20 |
| 2.5     | Dielectric properties                                  | 23 |
| 2.5.1   | Dielectric Constant                                    | 24 |
| 2.5.1.1 | Dependence of dielectric properties on various factors | 25 |
| 2.5.1.2 | Dependence of dielectric constant on frequency         | 25 |
| 2.5.1.3 | Dependence of dielectric constant on temperature       | 25 |
| 2.5.2   | Dielectric loss  | 26 |
| 2.5.2.1 | Factors affecting dielectric losses                    | 28 |
| 2.5.3   | Dielectric strength                                    | 29 |
| 2.6     | Relaxation phenomena                                   | 30 |
| 2.7     | Magnetism  | 33 |
| 2.7.1   | Permeability   | 34 |
|         | References   | 36 |

## **CHAPTER 3**

### **METHODOLOGY OF SAMPLE PREPARATION**

|       |   |    |
|-------|---|----|
| 3.1   | Sample Preparation Techniques           | 41 |
| 3.2   | Standard solid state reaction technique | 42 |
| 3.2.1 | Reagents                                | 43 |
| 3.2.2 | Mixing                                  | 43 |
| 3.2.3 | Calcination                             | 44 |
| 3.2.4 | Green body preparation                  | 45 |



|       |                                    |    |
|-------|------------------------------------|----|
| 3.2.5 | Uniaxial pressing                  | 46 |
| 3.2.6 | Sintering                          | 47 |
| 3.2.7 | Preparation of the Present Samples | 49 |
|       | References                         | 51 |

## **CHAPTER 4**

### **EXPERIMENTAL TECHNIQUES**

|       |  |    |
|-------|--|----|
| 4.1   | Structural and Morphological Characterization      | 53 |
| 4.1.1 | X-ray diffraction                                  | 53 |
| 4.1.2 | Microstructural studies by SEM/FESEM               | 57 |
| 4.2   | Density and Porosity Calculation                   | 61 |
| 4.3   | Dielectric Properties Measurement                  | 62 |
| 4.3.1 | Impedance Analyzer                                 | 64 |
| 4.3.2 | Theory and working principle of Impedance Analyzer | 64 |
| 4.3.3 | Dielectric measurement techniques                  | 66 |
| 4.3.4 | Measurement of ac-conductivity                     | 68 |
| 4.4   | Impedance Spectroscopy                             | 69 |
| 4.5   | Modulus Spectroscopy                               | 72 |
| 4.6   | Complex permeability measurement                   | 72 |
|       | References   | 74 |

## **CHAPTER 5**

### **RESULTS AND DISCUSSION**

|     |  |    |
|-----|--|----|
| 5.1 | Structural Analysis                      | 77 |
| 5.2 | Density and Porosity                     | 78 |
| 5.3 | Morphological Analysis                   | 80 |
| 5.4 | Dielectric Properties                    | 83 |
|     | 5.4.1 Dielectric constant                | 83 |
|     | 5.4.2 Dielectric loss factor             | 85 |
|     | 5.4.3 Complex impedance spectra analysis | 87 |
|     | 5.4.4 AC conductivity                    | 92 |
| 5.5 | Complex initial permeability             | 93 |
|     | References                               | 96 |

## **CHAPTER 6**

### **CONCLUSIONS**

|     |                                      |     |
|-----|--------------------------------------|-----|
| 6.1 | Conclusions                          | 100 |
| 6.2 | Recommendations for the further work | 103 |

## LIST OF FIGURES

|          |  |    |
|----------|--|----|
| Fig.2.1  | Perovskite $ABO_3$ structure with the A and B cations on the corner and body centre positions, respectively.   | 14 |
| Fig. 2.2 | A parallel plate capacitor, where the electrodes are separated by vacuum and a dielectric material.  | 16 |
| Fig. 2.3 | Non-polar dielectric structure polarizing with external applied field.   | 17 |
| Fig. 2.4 | (a) Imposed forces (torque) acting on a dipole by an electric field. (b) Final dipole alignment with the field.  | 18 |
| Fig. 2.5 | Bias field dependence of the dielectric constant of (a) typical dielectric, (b) tunable dielectric and (c) ferroelectric material.   | 19 |
| Fig. 2.6 | Frequency dependence of the polarization processes.  | 22 |
| Fig. 2.7 | Equivalent circuit diagrams: (a) capacitive cell, (b) charging loss current and (c) loss tangent.  | 27 |
| Fig. 2.8 | Impedance diagrams (top) and Cole-Cole diagrams (bottom) for one polarizable specie in the dielectric a) and typical Debye relaxation with two polarizable species b). Impedance diagram is not an appropriate plot to observe the relaxation process. | 32 |
| Fig. 2.9 | (a) Frequency dependence of real and imaginary part for the case of Debye-type relaxation process. (b) Form of the imaginary permittivity response expected from both <i>Maxwell Wagner</i> and <i>Debye</i> models.                                   | 32 |

|           |  |    |
|-----------|--|----|
| Fig. 2.10 | Various types of magnetism.  | 34 |
| Fig. 3.1  | Balance, mortar and pestle.  | 43 |
| Fig. 3.2  | Typical diagram of a crucible and a programmable electric furnace.   | 45 |
| Fig. 3.3  | Uniaxial pressing.   | 47 |
| Fig. 3.4  | Schematic representation of sintering stages: (a) green body, (b) initial stage, (c) intermediate stage and (d) final stage. | 48 |
| Fig. 3.5  | Graphical representation for the synthesis of ceramics samples by the solid-state reaction route.                            | 50 |
| Fig. 4.1  | Graphical representation of X-ray diffraction technique.   | 54 |
| Fig. 4.2  | Schematic diagram for a typical X-ray powder diffraction experiment.   | 56 |
| Fig. 4.3  | A typical X-ray diffractometer used for XRD.   | 56 |
| Fig. 4.4  | Various types of signals which are generated by electron-matter interactions.  | 58 |
| Fig. 4.5  | Field emission scanning electron microscope (FESEM) setup.   | 60 |
| Fig. 4.6  | Some techniques for the measurement of dielectric properties.  | 63 |
| Fig. 4.7  | A typical diagram of an impedance analyzer.  | 64 |
| Fig. 4.8  | Experimental setup of Wayne Kerr Impedance Analyzer (6500B).   | 67 |
| Fig. 4.9  | Silver paste painted two probe arrangements on the sintered sample.  | 67 |
| Fig. 4.10 | (a) The impedance plot for a circuit of a resistor and a capacitor in parallel and (b) the corresponding equivalent circuit. | 70 |
| Fig. 4.11 | (a) The impedance plot for an ideal polycrystalline sample and (b) the corresponding equivalent circuit.                     | 71 |
| Fig. 5.1  | XRD pattern of $\text{LaAl}_{0.67-x}\text{Ca}_x\text{Mn}_{0.33}\text{O}_3$ ceramics sintered at 1723 K.                      | 77 |
| Fig. 5.2  | variation of density and porosity with Ca content of various   | 79 |

LaAl<sub>0.67-x</sub>Ca<sub>x</sub>Mn<sub>0.33</sub>O<sub>3</sub> ceramics.

- Fig. 5.3 FESEM micrographs (magnification 5,000 times) of various 80  
LaAl<sub>0.67-x</sub>Ca<sub>x</sub>Mn<sub>0.33</sub>O<sub>3</sub> ceramics sintered at 1723 K.
- Fig. 5.4 FESEM micrographs (magnification 10,000 times) of various 81  
LaAl<sub>0.67-x</sub>Ca<sub>x</sub>Mn<sub>0.33</sub>O<sub>3</sub> ceramics sintered at 1723 K.
- Fig. 5.5 FESEM micrographs (magnification 20,000 times) of various 82  
LaAl<sub>0.67-x</sub>Ca<sub>x</sub>Mn<sub>0.33</sub>O<sub>3</sub> ceramics sintered at 1723 K.
- Fig 5.6 Variation of dielectric constant as a function of frequency (a) 10<sup>2</sup>-10<sup>7</sup> Hz 84  
(b) 10<sup>6</sup>-10<sup>7</sup> Hz of LaAl<sub>0.67-x</sub>Ca<sub>x</sub>Mn<sub>0.33</sub>O<sub>3</sub> ceramics sintered at 1723 K.
- Fig.5.7 Frequency dependence of dielectric loss tangent (*tanδ<sub>E</sub>*) (a) 10<sup>3</sup>-10<sup>7</sup> Hz 86  
(b) 10<sup>5</sup>-10<sup>7</sup> Hz of LaAl<sub>0.67-x</sub>Ca<sub>x</sub>Mn<sub>0.33</sub>O<sub>3</sub> ceramics sintered at 1723 K.
- Fig. 5.8 Variation of (a) *Z'* and (b) *Z''*, as a function of frequency of 87  
LaAl<sub>0.67-x</sub>Ca<sub>x</sub>Mn<sub>0.33</sub>O<sub>3</sub> ceramics sintered at 1723 K.
- Fig 5.9 Variation of (a) *M'* and (b) *M''*, as a function of frequency of 89  
LaAl<sub>0.67-x</sub>Ca<sub>x</sub>Mn<sub>0.33</sub>O<sub>3</sub> ceramics sintered at 1723 K.
- Fig. 5.10 (a) cole-cole plot (*Z'' vs Z'*) of various LaAl<sub>0.67-x</sub>Ca<sub>x</sub>Mn<sub>0.33</sub>O<sub>3</sub> ceramics 90  
sintered at 1723 K. (b) Equivalent circuit model.
- Fig. 5.11 (a) Variation of *σ<sub>ac</sub>* with frequency, (b) plots of *logσ<sub>ac</sub>* versus *logω* of 92  
LaAl<sub>0.67-x</sub>Ca<sub>x</sub>Mn<sub>0.33</sub>O<sub>3</sub> ceramics.
- Fig. 5.12 variation of (a) *μ'<sub>i</sub>* (b) *tanδ<sub>M</sub>* with frequency of various LaAl<sub>0.67-x</sub>Ca<sub>x</sub>Mn<sub>0.33</sub>O<sub>3</sub> 94  
ceramics.
- Fig. 5.13 The variations of Relative Quality factors (*Q*-factor) with frequency of 95

various  $\text{LaAl}_{0.67-x}\text{Ca}_x\text{Mn}_{0.33}\text{O}_3$  ceramics.

## LIST OF TABLES

|       |   |    |
|-------|---|----|
| Table | Data of Theoretical density, Bulk density and Porosity of various     | 79 |
| 5.1   | $\text{LaAl}_{0.67-x}\text{Ca}_x\text{Mn}_{0.33}\text{O}_3$ ceramics. |    |

## CHAPTER 1

### INTRODUCTION

#### 1.1 Motivation

The search for new high-performance dielectric materials, exhibiting temperature and frequency stable, colossal permittivity ( $CP > 10^3$ ) as well as sufficiently low dielectric loss, continues to arouse considerable interest motivated by their myriad device miniaturization and high-energy-density storage applications [1-2]. In recent years, a kind of (In, Nb) co-doped rutile  $\text{TiO}_2$  colossal permittivity material was reported, exhibiting high dielectric permittivity ( $>10^4$ ) and low dielectric loss ( $<0.05$ ) simultaneously over a wide frequency and temperature range [3]. After that, this donor and acceptor ions' co-doping strategy has been applied to different material systems, and a series of CP materials have been developed. Rutile  $\text{TiO}_2$  ceramics co-doped with trivalent ( $\text{Al}^{3+}$ ,  $\text{Ga}^{3+}$ , and  $\text{Bi}^{3+}$ ) and pentavalent ( $\text{Nb}^{5+}$ ,  $\text{Ta}^{5+}$ ) cations exhibited good dielectric properties [4-7]. Colossal permittivity has also been obtained from (Nb, Ga) co-doped perovskite  $\text{BaTiO}_3$ , (Nb, Al) codoped rutile  $\text{SnO}_2$ , and (Li, In) co-doped ZnO ceramics [8-10]. Recently many efforts have focused on developing dielectric materials with very high quality factors,  $Q \times f$  ( $Q \approx \tan \delta^{-1}$ ;  $f$ : measuring frequency), for the use as dielectric resonators and as substrates for high temperature superconducting (HTSC) microwave devices [11-12]. The quality factor of dielectric resonators determines their frequency selectivity. In addition to a high quality factor, a high relative permittivity ( $\epsilon_r$ ) and very small temperature coefficient of resonant frequency ( $\tau_f$ ) are necessary for the size reduction and stability of resonators, respectively. Many compounds such as (Ba, Pb) O– $\text{Nd}_2\text{O}_3$ – $\text{TiO}_2$ , (Zr, Sn)  $\text{TiO}_4$ ,  $\text{Ba}(\text{Zn}_{1/3}\text{Ta}_{2/3})\text{O}_3$  and (Mg, Ca) $\text{TiO}_3$  have therefore been developed [13]. Although these compounds exhibit good dielectric properties, a large demand exists for new materials.

Lanthanum aluminate ( $\text{LaAlO}_3$ ), which belongs to the perovskite type oxide materials, has been widely used as a substrate of high-temperature superconductor and ferroelectric thin films due to their low dielectric loss and minor lattice mismatch between the substrate and film [14-15]. The discovery of ferroelectricity in  $\text{BaTiO}_3$  has grown interest on a large number of  $\text{ABO}_3$  type materials such as  $\text{MgTiO}_3$ ,  $\text{CaTiO}_3$ ,  $\text{SrTiO}_3$ ,  $\text{LaAlO}_3$  etc. that have various important applications in electronic industries as they exhibit diverse electrical properties such as superconductivity, ferroelectricity, piezoelectricity, magnetism and dielectric properties. Diversity of structures of  $\text{BaTiO}_3$  based perovskite attracted the attention of the researchers in a wide range of fields including solid state chemistry, physics and communication technology. Capacitors are one of the key components in the electrical circuits and the present trend in the electronics industries is the development of smaller electrical devices. Ferroelectric materials play an important role in the development of miniaturized capacitors and the overall size of the circuits. A relatively high value of dielectric constant ( $\epsilon$ ) makes it possible to minimize the size of the capacitor and decrease the volume of the electronic device. But the value of  $\epsilon$  strongly depends on the electric field, frequency and temperature which are undesirable for applications in most of devices. Thus, the interest is now shifted to find dielectric materials of high  $\epsilon$  which are independent of the electric field, frequency and temperature.

Although colossal permittivity could be realized by donor and acceptor ions' co-doping in different matrix materials, the underlying mechanism is controversial. Different polarization mechanisms such as the internal barrier layer capacitance (IBLC) effect, Maxwell-Wagner (MW) polarization and hopping polaron mechanism have been applied to explain the dielectric phenomena [16-18]. We cannot deny that some polarization phenomenon originates from the interaction between the matrix defect and dopant. But it would be meaningful for understanding



the dielectric polarization mechanism to investigate the contribution of defects only from dopants.  $\text{LaAlO}_3$  is a member of the perovskite family and has an open structure for A and B site doping without valence change. It has a moderate dielectric permittivity ( $\sim 25$ ) and very low dielectric loss ( $\sim 10^{-4}$ ) over a wide frequency and temperature range [19]. Thus, the effect of doping elements on dielectric properties of the material is easy to identify. Moreover, the substitution of transition metal elements at B sites and their effects on the dielectric behavior of  $\text{LaGaO}_3$  have already been reported [20].

## 1.2 Objectives of the present work

Present work entails the following objectives:

- Preparation of various  $\text{LaAl}_{0.67-x}\text{Ca}_x\text{Mn}_{0.33}\text{O}_3$  ( $x=0.00, 0.02, 0.04, 0.05$ ) using standard solid state reaction technique.
- Structural characterization was done by the X-ray diffraction (XRD). From the XRD results, lattice parameters, density and porosity of all the compositions were determined.
- Surface morphology and average grain sizes of all samples were investigated by a high resolution scanning electron microscope (SEM).
- Frequency and composition dependence of dielectric constant, dielectric loss and ac conductivity were studied.
- Impedance spectroscopy of all the samples was also studied.
- Investigation of the complex initial permeability as a function of frequency of all the studied samples.

### 1.3 Outline of the Thesis

The summary of the thesis is as follows:

**Chapter-1:** Introduction: Motivation and objectives of the present work.

**Chapter-2:** Literature review of the present work materials. In this chapter general information about perovskite structure, dielectric and magnetic properties of the materials are given.

**Chapter-3:** Methodology of sample preparation is described.

**Chapter-4:** Experimental techniques used to measure the important parameters during the entire study are described.

**Chapter-5:** Discusses the results of various investigations of the study and explanation of results in the light of existing theories.

**Chapter-6:** Conclusions and suggestions for further investigation are presented.

### References

- [1] Homes, C.C., Vogt, T., Shapiro, S.M., Wakimoto, S. and Ramirez, A.P., “Optical response of high-dielectric-constant perovskite-related oxide,” *Science*, 293(5530), pp.673-676, 2001.
- [2] Krohns, S. et al. “The route to resource-efficient novel materials,” *Nature Mater.* 10, 899-901, 2011.
- [3] Hu, W., Liu, Y., Withers, R.L., Frankcombe, T.J., Norén, L., Snashall, A., Kitchin, M., Smith, P., Gong, B., Chen, H. and Schiemer, J., “ Electron-pinned defect-dipoles for high performance colossal permittivity materials,” *Nature materials*, 12(9), p.821, 2013.

- [4] Cheng, X., Li, Z. and Wu, J., “ Colossal permittivity in ceramics of TiO<sub>2</sub> Co-doped with niobium and trivalent cation,” *Journal of Materials Chemistry A*, 3(11), pp.5805-5810, 2015.
- [5] Dong, W., Hu, W., Berlie, A., Lau, K., Chen, H., Withers, R.L. and Liu, Y., “ Colossal dielectric behavior of Ga<sup>+</sup>, Nb co-doped rutile TiO<sub>2</sub>,” *ACS applied materials & interfaces*, 7(45), pp.25321-25325, 2015.
- [6] Hu, W., Lau, K., Liu, Y., Withers, R.L., Chen, H., Fu, L., Gong, B. and Hutchison, W., “Colossal dielectric permittivity in (Nb<sup>+</sup>, Al) codoped rutile TiO<sub>2</sub> ceramics: compositional gradient and local structure,” *Chemistry of Materials*, 27(14), pp.4934-4942, 2015.
- [7] Dong, W., Hu, W., Frankcombe, T.J., Chen, D., Zhou, C., Fu, Z., Cândido, L., Hai, G., Chen, H., Li, Y. and Withers, R.L., “ Colossal permittivity with ultralow dielectric loss in In<sup>+</sup>, Ta co-doped rutile TiO<sub>2</sub>,” *Journal of Materials Chemistry A*, 5(11), pp.5436-5441, 2017.
- [8] Wu, Y., Miao, J., Liu, Z. and Li, Y., “ Colossal permittivity and dielectric relaxations in BaTi<sub>0.99</sub>(Nb<sub>0.5</sub>Ga<sub>0.5</sub>)<sub>0.02</sub>O<sub>3</sub> ceramics,” *Ceramics International*, 41, pp.S846-S850, 2015.
- [9] Song, Y., Wang, X., Zhang, X., Qi, X., Liu, Z., Zhang, L., Zhang, Y., Wang, Y., Sui, Y. and Song, B., “Colossal dielectric permittivity in (Al<sup>+</sup>, Nb) co-doped rutile SnO<sub>2</sub> ceramics with low loss at room temperature,” *Applied Physics Letters*, 109(14), p.142903, 2016.

- [10] Huang, D., Liu, Z., Li, Y. and Liu, Y., “Colossal permittivity and dielectric relaxation of (Li, In) Co-doped ZnO ceramics,” *Journal of Alloys and Compounds*, 698, pp.200-206, 2017.
- [11] O'bryan, H.M., Gallagher, P.K., Berkstresser, G.W. and Brandle, C.D., “Thermal analysis of rare earth gallates and aluminates,” *Journal of Materials Research*, 5(1), pp.183-189, 1990.
- [12] Dube, D.C., Scheel, H.J., Reaney, I., Daghish, M. and Setter, N., “ Dielectric properties of lanthanum gallate (LaGaO<sub>3</sub>) crystal,” *Journal of applied physics*, 75(8), pp.4126-4130, 1994.
- [13] Brown, R., Pendrick, V., Kalokitis, D. and Chai, B.H.T., “Low-loss substrate for microwave application of high-temperature superconductor films,” *Applied Physics Letters*, 57(13), pp.1351-1353, 1990.
- [14] Simon, R.W., Platt, C.E., Lee, A.E., Lee, G.S., Daly, K.P., Wire, M.S., Luine, J.A. and Urbanik, M., “Low-loss substrate for epitaxial growth of high-temperature superconductor thin films,” *Applied physics letters*, 53(26), pp.2677-2679, 1988.
- [15] Först, C.J., Schwarz, K. and Blöchl, P.E., “Structural and electronic properties of the interface between the high-k oxide LaAlO<sub>3</sub> and Si (001),” *Physical review letters*, 95(13), p.137602, 2005.
- [16] Li, J., Li, F., Li, C., Yang, G., Xu, Z. and Zhang, S., “Evidences of grain boundary capacitance effect on the colossal dielectric permittivity in (Nb<sup>+</sup>, In) co-doped TiO<sub>2</sub> ceramics,” *Scientific reports*, 5, p.8295, 2015.

- [17] Tuichai, W., Danwittayakul, S., Chanlek, N., Srepusharawoot, P., Thongbai, P. and Maensiri, S., “Origin (s) of the apparent colossal permittivity in  $(\text{In}_{1/2}\text{Nb}_{1/2})_x\text{Ti}_{1-x}\text{O}_2$ : clarification on the strongly induced Maxwell–Wagner polarization relaxation by DC bias,” *RSC Advances*, 7(1), pp.95-105, 2017.
- [18] Mandal, S., Pal, S., Kundu, A.K., Menon, K.S., Hazarika, A., Rioult, M. and Belkhou, R., “Direct view at colossal permittivity in donor-acceptor (Nb, In) co-doped rutile  $\text{TiO}_2$ ,” *Applied physics letters*, 109(9), p.092906, 2016.
- [19] Dube, D.C., Scheel, H.J., Reaney, I., Daghli, M. and Setter, N., “Dielectric properties of lanthanum gallate ( $\text{LaGaO}_3$ ) crystal,” *Journal of applied physics*, 75(8), pp.4126-4130, 1994.
- [20] Rai, H.M., Saxena, S.K., Late, R., Mishra, V., Rajput, P., Sagdeo, A., Kumar, R. and Sagdeo, P.R., “Observation of large dielectric permittivity and dielectric relaxation phenomenon in Mn-doped lanthanum gallate,” *RSC Advances*, 6(32), pp.26621-26629, 2016.

## CHAPTER 2

### LITERATURE REVIEW

#### 2.1 Introduction

Hot topics like high- $T_c$  superconductivity, colossal magnetoresistance and multiferroicity have led to a tremendous boost of solid state physics during the last 25 years. These and other interesting phenomena to a large extent first have been revealed and intensely investigated in transition-metal oxides. The complexity of the ground states of these materials arises from strong electronic correlations, enhanced by the interplay of spin, orbital, charge and lattice degrees of freedom. These phenomena are a challenge for basic research and also bear enormous potentials for future applications as the related ground states are often accompanied by so-called “colossal” effects, which are possible building blocks for tomorrow’s correlated electronics.

The measurement of the response of transition-metal oxides to ac electric fields is one of the most powerful techniques to provide detailed insight into the underlying physics that may comprise very different phenomena, e.g., charge order, molecular or polaronic relaxations, magnetocapacitance, hopping charge transport, ferroelectricity or density-wave formation. The present work concentrates on materials showing so-called colossal dielectric constants (CDC), i.e. values of the real part of the permittivity  $\varepsilon'$  exceeding 1000. Since long, materials with high dielectric constants are in the focus of interest, not only for purely academic reasons but also because new high- $\varepsilon'$  materials are urgently sought after for the further development of modern electronics. In general, for the miniaturisation of capacitive electronic elements materials with high- $\varepsilon'$  are prerequisite. This is true not only for the common silicon-based integrated-circuit technique but also for stand-alone capacitors. For example, the latter, if constructed using

materials with CDCs, can reach capacitances high enough to enable their use for energy storage, without the disadvantage of escalating volume and weight. Such capacitors can be used, e.g., to replace batteries in hybrid vehicles.

Most of the currently available capacitor materials with CDCs are based on ferroelectrics, which reach very high values of the dielectric constant often exceeding  $10^4$ . However, ferroelectric materials exhibit a strong temperature dependence of  $\epsilon'$ , limiting their straightforward application in electronic devices. Currently, the most prominent non-ferroelectric material showing colossal values of  $\epsilon'$  is  $\text{CaCu}_3\text{Ti}_4\text{O}_{12}$  (CCTO). Initiated by the first reports of extremely high dielectric constants in CCTO in 2000 [1].

## 2.2 Origin of colossal dielectric constants

The most prominent mechanisms that can give rise to enhanced values of the dielectric constant are ferroelectricity, charge-density wave formation, hopping charge transport, the metal-insulator transition.

### 2.2.1 Ferroelectricity

It is known since long that in ferroelectrics very high values of the dielectric constant can arise [2-3]. Approaching the ferroelectric phase transition at  $T_c$  from high temperatures,  $\epsilon'$  (T) strongly increases, usually following a Curie-Weiss behaviour and starts to decrease again below  $T_c$ . In addition, ferroelectrics have pronounced non-linear dielectric properties, e.g., showing characteristic hysteresis loops of the electric-field dependent polarization [3]. Both phenomena represent problems for application in electronic devices. This partly can be overcome by doping and special processing thereby adjusting microstructure and internal interfaces. The well-known ceramic Barrier Layer Capacitors use a combination of interface

polarisation effects and ferroelectric materials like BaTiO<sub>3</sub> to achieve high capacitance values with temperature and voltage dependences that are tolerable at least for some applications [4-6]. Ferroelectric transitions often are classified as displacive or order-disorder type. The latter case corresponds to the ordering of dipolar degrees of freedom already present at  $T > T_c$ . In these systems the hopping of the dipoles can lead to strong frequency dependence of  $\epsilon'$  at technically relevant frequencies (Hz-GHz) making them less suited for application [3, 7, 8]. In contrast, ferroelectrics of displacive type usually show no frequency dependence up to infrared frequencies, where the well-known soft-phonon modes appear [3].

A special variant of ferroelectrics are the so-called relaxor ferroelectrics [9, 10]. Their static dielectric constant shows a strong increase with decreasing temperature just as for canonical ferroelectrics. However, this is superimposed by a marked relaxation mode that leads to peaks in  $\epsilon'$  (T) at temperatures that are strongly dependent on frequency. Different explanations have been proposed for this behaviour, e.g., in terms of polar cluster dynamics, but no consensus has been achieved so far [9-13].

While in conventional and relaxor ferroelectrics ions or dipoles are the relevant entities achieving ferroelectric order, also the ordering of electronic degrees of freedom has been considered [14-16]. For example, the occurrence of CDCs of magnitude  $>4000$  detected in the mixed-valent transition-metal oxide LuFe<sub>2</sub>O<sub>4</sub> was ascribed to an electronic polarisation mechanism involving charge ordering of Fe<sup>2+</sup> and Fe<sup>3+</sup> ions [17]. Also in certain charge-transfer salts a ferroelectric transition of electronic origin recently was discussed [7, 18].

Finally, it should be mentioned that in some materials, the so-called incipient ferroelectrics, long-range ferroelectric order is prevented by quantum fluctuations at low temperature, setting in before complete order is achieved at  $T_c$ . At temperatures sufficiently above  $T_c$ ,  $\epsilon'$  (T) of these



materials follows the Curie-Weiss law and thus CDCs are observed. The most prominent incipient ferroelectric is  $\text{SrTiO}_3$  [19], which shows a tendency of  $\epsilon'(T)$  to saturate at low temperatures, setting in below about 30K due to the mentioned quantum effects [20]. Besides  $\text{BaTiO}_3$ , also  $\text{SrTiO}_3$  is often employed as dielectric material in commercial ceramic Barrier Layer Capacitors.

### 2.2.2 Charge-density waves

In highly anisotropic low-dimensional materials a metal-insulator transition can arise with lowering of the temperature, which is accompanied by the formation of a charge-density wave (CDW). Here the electronic charge density is a periodic function of position and its period can be incommensurate with the crystal lattice. A very well-known example of a CDW system is also found in the group of transition-metal oxides, namely the blue bronze,  $\text{K}_{0.30}\text{MoO}_3$  [21]. A harmonic oscillator mode at GHz frequencies caused by the CDW being pinned at defects and a huge relaxation mode at kHz-MHz involving colossal values of the dielectric constant [22-24]. In CDW systems the highest intrinsic dielectric constants of any materials are observed, reaching magnitudes of up to  $10^8$ . Littlewood has proposed screening effects of the pinned CDW by the normal electrons, not participating in the CDW, to explain the occurrence of the low-frequency relaxation mode and CDCs in this class of materials. Due to the strong frequency dependence of  $\epsilon'$  and the high dielectric losses associated with the relaxational modes, CDWs are not applied in capacitive devices.

### 2.2.3 Hopping charge transport

Hopping conductivity is the most common charge-transport process in condensed matter. As it is intimately related to the occurrence of a power law with negative exponent in the frequency

dependent dielectric constant  $\varepsilon'(\nu)$ , it will always lead to a divergence of  $\varepsilon'$  for low frequencies [25-28]. Hopping conduction is the typical charge-transport process of localised charge carriers. In electronic conductors, electrons (or holes) can localise due to disorder. Disorder may arise from an amorphous structure, from doping (substitutional disorder) or occur even in nominally pure crystals due to slight deviations from stoichiometry or lattice imperfections. Hopping conduction leads to a characteristic signature in the frequency dependence of the complex conductivity, namely a power-law increase  $\sigma' = \sigma_0 \nu^s$  with the exponent  $s < 1$  [25, 26, 29]. This power law was shown by Jonscher [27, 28] to be a quite universal phenomenon in all types of disordered matter and termed “Universal Dielectric Response” (UDR). This behaviour can be understood in the framework of various models on the charge transport of localised charge carriers, including the often-employed variable-range hopping (VRH) model. These models originally were developed for amorphous and highly doped semiconductors like doped silicon but also, e.g., for thin scandium-oxide films. The typical signature of hopping transport in measurements of the ac conductivity was also found in numerous transition-metal oxides. Via the Kramers-Kronig relation, the  $\nu^s$  power law also leads to a corresponding power law in the imaginary part of the ac conductivity, namely  $\sigma'' = \tan(s\pi/2)\sigma_0\nu^s$  [28]. As the dielectric constant is directly related to  $\sigma''$  via  $\varepsilon' = \sigma''/(2\pi\nu\varepsilon_0)$  (with  $\varepsilon_0$  the permittivity of vacuum) hopping conduction is expected to lead to a power law  $\varepsilon' \propto \nu^{s-1}$ . Thus, as  $s < 1$ , the dielectric constant can easily reach colossal magnitudes for low frequencies. However, as the factor  $\tan(s\pi/2)$  usually is of the order of one, the dielectric loss  $\varepsilon'' = \sigma''/(2\pi\nu\varepsilon_0)$  is relatively high (which of course is reasonable for a conducting material) rendering this effect unsuited for application.

### 2.2.4 Metal-insulator transition

It is known since about 100 years that the Clausius-Mosotti relation will lead to a polarisation catastrophe, i.e. a divergence of the dielectric constant when approaching the metal-insulator (MI) transition from the insulating side [30]. It is naively clear that the reduction of the restoring forces experienced by electrons localised at atomic sites, which should occur when the material approaches the metallic state with its itinerant electron states, will lead to an increase of the electronic polarisability and thus the dielectric constant. Indeed, such a divergence has been observed in some cases, the most prominent one being measurements of the dielectric properties of doped silicon for increasing doping level [31]. Several theoretical approaches have appeared treating this topic and going beyond the simple arguments based on the Clausius-Mosotti equation [32]. Prototypical MI transitions are regularly found in transition metal oxides, the most well-known ones being those in magnetite,  $\text{Fe}_3\text{O}_4$ , and vanadium oxide,  $\text{V}_2\text{O}_3$ . One may speculate if some of the observations of CDCs in transition-metal oxides could be due to the fact that these materials often are at the verge of a MI transition. However, in most cases interfacial effects as treated in the following section seem the more likely explanation. The expected divergence of  $\epsilon'$  at the MI transition of course is also accompanied by an increase of the conductivity, preventing any technical application of this effect for the construction of capacitive components.

### 2.3 General Features of $\text{LaAlO}_3$

Lanthanum aluminate is an inorganic compound with the formula  $\text{LaAlO}_3$ , often abbreviated as LAO. It is an optically transparent ceramic oxide with a distorted perovskite structure. Crystalline  $\text{LaAlO}_3$  has a relatively high relative dielectric constant of  $\sim 25$ . The most important and common use for epitaxial LAO is at the lanthanum aluminate-strontium titanate interface. In

2004, it was discovered that when 4 or more unit cells of LAO are epitaxially grown on strontium titanate ( $\text{SrTiO}_3$ , STO), a conductive 2-dimensional layer is formed at their interface. Individually,  $\text{LaAlO}_3$  and  $\text{SrTiO}_3$  are non-magnetic insulators, yet  $\text{LaAlO}_3/\text{SrTiO}_3$  interfaces exhibit electrical conductivity, superconductivity, ferromagnetism, large negative in-plane magnetoresistance, and giant persistent photoconductivity. The study of how these properties emerge at the  $\text{LaAlO}_3/\text{SrTiO}_3$  interface is a growing area of research in condensed matter physics.

### 2.3.1 Perovskite structure

Perovskite is a family name of a group of materials and the mineral name of calcium titanate ( $\text{CaTiO}_3$ ) having a structure of the type  $\text{ABO}_3$ . In this structure, the A-site ion, on the corners of the lattice, is usually an alkaline earth or rare earth element. B-site ions, on the center of the lattice, could be 3d, 4d and 5d transitional metal elements. A-site might be occupied by mono valent, divalent or trivalent metal and B-site might be trivalent, tetravalent or pentavalent metal. A large number of metallic elements are stable in the perovskite structure. Many ferroelectric (including piezoelectric) ceramics such as BT, PT, PZT, PLZT, Lead Magnesium Niobate (PMN), KN etc. have a cubic perovskite type structure (in the paraelectric state) with chemical formula  $\text{ABO}_3$  (Fig. 2.1).

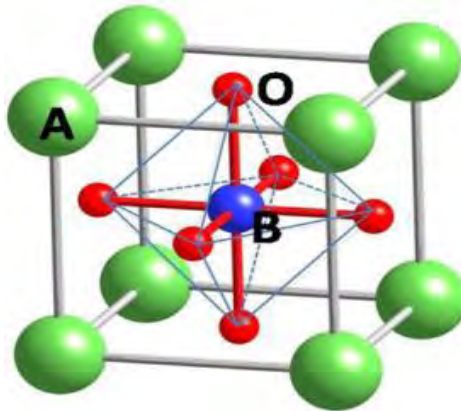


Fig.2.1: Perovskite  $\text{ABO}_3$  structure with the A and B cations on the corner and body centre positions, respectively.

As conventionally drawn, A-site cations occupy the corners of a cube, while B-site cations sit at the body center. Six oxygen atoms per unit cell rest on the faces. The lattice constant of the perovskite structure is usually close to the 4 Å due to rigidity of the oxygen octahedral network and the well-defined oxygen ionic radius of 1.35 Å.

A practical advantage of the perovskite structure is that many different cations can be substituted on both the A- and B- sites without drastically changing the overall structure. Complete solid solutions are easily formed between many cations, often across the entire range of composition. Even though two cations are compatible in solution, their behaviour can be radically different when apart from each other. Thus, it is possible to manipulate a material's properties such as  $T_C$  or  $\varepsilon'$  with only a small substitution of a given cation.

## 2.4 Dielectrics

The word dielectric is derived from the prefix dia, originally from Greek, which means 'through' or 'across', thus the dielectric is referred to as a material that permits the passage of the electric flux but not particles. The dielectric is generally considered a nonconducting or an insulating material that can be polarized by applying an electric field as shown in Fig. 2.2. When a dielectric is placed in an electric field, electric charges do not flow through the materials as in a conductor, but only slightly shift from their average equilibrium positions causing dielectric polarization. Because of dielectric polarization, positive charges are displaced toward the field and negative charges shift in the opposite direction. This creates an internal electric field which reduces the overall field within the dielectric itself.

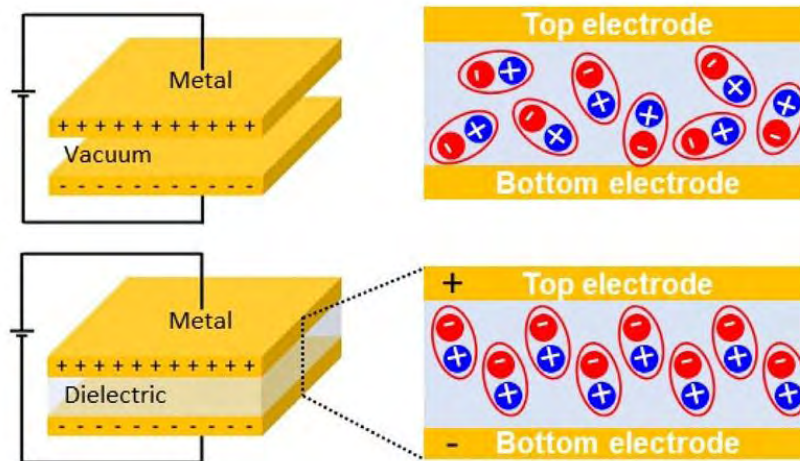


Fig. 2.2: A parallel plate capacitor, where the electrodes are separated by vacuum and a dielectric material.

An insulator, also called a dielectric, is a material that resists the flow of electric charge. In insulating materials valence electrons are tightly bonded to their atoms. These materials are used in electrical conductors without allowing current through themselves. The study of dielectric properties is concerned with the storage and dissipation of electric and magnetic energy in materials. It is important to explain various phenomenon in electronics, optics and solid state physics.

Dielectrics are broadly divided into two classes: polar dielectrics and non-polar dielectrics. In polar dielectric, a shift has occurred in the atomic structures such that the positive and negative charges have an asymmetrical alignment producing an electrical dipole. Non-polar dielectric materials lack this inherent dipole in the absence of a polarizing field, however when an external potential is applied, a dipole forms a shift in the electron cloud as shown in Fig. 2.3.

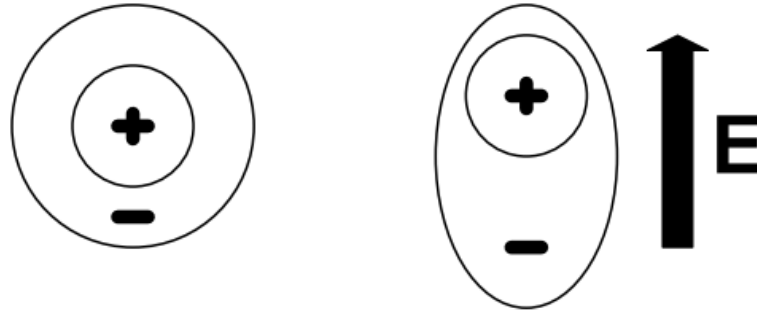


Fig. 2.3: Non-polar dielectric structure polarizing with external applied field.

### 2.4.1 Polarization

For every dipole, there is a separation between a positive and a negative electric charge. An electric dipole moment  $p$  is associated with each dipole as follows:

$$p = q \times d \quad (2.1)$$

Where  $q$  is the magnitude of each dipole charge and  $d$  is the distance of separation between them. In the presence of an electric field  $E$ , which is a vector quantity, a force (or torque) will come to bear on an electric dipole to orient it with the applied field; this phenomenon is illustrated in Fig. 2.4. The process of dipole alignment is termed polarization [33].

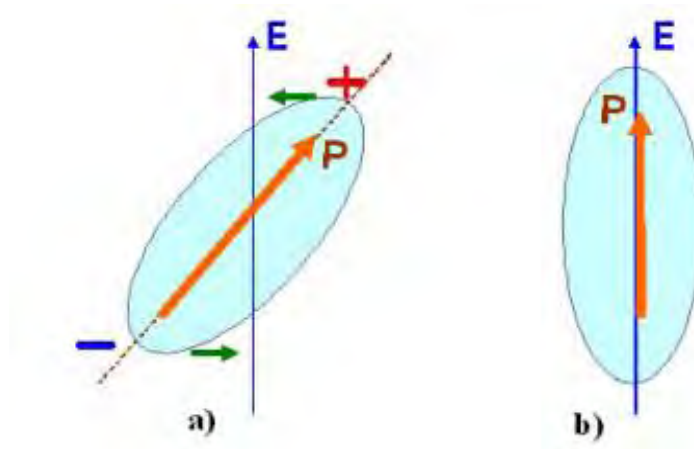


Fig. 2.4: (a) Imposed forces (torque) acting on a dipole by an electric field. (b) Final dipole alignment with the field [33].

#### 2.4.2 Macroscopic and microscopic polarization

In accordance to the Poisson equation, the source of the dielectric displacement  $\mathbf{D}$  is given by the density of charges  $\rho$ :

$$\text{div } \mathbf{D} = \rho \quad (2.2)$$

Equation (2.2) shows that electric displacement can be considerably increased from charges in the materials. Based on this relation, the global charge neutrality of matter within an external field is described by:

$$\mathbf{D} = \varepsilon_0 \mathbf{E} + \mathbf{P} \quad (2.3)$$

$\varepsilon_0 \mathbf{E}$  represent the vacuum contribution induced by the externally applied electric field,  $\mathbf{P}$  is the electrical polarization of the matter. It is important to note that  $\mathbf{P}$  can be induced by pyroelectric polarization, piezoelectric polarization, ferroelectric polarization or dielectric polarization (by an external electric field).



For a pure dielectric material, the polarization is proportional to the electric field in linear approximation by:

$$\mathbf{P} = \varepsilon_0 \chi_e \mathbf{E} \text{ or } \mathbf{D} = \varepsilon_0 \varepsilon_r \mathbf{E} \quad (2.4)$$

Here, the material properties are:

$\chi_e$  is the electrical susceptibility,

$\varepsilon_r$  is the relative dielectric constant with  $\varepsilon_r = 1 + \chi_e$ ,

For many dielectrics,  $\chi_e$  and  $\varepsilon_r$  are field-independent. However, large electric fields can lead to strong non-linear dielectric properties. Therefore tunable dielectrics are achieved. From the device point of view, this property (tunability) is particularly interesting as the capacity to store charges can be tuned by varying the voltage [34]. We can note that in ferroelectric materials, the variation in  $\varepsilon_r$  leads to a hysteresis behaviour as shown in Fig. 2.5.

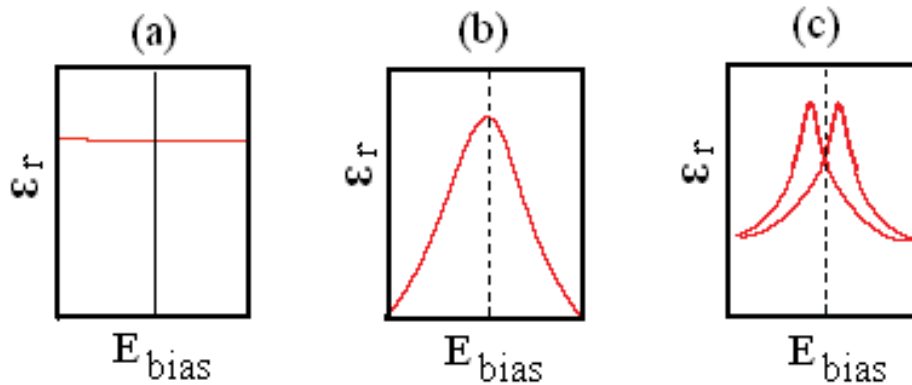


Fig. 2.5: Bias field dependence of the dielectric constant of (a) typical dielectric, (b) tunable dielectric and (c) ferroelectric material [34].

The correlation between the macroscopic polarization  $\mathbf{P}$  and the microscopic properties of the material can be discussed as: the macroscopic polarization  $\mathbf{P}$  is the sum of all individual dipole moments  $\mathbf{p}_a$  with their density  $N_a$ . The contribution can be described by:

$$\mathbf{P} = \Sigma N_a \mathbf{p}_a \quad (2.5)$$

If we consider a single (polarizable) particle, and if the particle is put into an electric field, the dipole moments are induced by the local electric field  $\mathbf{E}_{loc}$  at the dipole site:

$$\mathbf{P} = N_a \alpha \mathbf{E}_{loc} \quad (2.6)$$

$\alpha$  is the polarizability of an atomic dipole. In condensed matter, the electrostatic interactions between the microscopic dipoles make the local electric field different from the external macroscopic one  $\mathbf{E}_a$ , i-e,  $\mathbf{E}_{loc} \neq \mathbf{E}_a$ :

$$\mathbf{E}_{loc} = \mathbf{E}_a + \Sigma \mathbf{E}_{dipole} \quad (2.7)$$

Therefore, the local field is higher than the macroscopic field inside the dielectric due to contribution of all dipoles.

So far, another field has been voluntarily neglected since dipoles were only considered parallel oriented along the applied electric field. This hypothesis is true for example when the dielectric structure is face-centered cubic. Thus, the barycentre of positive and negative ions is uniform in all the directions (isotropic contribution) assuming that field induce by the atoms  $\mathbf{E}_{atoms} = 0$ . For ferroelectric materials, e.g. BaTiO<sub>3</sub>,  $\mathbf{E}_{atoms}$  cannot be neglected anymore even in the cubic phase due to strong directional dependence of the oxygen neighborhood (strong anisotropy) [34].

### 2.4.3 Frequency dependence of polarization

The total polarization of a dielectric material can be obtained by four contributions. They are discussed below. Each one contributes to the dielectric response but in different frequency regimes since they involve different polarizable species. Polarization occurs due to several atomic mechanisms. For example, let us consider an atom placed inside an electric field. The

centre of positive charge is displaced along the applied field direction, while the centre of negative charge is displaced in the opposite direction. Thus a dipole is produced. When a dielectric material is placed inside an electric field such dipoles are created in all the atoms inside. This process of producing electric dipoles which are oriented along the field direction is called polarization in dielectrics.

There are several types of polarization mechanisms. The basic polarizations mechanisms are; space charge ( $\alpha_s$ ), orientational or dipolar ( $\alpha_o$ ), ionic ( $\alpha_i$ ) and electronic ( $\alpha_e$ ) (Fig.2.6). The total polarizability of dielectric placed in an alternating field can be written as:

$$\alpha_{Tot} = \alpha_s + \alpha_o + \alpha_i + \alpha_e \quad (2.8)$$

**Space charge polarization** could exist in dielectric material if the density of charge carrier is not homogeneously distributed. This polarization is the slowest process, as it involves the diffusion of ions over several inter-atomic distances. The relaxation time for this process is related to the frequency of successful jumps of ions under the influence of the applied field, a typical value being  $10^2$  Hz. Correspondingly, space charge polarization occurs at lower frequencies (50 ~ 60 Hz). Consider a dielectric medium placed between two electrodes. When no field is applied to the electrode, the positive and negative charges are not separated and there are fixed number of charges. On the other hand, when an electric field is applied, the charges are separated. The positive charges are accumulated near the negative electrode. Therefore, a dipole moment is induced due to displacement of ions. Then, the induced dipole moment per unit volume gives the induced polarization. This polarization is also known as interfacial polarization. This polarization is also known as Maxwell-Wagner polarization.

**Dipolar polarization** or **orientational polarization** arises when the substance is built up of molecules possessing a permanent electronic dipole moment which may be more or less free to

change orientation in an applied electric field. More clearly, according to Debye, this type of polarization is due to the rotation (orientation) of the molecules of polar dielectrics having a constant dipole moment in the direction of the applied electric field. Orientation polarization is even slower than ionic polarization. The relaxation time for orientation polarization in a liquid is less than that in a solid. For example the relaxation time for orientation polarization is  $10^{-10}$  s in liquid propyl alcohol while it is  $3 \times 10^{-6}$  s in solid ice. Orientation polarization occurs when the frequency of the applied voltage is in the audio range.

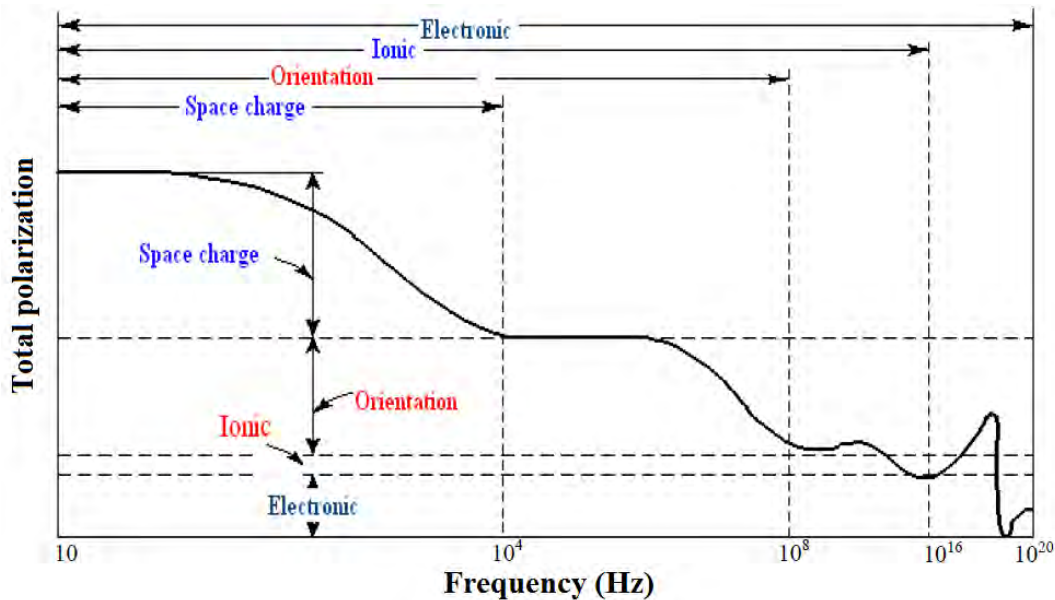


Fig. 2.6: Frequency dependence of the polarization processes.

**Ionic polarization** comes from the displacement and deformation of a charged ion with respect to other ions, i.e. ionic polarization is due to displacement of ions over a small distance due to the applied field. Since ions are heavier than electron cloud, the time taken for displacement is larger. The frequency with which ions are displaced is of the same order as the lattice vibration frequency ( $\sim 10^{13}$  Hz). This means that for optical frequency the ions do not respond, as the time required for lattice vibrations is nearly 100 times larger than the period of applied voltage at

optical frequency. Hence, at optical frequencies, there is no ionic polarization. If the frequency of the applied voltage is less than  $10^{13}$  Hz, the ions respond. Hence at  $10^{13}$  Hz, we have both electronic polarization and ionic polarization responding.

**Electronic polarization** exists in all materials. It is based on the displacement of the negatively charged electron shell against the positively charged core. This displacement occurs due to the equilibrium between restoration and electric forces. **Electronic polarization** may be understood by assuming an atom as a point nucleus surrounded by spherical electron cloud of uniform charge density. In a solid, the resonance frequencies correspond to electronic inter- and intra-band transitions. Electronic polarization is extremely rapid. Even when the frequency of the applied voltage is very high in the optical range ( $\sim 10^{15}$  Hz), electronic polarization occurs during every cycle of the applied voltage.

In the calculation of total polarization, the space charge polarization is not taken into account, since it occurs as interface and it is very small and hence negligible. In addition to this, the fields are not well defined at interfaces. Therefore, the total polarization vector is given by,

$$P = P_e + P_i + P_o \quad (2.9)$$

Where  $P_e$  is electronic polarization,  $P_i$  is ionic polarization and  $P_o$  is orientational polarization.

## 2.5 Dielectric properties

Studies of dielectric properties provide a great deal of information about the suitability of the material for various applications. Dielectric constant ( $\epsilon'$ ), dielectric loss ( $\tan\delta_E$ ) and dielectric break down are important parameters for dielectric materials.

### 2.5.1 Dielectric Constant

The dielectric constant is a number relating the ability of a material to carry alternating current to the ability of vacuum to carry alternating current. The capacitance created by the presence of the material is directly related to the dielectric Constant of the material. Also, the dielectric constant is the ratio of the permittivity of a substance to the permittivity of free space. It is an expression of the extent to which a material concentrates electric flux, and is the electrical equivalent of relative magnetic permeability. As the dielectric constant increases, the electric flux density increases, if all other factors remain unchanged. This enables objects of a given size, such as sets of metal plates, to hold their electric charge for long periods of time, and/or to hold large quantities of charge.

The capacitance for a parallel plate capacitor with vacuum between the capacitor plates is given by,

$$C_0 = \varepsilon_0 A/d \quad (2.10)$$

Where  $\varepsilon_0$  is the permittivity of free space,  $A$  is the area of electrode and  $d$  is the separation between two electrodes.

When a dielectric (electrical insulator) fills the space between the plates, the capacitance of the capacitor is increased by a factor  $\varepsilon'$ , which is called the dielectric constant of the dielectric material. Therefore, for a parallel plate capacitor with a dielectric between the capacitor plates, the capacitance,  $C$  is given by,

$$C = \varepsilon' \varepsilon_0 A/d \quad (2.11)$$

Therefore, the dielectric constant of the given dielectric material can be written as,

$$\varepsilon' = C/C_0 \quad (2.12)$$

### 2.5.1.1 Dependence of dielectric properties on various factors

$\epsilon'$  is the property of a dielectric medium that determines the force of the electric charges that exerts on the dielectric. The value of  $\epsilon'$  depends on the several external factors, such as the frequency of the voltage applied to the dielectric, temperature, particle size etc.

### 2.5.1.2 Dependence of dielectric constant on frequency

The time required for electronic or ionic polarization to set in, is very small as compared with the time of voltage sign change with the half period of alternating voltage, even of the highest frequencies which find practical use in electrical and radio engineering. For this reason, the polarization of deformational mechanism of polarization, completely settles itself during a very short period of time as compared with voltage half period. The value of  $\epsilon'$  of non-polar dielectrics does not depend on frequency when it changes within very broad limits.

The value of  $\epsilon'$  depends on frequency only in the case of polar dielectrics. When the frequency of alternative voltage increases the value of  $\epsilon'$  of a polar dielectric at first remains invariable but above a certain critical frequency ' $f_o$ ' (when polarization fails to settle itself completely during one half periods)  $\epsilon'$  begins to drop approaching. At very high frequencies,  $\epsilon'$  behaves like the typical value of non-polar dielectrics.

### 2.5.1.3 Dependence of dielectric constant on temperature

The process of electronic polarization in non-polar dielectric does not depend on temperature because temperature does not affect the electronic polarizability of molecules. However, due to thermal expansion of matter, the ratio of number of molecules in the effective length,  $L$  of the dielectric diminishes when temperature increases and thus  $\epsilon'$  also diminishes. In solid ionic dielectric, the dependence of  $\epsilon'$  on temperature may be different. In most cases an ionic

mechanism of polarization increases when the temperature grows. In polycrystalline materials at low frequency region space charges become more active during the arise of temperature and hence  $\epsilon'$  increases. However, in some cases, the value of  $\epsilon'$  may diminish when temperature rises, particularly in those substances in which ionic displacement intensifies the internal field and thereby electronic polarization.

In the low temperature region, in most cases the molecules cannot orient themselves in polar dielectrics. When the temperature rises, the orientation of dipole is facilitated and this increases  $\epsilon'$ . As the temperature rises the chaotic thermal oscillations of molecules are intensified and the degree of orderliness of their orientation is decreased.

### **2.5.2 Dielectric loss**

Dielectric loss is a special type of friction. When an electric field is applied to a dielectric material, dielectric polarization occurs. The total polarization is the sum of various contributions, e.g. electronic polarization due to the relative displacement of electrons and nuclei, dipolar polarization due to orientation of dipoles, ionic polarization due to the relative displacement of ions and interfacial or Maxwell-Wagner polarization when there are boundaries between the components of a heterogeneous system. Each mechanism contributes to the polarization up to a given frequency. Above that frequency, its contribution can no longer contribute and lowers the dielectric constant. At very low frequencies the polarization easily follows the alternating field, thus its contribution to the dielectric constant is maximum and no loss occurs. But at high frequency the polarization begins to lag behind the electric field and energy is dissipated. An ideal dielectric would allow no flow of electronic charge, only a displacement of charge via polarization. If a plate of such ideal material is placed between the capacitive cell shown in Fig. 2.7 and a dc voltage is applied, the current through the circuit



would decay exponentially to zero with time. But this will not happen if an alternating (sine wave) electric field is applied. For real dielectric material, the current  $I$  has two vector components, real  $I_R$  and imaginary  $I_C$ . The condition of loss (not so good) is illustrated in Fig. 2.7(b) which is an equivalent circuit analogous of a resistance in parallel with the capacitor [35]. The current  $I_C$  represents a (watt less) capacitive current proportional to the charge stored in the capacitor. It is frequency dependent and leads the voltage by  $90^\circ$ . On the other hand, the current  $I_R$  is ac conduction current in phase with the voltage  $V$ , which represents the energy loss or power dissipated in the dielectric. The resultant angle between the current and the voltage is  $\varphi$  somewhat less than  $90^\circ$ . The current in real capacitor lags slightly behind what it would be in an ideal capacitor. The angle of lag is defined as  $\delta$  and the amount of lag becomes  $\tan\delta_E$  or loss tangent.

By definition,

$$\tan\delta = \left| \frac{I_C}{I_R} \right| = \frac{\epsilon''}{\epsilon'} \quad (2.13)$$

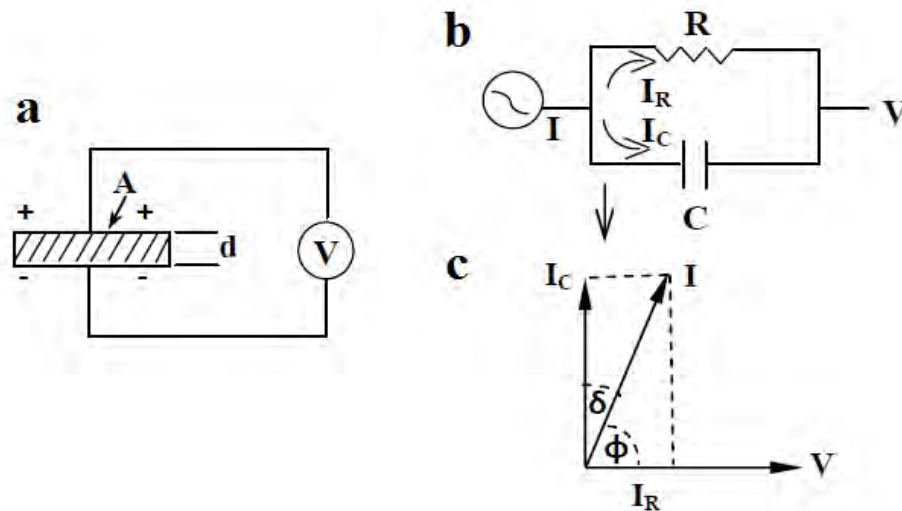


Fig. 2.7: Equivalent circuit diagrams: (a) capacitive cell, (b) charging loss current and (c) loss tangent [35].

### 2.5.2.1 Factors affecting dielectric losses

The  $\tan\delta_E$  is very sensitive to humidity. Hence the microwave measurements should be done in an air-conditioned room. The samples should be heated in an oven to remove the moisture before starting the experiments. For a low loss material, it should contain lowest possible concentration of dipoles and charge carriers with lowest possible mobility. However, it is a fact that most technically important insulating materials are far from very pure and often contain deliberate or accidental admixtures of substances which are necessary for their processing. The disordered charge distributions in the crystal lattice also contribute to dielectric loss. Dielectric losses occur if the charge distribution in the crystal deviates from perfect periodicity. In 1964, Schlomann reported that in ionic non-conducting crystals, the loss tangent increases when the ions are distributed disorderly in such a way that they break the periodic arrangement of atoms in the crystal [36]. The loss tangent depends strongly on the spatial correlation between charge deviations. He reported that the loss tangent is negligible if the disordered charge distribution in the crystal maintains the charge neutrality within a short range of the order of lattice constant.

The intrinsic quality factor ( $Q_i = 1/\tan\delta_E$ ) of any given material will vary with the frequency of measurements. For many materials the dielectric loss tangent almost linearly increases as the frequency increases. Hence often the intrinsic quality factor ( $1/\tan\delta_E$ ) is reported as  $Qif = f/\tan\delta_E$  (in GHz) since this value is the first approximation constant. Assumption that the value of  $Qif$  is constant is satisfied the best for the well-densified ceramics at certain limited frequency range. In practice, samples measured at higher frequencies (5–12 GHz) always give higher  $Qif$  values than the same material measured at lower frequencies of 1–3 GHz. This difference may be related to ceramic processing. The bigger samples resonating at lower frequencies statistically contain more imperfections than smaller ceramic pucks resonating at larger frequencies. The

presence of porosity decreases the quality factor due to the presence of moisture in the pores. Hence porous samples show an increase in  $Qf$  on warming up due to escape of trapped moisture.

There is no predictive theory to account for the microwave loss in dielectric ceramics. Hence the approach to find new dielectric resonator materials is largely done by trial and error method involving preparing and testing a large number of samples. This is a laborious and time consuming job. The quality factor is highly dependent not only on the intrinsic quality of the ceramic material, but also on the method of measurement, the measurement environment and the frequency at which the sample is measured. A given material sample may exhibit greatly differing quality factors when tested in different test fixtures and environments which may vary in size, shape, conductor quality, coupling, type of sample support, ambient temperature and relative humidity.

### **2.5.3 Dielectric strength**

An important aspect in considering the dielectric properties of a high-  $\epsilon'$  ceramic is its breakdown characteristics. This is sometimes referred to as the “strength” of a dielectric. There are three main breakdown mechanisms; thermal, electrical and discharge [37-39].

Thermal breakdown occurs when high frequency potentials are applied for a certain period of time. In this case, energy in the dielectric can be lost to heat, which results in an increase in the dissipation factor that in turn, generates more heat and causes a catastrophic breakdown event. Electrical breakdown occurs when a high enough electric field ( $10^6\sim 10^7$  V/cm) is applied. When subjected to an electric field, some electrons will gain enough energy to ionize other constituent ions, which leads to an avalanche effect due to the increasing number of electrons in the system. This is a result of the microstructure and grain size and is usually referred to as the “intrinsic”

strength. It has been shown that the dielectric strength of a material ( $DS$ ) is directly related to the thickness of the sample ( $d$ ), where  $V_B$  is the breakdown voltage [39].

$$DS = \frac{V_B}{d} \quad (2.14)$$

Discharge breakdown is similar to electrical breakdown but its cause is more specific. In this type of breakdown, the electric field is greater in a flaw than in the rest of the dielectric. This will cause the flaw to discharge, which leads to charge leakage and breakdown. Independent of the breakdown mechanism, the dielectric strength of a material is influenced by its composition, microstructure and testing conditions such as electrode configuration and sample thickness. By using thin films, the dielectric strength of a material can be increased dramatically due to more direct electrode contact with the dielectric and lower defect density. Now that the characteristics of energy storage have been discussed, the four main types of capacitors will be introduced.

## 2.6 Relaxation phenomena

Debye relaxation is a very simple model where only two polarizable species are assumed in the dielectric. Thus, the dielectric parameters will undergo a single relaxation time  $\tau$  which denotes the transition time between one species and the other one. Both are contributing to the dielectric response but at different frequencies. Let us take the example of a ceramics including two possible dielectric contributions; one from grain boundaries and the other from the grains. Each contribution is usually represented using the impedance diagram ( $-Z''$  vs.  $Z'$ ), as shown in Fig. 2.8 (b). They can also be represented by an equivalent circuit also depicted in Fig. 2.8. Both contributions can be easily distinguished with the impedance diagram but the relaxation process between them can only be evidenced using the *Cole-Cole* diagram [40-41] by plotting  $\epsilon_r''$  vs  $\epsilon_r'$ . Finally, it is important to note that if only one species is considered in the dielectric, no

mechanism of relaxation has to be expected (as shown in Fig. 2.8 (a)). The Debye relaxation is usually expressed in the complex permittivity  $\varepsilon$  of a medium as a function of the field frequency  $\omega$ :

$$\varepsilon(\omega) = \varepsilon_{\infty} + \frac{\varepsilon_s - \varepsilon_{\infty}}{1 + i\omega\tau} \quad (2.15)$$

Where  $\varepsilon_{\infty}$  is the high frequency permittivity,  $\varepsilon_s$  is the low frequency permittivity (static) and  $\tau$  describes the characteristic relaxation. In the case of a pure Debye relaxation the plot of  $\varepsilon_r'$  vs.  $\varepsilon_r''$  the frequency is shown in Fig. 2.9 (a).

Maxwell Wagner (MW) effect is commonly involved if a material is electrically heterogeneous. This dispersion occurs because of the charging of the interfaces within the material. This phenomenon does not arise from dielectric relaxation in the bulk phases of the material (which might also be present), but is a consequence of the boundary conditions on the fields at the interfaces between phases. Interfacial effects typically dominate the dielectric properties of doped-LaAlO<sub>3</sub>, when free charges induced by doping are located at the interfaces (grain boundaries, domain walls, electrodes). The typical Maxwell Wagner behavior is plotted in Fig. 2.9 (b). In a MW system, the real part is the same as in Debye relaxation. Analysis of the real part of relative permittivity is therefore not useful for identification of interfacial polarization effects. On the other hand, analysis of the imaginary permittivity does distinguish Debye from MW behavior.

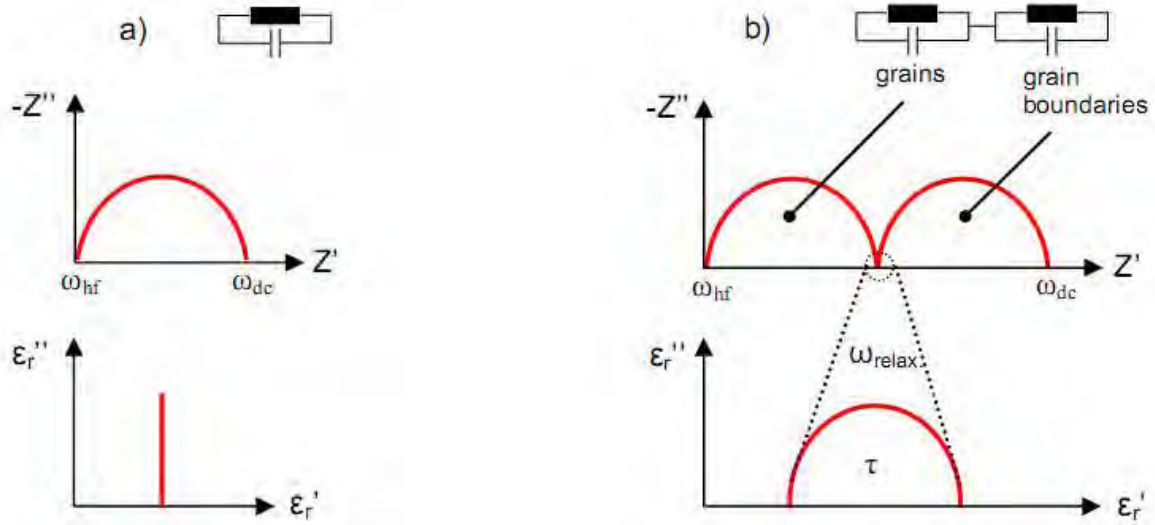


Fig. 2.8: Impedance diagrams (top) and Cole-Cole diagrams (bottom) for one polarizable specie in the dielectric a) and typical Debye relaxation with two polarizable species b). Impedance diagram is not an appropriate plot to observe the relaxation process [42].

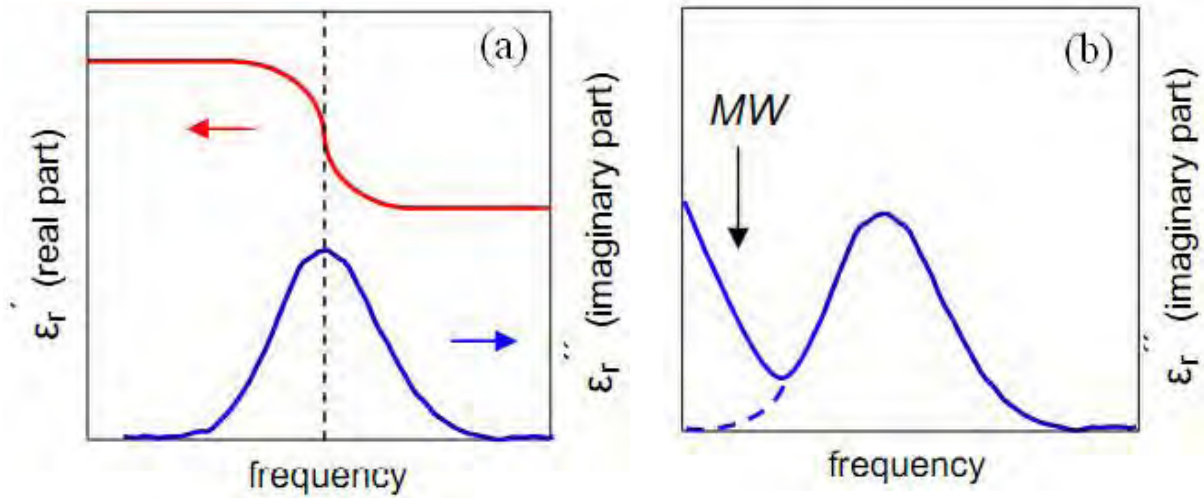


Fig. 2.9: (a) Frequency dependence of real and imaginary part for the case of Debye-type relaxation process. (b) Form of the imaginary permittivity response expected from both *Maxwell Wagner* and *Debye* models [42].

## 2.7 Magnetism

Magnetism is a class of physical phenomena that are mediated by magnetic fields. Electric currents and the magnetic moments of elementary particles give rise to a magnetic field, which acts on other currents and magnetic moments. The origin of the magnetic moments responsible for magnetization can be either microscopic electric currents resulting from the motion of electrons in atoms or the spin of the electrons or the nuclei [43]. Five basic types of magnetism can be described: diamagnetism, paramagnetism, ferromagnetism, antiferromagnetism and ferrimagnetism. In the presence of an externally applied magnetic field the atomic current loops created by the orbital motion of electrons respond to oppose the applied field. All materials display this type of weak repulsion to a magnetic field known as diamagnetism. Diamagnetism is observed in materials with filled electronic subshells where the magnetic moments are paired and overall cancel each other. All other types of magnetic behavior observed in materials are at least partially attributed to unpaired electrons in atomic shells, often in the 3d or 4f shells of each atom. Materials whose atomic magnetic moments are uncoupled display paramagnetism. The most familiar effects occur in ferromagnetic materials, which are strongly attracted by magnetic fields and can be magnetized to become permanent magnets, producing magnetic fields themselves. Only a few substances are ferromagnetic; the most common ones are iron, nickel and cobalt and their alloys. Materials having atomic magnetic moments of equal magnitude that arranged in an antiparallel fashion display antiferromagnetism. Ferrimagnetism is a property exhibited by materials whose atoms or ions tend to assume an ordered but nonparallel arrangement of moments in zero applied field below a certain characteristic temperature known as the Neel temperature. Different types of magnetism are illustrated in Fig. 2.10.

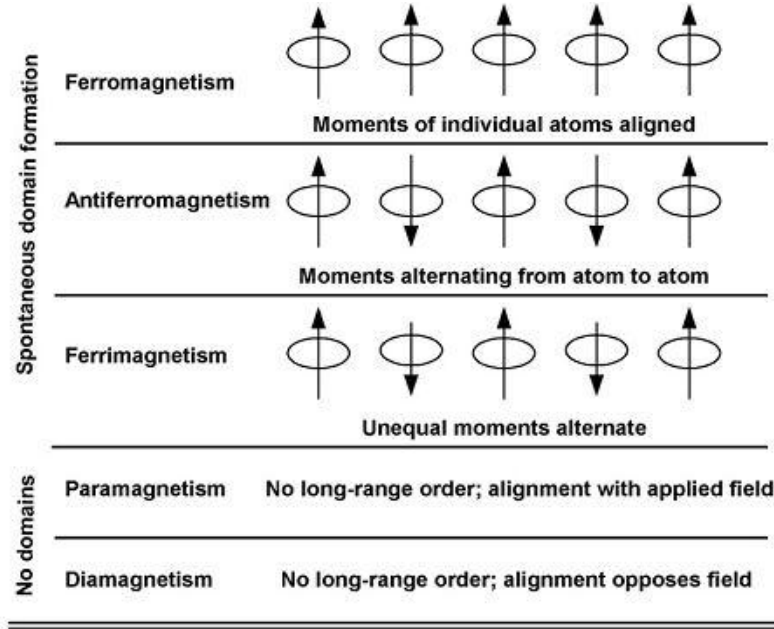


Fig. 2.10: Various types of magnetism.

### 2.7.1 Permeability

In electromagnetism, permeability is the measure of the ability of a material to support the formation of a magnetic field within itself [44]. Hence, it is the degree of magnetization that a material obtains in response to an applied magnetic field. Permeability is defined as the proportionality constant between the magnetic field induction  $B$  and applied field intensity  $H$ :

$$B = \mu H \quad (2.16)$$

If the applied field is very low, approaching zero, the ratio will be called the initial permeability  $\mu_i$ .

A useful tool for dealing with high frequency magnetic effects is the complex permeability. While at low frequencies in a linear material the magnetic field and the auxiliary magnetic field are simply proportional to each other through some scalar permeability, at high frequencies



these quantities will react to each other with some lag time. A magnetic material subjected to an ac magnetic field can be written as,

$$H = H_0 e^{i\omega t} \quad (2.17)$$

It is observed that the magnetic induction  $B$  lag behind  $H$ . This is caused by the presence of various losses and is thus expressed as,

$$B = B_0 e^{i(\omega t - \delta)} \quad (2.18)$$

Here  $\delta$  is the phase angle that marks the delay of  $B$  with respect to  $H$ . The permeability is then given by,

$$\mu = \frac{B}{H} = \frac{B_0 e^{i(\omega t - \delta)}}{H_0 e^{i\omega t}} = \frac{B_0 e^{-i\delta}}{H_0} \quad (2.19)$$

By Euler's formula, the complex permeability can be translated from polar to rectangular form,

$$\mu = \frac{B_0}{H_0} \cos \delta - i \frac{B_0}{H_0} \sin \delta = \mu' - i\mu'' \quad (2.20)$$

Where

$$\mu' = \frac{B_0}{H_0} \cos \delta \quad (2.21)$$

$$\mu'' = \frac{B_0}{H_0} \sin \delta \quad (2.22)$$

The real part  $\mu'$  of complex permeability ( $\mu$ ), as expressed in equation (2.20) represents the component of  $B$  which is in phase with  $H$ , so it corresponds to the normal permeability. If there are no losses, we should have  $\mu = \mu'$ . The imaginary part  $\mu''$  corresponds to that of  $B$ , which is delayed by phase angle  $90^\circ$  from  $H$ . The presence of such a component requires a supply of energy to maintain the alternating magnetization, regardless of the origin of delay.

The ratio of the imaginary to the real part of the complex permeability is called the loss tangent,

$$\tan \delta = \frac{\mu''}{\mu'} \quad (2.23)$$

Which provides a measure of how much power is lost in a material versus how much is stored.

This occurs due to the irreversible domain wall movements.

### References

- [1] Subramanian, M.A., Li, D., Duan, N., Reisner, B.A. and Sleight, A.W., "High dielectric constant in  $\text{ACu}_3\text{Ti}_4\text{O}_{12}$  and  $\text{ACu}_3\text{Ti}_3\text{FeO}_{12}$  phases," *Journal of Solid State Chemistry*, 151(2), pp.323-325, 2000.
- [2] J. Halblutzel, *Helv. Phys. Acta.* 12, 489, 1939.
- [3] Lines, M.E. and Glass, A.M., "*Principles and applications of ferroelectrics and related materials*," Oxford university press, 2001.
- [4] Fujimoto, M. and Kingery, W.D., "Microstructures of  $\text{SrTiO}_3$  internal boundary layer capacitors during and after processing and resultant electrical properties," *Journal of the American Ceramic Society*, 68(4), pp.169-173, 1985.
- [5] Yang, C.F., "Improvement of the sintering and dielectric characteristics of surface barrier layer capacitors by CuO addition," *Japanese journal of applied physics*, 35(3R), p.1806,1996.
- [6] Moulson, A.J., Herbert, J.M. and *Electroceramics*, C., Hall Ltd, 1990.

- [7] Starešinić, D., Biljaković, K., Lunkenheimer, P. and Loidl, A., “Slowing down of the relaxational dynamics at the ferroelectric phase transition in one-dimensional (TMTTF)  $2\text{AsF}_6$ ,” *Solid state communications*, 137(5), pp.241-245, 2006.
- [8] Schrettle, F., Lunkenheimer, P., Hemberger, J., Ivanov, V.Y., Mukhin, A.A., Balbashov, A.M. and Loidl, A., “Relaxations as key to the magnetocapacitive effects in the perovskite manganites,” *Physical review letters*, 102(20), p.207208, 2009.
- [9] Cross, L.E., “Relaxor ferroelectrics,” *Ferroelectrics*, 76(1), pp.241-267, 1987.
- [10] Bokov, A.A. and Ye, Z.G., “Recent progress in relaxor ferroelectrics with perovskite structure,” *Journal of materials science*, 41(1), pp.31-52, 2006.
- [11] Viehland, D., Jang, S.J., Cross, L.E. and Wuttig, M., “Freezing of the polarization fluctuations in lead magnesium niobate relaxors,” *Journal of Applied Physics*, 68(6), pp.2916-2921, 1990.
- [12] Westphal, V., Kleemann, W. and Glinchuk, M.D., “Diffuse phase transitions and random-field-induced domain states of the “relaxor” ferroelectric  $\text{PbMg}_{1/3}\text{Nb}_{2/3}\text{O}_3$ ,” *Physical Review Letters*, 68(6), p.847, 1992.
- [13] Vugmeister, B.E. and Rabitz, H., “Dynamics of interacting clusters and dielectric response in relaxor ferroelectrics,” *Physical Review B*, 57(13), p.7581, 1998.
- [14] Portengen, T., Östreich, T. and Sham, L.J., “Theory of electronic ferroelectricity,” *Physical Review B*, 54(24), p.17452, 1996.
- [15] Batista, C.D., “Electronic ferroelectricity in the Falicov-Kimball model,” *Physical review letters*, 89(16), p.166403, 2002.

- [16] Kampf, A.P., Sekania, M., Japaridze, G.I. and Brune, P., “Nature of the insulating phases in the half-filled ionic Hubbard model,” *Journal of Physics: Condensed Matter*, *15*(34), p.5895, 2003.
- [17] Ikeda, N., Ohsumi, H., Ohwada, K., Ishii, K., Inami, T., Kakurai, K., Murakami, Y., Yoshii, K., Mori, S., Horibe, Y. and Kitô, H., “Ferroelectricity from iron valence ordering in the charge-frustrated system  $\text{LuFe}_2\text{O}_4$ ,” *Nature*, *436*(7054), p.1136, 2005.
- [18] Monceau, P., Nad, F.Y. and Brazovskii, S., “Ferroelectric Mott-Hubbard phase of organic  $(\text{TMTTF})_2\text{X}$  conductors,” *Physical review letters*, *86*(18), p.4080, 2001.
- [19] Müller, K.A. and Burkard, H., “ $\text{SrTiO}_3$ : An intrinsic quantum paraelectric below 4 K,” *Physical Review B*, *19*(7), p.3593, 1979.
- [20] Viana, R., Lunkenheimer, P., Hemberger, J., Böhmer, R. and Loidl, A., “Dielectric spectroscopy in  $\text{SrTiO}_3$ ,” *Physical Review B*, *50*(1), p.601, 1994.
- [21] Dumas, J., Schlenker, C., Marcus, J. and Buder, R., “Nonlinear Conductivity and Noise in the Quasi One-Dimensional Blue Bronze  $\text{K}_{0.30}\text{MoO}_3$ ,” *Physical Review Letters*, *50*(10), p.757, 1983.
- [22] Grüner, G., “The dynamics of charge-density waves,” *Reviews of modern physics*, *60*(4), p.1129, 1988.
- [23] Fleming, R.M., Cava, R.J., Schneemeyer, L.F., Rietman, E.A. and Dunn, R.G., “Low-temperature divergence of the charge-density-wave viscosity in  $\text{K}_{0.30}\text{MoO}_3$ ,  $(\text{TaSe}_4)_2\text{I}$ , and  $\text{TaS}_3$ ,” *Physical Review B*, *33*(8), p.5450, 1986.

- [24] Cava, R.J., Littlewood, P., Fleming, R.M., Dunn, R.G. and Rietman, E.A., “Low-frequency dielectric response of the charge-density wave in  $(\text{TaSe}_4)_2\text{I}$ ,” *Physical Review B*, 33(4), p.2439, 1986.
- [25] Long, A.R., “Frequency-dependent loss in amorphous semiconductors,” *Advances in physics*, 31(5), pp.553-637, 1982.
- [26] Elliott, S.R., “Physics of amorphous materials,” *Longman Group, Longman House, Burnt Mill, Harlow, Essex CM 20 2 JE, England, 1983.*
- [27] Jonscher, A.K., “The ‘universal’ dielectric response,” *nature*, 267(5613), p.673, 1977.
- [28] Jonscher, A.K., “Chelsea dielectric press,” *London, Google Scholar, 1983.*
- [29] Mott, N.F. and Davis, E.A., “*Electronic processes in non-crystalline materials*,” Oxford university press, 2012.
- [30] Castner, T.G., “The dielectric anomaly as the insulator-metal transition is approached from the insulating side,” *Philosophical Magazine B*, 42(6), pp.873-893, 1980.
- [31] Hess, H.F., DeConde, K., Rosenbaum, T.F. and Thomas, G.A., “Giant dielectric constants at the approach to the insulator-metal transition,” *Physical Review B*, 25(8), p.5578, 1982.
- [32] Mott, N.F. and Transitions, M.I., Taylor and Francis, 1990.
- [33] Callister, W. D, J., “Materials Science and Engineering, An Introduction”, 5th edition, John Wiley & Sons, 2005.
- [34] Waser, R., “Nanoelectronics and information technology,” John Wiley & Sons, 2005.

- [35] Miah, M. J., “Study of Multiferroic Properties of Rare Earth Substituted  $x\text{Ba}_{0.95}\text{Sr}_{0.05}\text{TiO}_3-(1-x)\text{BiFe}_{0.9}\text{Re}_{0.1}\text{O}_3$  Perovskite Ceramics,” Ph. D. Thesis, Department of Physics, Bangladesh University of Engineering and Technology, 2016.
- [36] Sebastian, M.T., “*Dielectric materials for wireless communication*,” Elsevier, 2010.
- [37] Jaffe, B., Cook, W. R., and Jaffe, H., “Piezoelectric Ceramics”, Academic Press, London, 1971.
- [38] Buchanan, R. C., “Ceramic Materials for Electronics”, Marcel Dekker, Inc, New York, 2004.
- [39] Moulson, A. J., Herbert, J. M., “Electroceramics: Materials, Properties, Applications”, 2nd edition, John Wiley & Sons, London, 2003.
- [40] Cole, K. S., and Cole, R. H., “Dispersion and Absorption in Dielectrics I. Alternating Current Characteristics”, J. Chem. Phys., **9**, 341-351, 1941.
- [41] Cole, K. S., and Cole, R. H., “Dispersion and absorption in dielectrics II. Direct current characteristics”, J. Chem. Phys. **10**, 98-105, 1942.
- [42] Arveux, P. E., “Surface and interface properties of  $\text{BaTiO}_3$  ferroelectric thin films studied by in-situ photoemission spectroscopy”, Ph. D thesis, Material science, L’UNIVERSITÉ BORDEAUX 1, 2009.
- [43] Chikazumi, S. and Graham, C.D., Physics of Ferromagnetism. (International Series of Monographs on Physics; 94). Oxford University Press, 1997.
- [44] “Permeability (Electromagnetism).” Wikipedia, Wikimedia Foundation, [en.wikipedia.org/wiki/Permeability-\(electromagnetism\)](https://en.wikipedia.org/wiki/Permeability-(electromagnetism)), 20 Feb. 2019.

## CHAPTER 3

### METHODOLOGY OF SAMPLE PREPARATION

The most of the important properties needed for polycrystalline ceramics applications are not only intrinsic but also extrinsic, so the preparation of polycrystalline ceramics samples has to encounter additional complexity day by day. The properties of polycrystalline ceramics materials are strongly influenced by preparation methodology. The preparation of polycrystalline ceramics with optimum desired properties is still a complex and difficult task [1-5]. Therefore, the knowledge of preparation and the control of the chemical composition, homogeneity and microstructure are very crucial. There are several techniques available in the literature for the synthesis of ceramic samples.

#### 3.1 Sample Preparation Techniques

There are basically two approaches for sample preparation [6].

1. The chemical method.
2. The mechanical method.

The mechanical methods can be divided into two types,

- a. High energy ball milling.
- b. Solid state reaction technique or mixed oxide process.

Similarly, the following chemical methods are generally used for the synthesis of ceramics materials.

- a. Auto-combustion technique.
- b. Sol-gel method.

- c. Hydrothermal method.
- d. Co-precipitation technique, etc.

Both the mechanical and chemical methods have some advantages and disadvantages. The advantages of the mechanical methods include large-scale production of bulk ceramic powder at low cost and comparatively easy adaptability. However, in the conventional solid-state reaction method the particles are being coarse due to the high temperature and heating for long time [6]. Chemical methods are generally used to prepare fine powder with improved homogeneity and densification. The chemical precursors used in the sample preparation process can simply be refined to enhance the purity of the desired composition. It is also easy to control the stoichiometry and particle size with less processing time. However, the chemical techniques are generally complex than the conventional solid-state route and the large-scale production is sometimes difficult.

In this thesis, the most economical and comparatively simple mixed oxide process (conventional solid-state reaction technique) is used for preparing the different compositions of  $\text{LaAlO}_3$  based ceramics.

### **3.2 Standard solid state reaction technique**

The solid-state reaction method is the most widely used technique for the synthesis of polycrystalline materials from a mixture of solid starting materials. It is a direct reaction technique between the starting raw materials (usually powders). At room temperature, solids do not react together. High temperature (often 800 to 1600 °C) is required to take place the reaction at an appreciable rate. There are several factors on which the rate of reaction and feasibility depend including structural properties of the reactants, reaction conditions, surface area of the solids, reactivity of solids, and change of the thermodynamic free energy associated with the



reaction [7, 8]. Solid-state reaction is generally slow because during the reaction process a large number of bonds break and the ions migrate through a solid unlike gas phase and solution reactions [6]. Diffusion acts as the limiting factor in solid state reaction. So by controlling the diffusion of the cations through the product layer the solid state reaction rate can be controlled. The reaction takes place more quickly with the increase of temperature and reaction does not take place until the reaction temperature reaches at least two third of the melting point of one of the reactants [6]. The basic steps involved in the solid state reaction method are discussed below.

### 3.2.1 Reagents

Reagents are the solid reactants which are used to prepare a solid sample. The selected raw materials are first weighed out according to the stoichiometry of the compound. In this case, the impurity and moisture content should be taken into consideration. Before weighing the reactants should be dried thoroughly.

### 3.2.2 Mixing

After weighing the required amount of raw materials, they are mechanically mixed and then grind to control the particle size and for making the mixture homogeneous. For this purpose milling operation is carried out which can reduce the particle size to 1-10  $\mu\text{m}$  range [9].



Fig. 3.1: Balance, mortar and pestle.

For mixing small amount of reactants, generally an agate mortar and pestle are used as shown in Fig. 3.1. Sometimes volatile organic liquid (acetone or alcohol) is used to make the mixture more homogeneous. During the mixing and grinding process the organic liquid volatilizes gradually and evaporates completely after 10 to 15 minutes. Ball milling process is adopted when the quantity of raw materials are much larger than 20 to 25 gm. Since increase in surface area may increase the reaction rate, fine grained materials should be used.

### 3.2.3 Calcination

Next step is the solid state reaction between the constituents of the raw materials at suitable high temperature. This process is known as firing or calcinations. Calcination is typically a chemical reaction technique during which either complete or partial phase of the material is formed. During the calcinations process the unwanted gases and impurities are removed from the desired composition. It also helps in homogenization of the powder sample and reducing the shrinkage. Calcination causes the constituents to interact by inter diffusion of their ions and resulting in a homogeneous body. The control over the stoichiometry is necessary during the calcinations process and for it, volatile constituents should be compensated. This thermal treatment process can be carried out in the absence or limited supply of air. Calcination reactions occur at or above the thermal decomposition temperature of the constituent starting materials. This reaction takes place at temperature below the melting points of the raw materials [10]. The calcinations temperature is the temperature at which the standard Gibbs free energy for a particular calcination reaction is equal to zero [11]. The calcination temperature for a desired composition can be selected from the thermogravimetric analysis (TGA), differential thermal analysis (DTA) and the differential thermogravimetric analysis (DTG). In general, the calcination of raw materials is involved with four physical processes [6].

1. Linear expansion of the particles ( $< 400\text{ }^{\circ}\text{C}$ )
2. Solid phase reaction ( $400\text{ to }750\text{ }^{\circ}\text{C}$ )
3. Contraction of product ( $750\text{ to }850\text{ }^{\circ}\text{C}$ )
4. Grain growth ( $> 850\text{ }^{\circ}\text{C}$ )

A programmable furnace is typically used for the high temperature heat treatment. Crucible or boat can be used as container of sample. However, it is important to choose a suitable container material. The container material should be chemically inert to the reactants under the heating conditions used. A typical diagram of the container of sample and a programmable furnace are illustrated in Fig. 3.2.

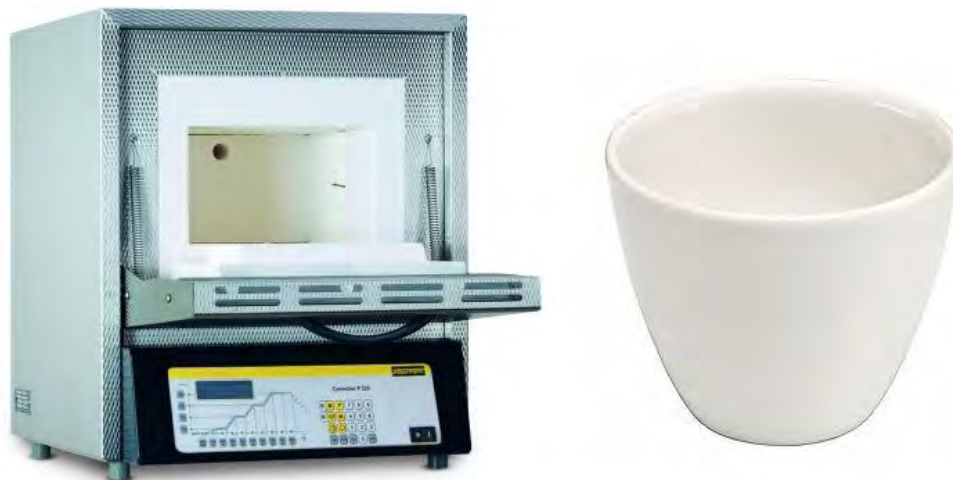


Fig. 3.2: Typical diagram of a crucible and a programmable electric furnace.

### 3.2.4 Green body preparation

Before further shaping the calcined powder is grind or ball milled again for few hours. Usually, the calcined powder is mixed with an organic binder (Polyvinyl alcohol- PVA) for making the sample more strengthened so that handling of the sample between the shaping and sintering process may not be difficult. It is very important that to choose such a reagent as binder which is

removable from the pressed sample after sintering without any disruptive effect. There are various methods available for shaping powder sample. These are,

1. Uniaxial pressing
2. Isostatic pressing
3. Extrusion
4. Calendering
5. Jiggering
6. Band casting
7. Silk screening
8. Slip casting
9. Injection moulding

However, in the present work uniaxial pressing technique is used among these different shaping methods.

### **3.2.5 Uniaxial pressing**

Uniaxial pressing is used to make compacts of small sizes with simple shapes of the calcined powder. It is carried out in a die having movable top. A cavity is formed at the bottom in lower portion. This cavity is filled with free flowing granulated powder and then it is struck with the top of the die. With the help of the top-punch, pressure in the range of 4000 to 8000 psi is applied by a Hydraulic press. A lot of care at various levels of mixing is needed while using this pressing technique, as samples prepared by this technique show the mechanical cracks and layering after sintering. Highly polished die and punch surfaces help to reduce wall friction and

tools are made of hardened steels to minimize wear and maintain surface finish. The process is shown in Fig. 3.3.

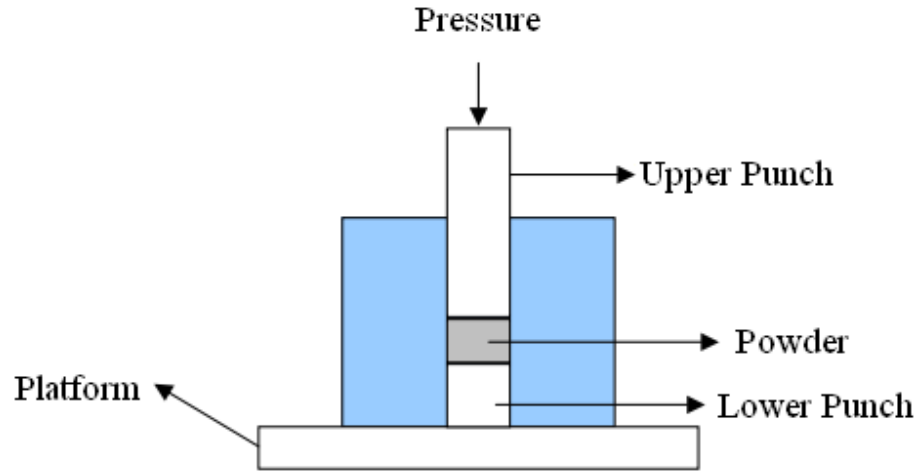


Fig. 3.3: Uniaxial pressing.

### 3.2.6 Sintering

Sintering is the process of compacting and forming a solid mass of material by heat or pressure without melting it to the point of liquefaction. It is the process in which the green compacts are generally consolidated into strong and dense polycrystalline aggregates [6]. During sintering at an appreciable temperature, the atomic motion is more violent and the area between grains in contact increases due to the thermal expansion of the grains and finally only one interface between two grains remains. This corresponds to a state with much lower surface energy. In this state, the atoms on the grain surfaces are affected by neighboring atoms in all directions, which results in densified ceramic [10]. Sintering is effective when the process reduces the porosity and enhances properties such as strength, electrical conductivity, translucency, thermal conductivity etc.

Coble and Burke derived an empirical relationship regarding the rate of grain growth with sintering time given as follows [12],

$$D = kT^n \quad (3.1)$$

Where  $D$  stands for the mean grain diameter,  $n$  is about  $1/3$ ,  $T$  is the sintering time and  $k$  is a temperature dependent parameter. Sintering can be divided into three stages as shown in Fig. 3.4.

Stage-1: Contact area between particles increases,

Stage-2: Porosity changes from open to close porosity,

Stage-3: Pore volume decreases and grains begin to grow.

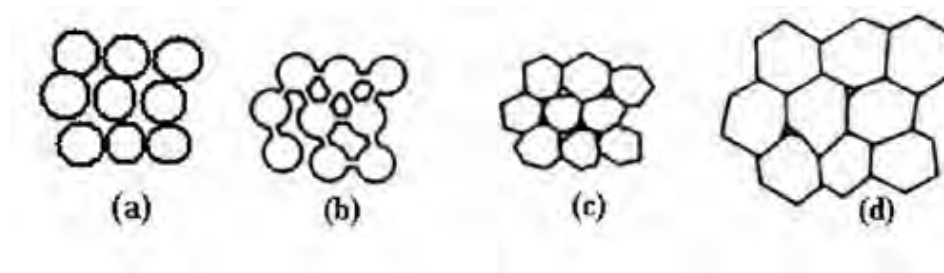


Fig. 3.4: Schematic representation of sintering stages: (a) green body, (b) initial stage, (c) intermediate stage and (d) final stage [13].

At the beginning of the sintering process, at high temperature, the lattice distortion and internal strain are reduced by atomic diffusion. This is known as the recovery process. When the temperature increases further, a recrystallization process occurs through atomic diffusion. During recrystallization, new crystal nuclei form and grow at grain boundaries and in other regions inside the grain with higher free energies. Meanwhile some grains grow by swallowing up other smaller grains. In the recrystallization stage grain growth is usually realized through the motion of

grain boundaries. Generally, higher the sintering temperature, larger the grains would grow, as the grain growth is caused by atomic diffusion, which increases with the increase in sintering temperature. However, if the sintering time is too long or the sintering temperature is so high, the density of the sample may be reduced due to the formation of larger grains.

### 3.2.7 Preparation of the Present Samples

The conventional solid state reaction technique is used for synthesizing the (Ca, Mn) co-doped  $\text{LaAlO}_3$  ceramics with formula  $\text{LaAl}_{0.67-x}\text{Ca}_x\text{Mn}_{0.33}\text{O}_3$  where ( $x=0.00, 0.02, 0.04, 0.05$ ).  $\text{La}_2\text{O}_3$  ( $\geq 99.9\%$ ),  $\text{Al}_2\text{O}_3$  ( $\geq 99.9\%$ ),  $\text{MnCO}_3$  ( $\geq 99.9\%$ ) and  $\text{CaCO}_3$  ( $\geq 99.99\%$ ) are taken as the starting materials (raw materials). Stoichiometric amounts of the raw materials (powder form) are properly mixed in an agate mortar by hand milling for about 6 hours. Acetone (Propanone) is used as a volatile organic liquid for making the mixer more homogeneous. During the mixing and grinding process acetone volatilizes gradually and evaporates completely after 10 to 15 minutes. After grinding and mixing properly, the dried powders are then calcined in an alumina crucible by using a programmable electric furnace at 1273 K for 5 hours in the air with a heating and cooling rate of about 10 and 5 °C/min, respectively. The calcined powder is then re-milled for 4 hours for ensuring proper homogenization. Finally, the dried fine powders are used to prepare the disc shaped pellet and toroid shaped green body by applying uniaxial pressure of 4000 psi for 1 min through a hydraulic press. Typically 0.90 gm and 0.80 gm fine powder is used to make each pellet and toroid shaped green body, respectively. A small drop of poly vinyl alcohol (PVA) is mixed as a binder for preparing each of the green body. The green samples are then sintered at 1723 K in the air for burning out the PVA and densification. The sintered samples are then polished to remove roughness of the surface and any oxide layer formed during the sintering process.

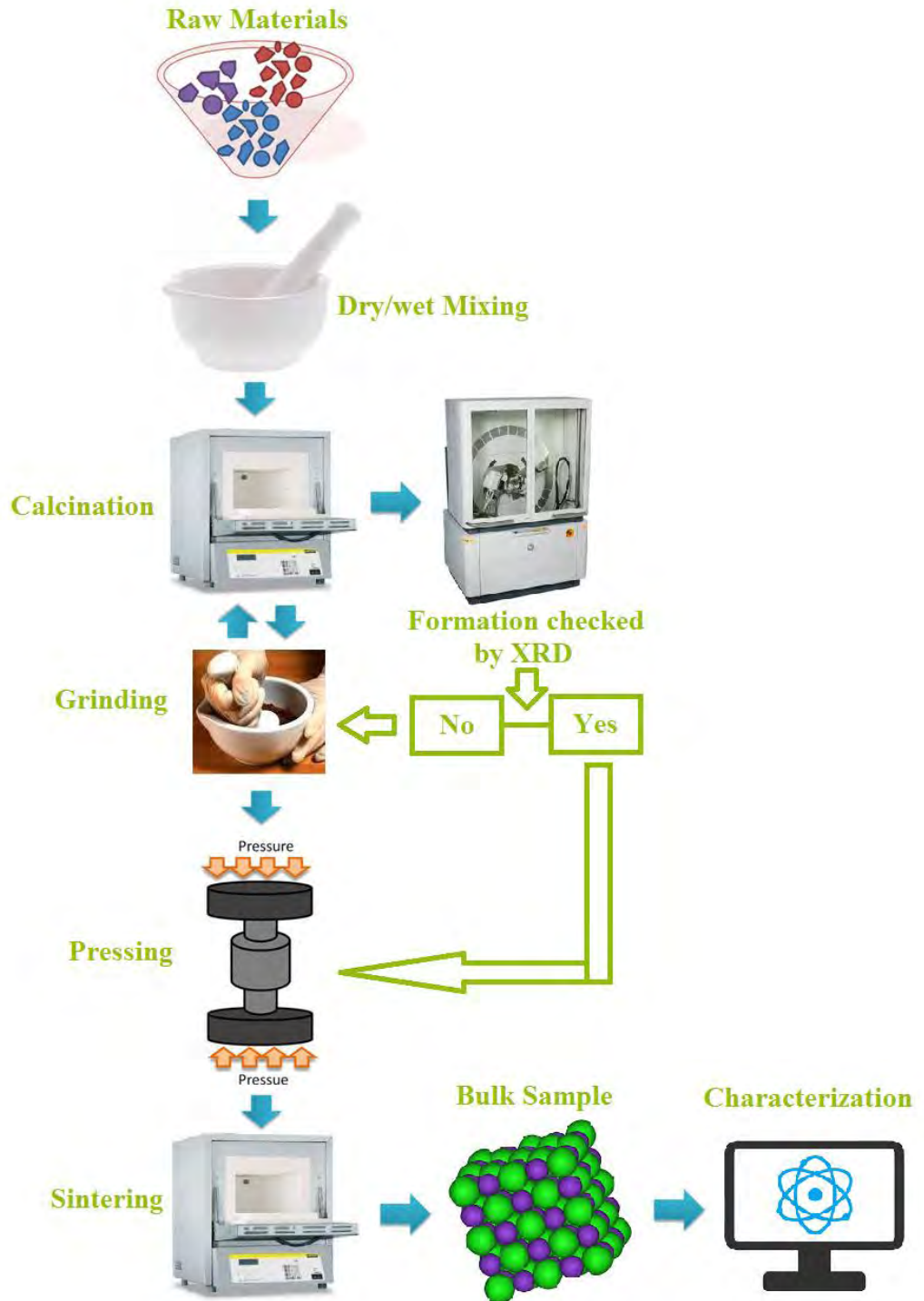


Fig. 3.5: Graphical representation for the synthesis of ceramics samples by the solid-state reaction route.



**References**

- [1] Haertling, G.H., “Ferroelectric ceramics: history and technology”, *Journal of the American Ceramic Society*, 82(4), pp.797-818, 1999.
- [2] Kingery, W.D., Bowden, H.K. and Uhlmann, D.R., “Wiley Series on the Science and Technology of the Materials”, *Introduction to Ceramics*, 1976.
- [3] Lines, M.E. and Glass, A.M., “*Principles and applications of ferroelectrics and related materials*”, Oxford university press, 2001.
- [4] Burfoot, J.C. and Taylor, G.W., “*Polar dielectrics and their applications*”, Univ of California Press, 1979.
- [5] Takasu, H., “The ferroelectric memory and its applications”, *Journal of Electroceramics*, 4(2-3), pp.327-338, 2000.
- [6] Shah, M. R., Dielectric properties of alkaline earth (D = Ba, Sr, Ca) and rare earth (T = La, Nd) substituted polycrystalline  $D_{1-x}T_x(\text{Ti}_{0.5}\text{Fe}_{0.5})\text{O}_3$  perovskite, Ph. D. Thesis, Department of Physics, Bangladesh University of Engineering and Technology, 2013.
- [7] West, A.R., “*Solid state chemistry and its applications*”, John Wiley & Sons, 2014.
- [8] Gerand, B., Nowogrocki, G., Guenot, J. and Figlarz, M., “Preparative methods in Solid State Chemistry”, 1989.
- [9] Moulson, A.J. and Herbert, J.M., “*Electroceramics: materials, properties, applications*”, John Wiley & Sons, 2003.
- [10] Xu, Y., “*Ferroelectric materials and their applications*”, Elsevier, 2013.

- [11] “Calcination.” Wikipedia, Wikimedia Foundation, 18 Nov. 2018, en.wikipedia.org/wiki/Calcination.
- [12] Coble, R. L. and Burke, J. E., “On the reactivity of solids”, 4th Int. Symp., 30 May-4 June, Amsterdam, pp. 38-51, 1960.
- [13] Miah, M. J., “Study of Multiferroic Properties of Rare Earth Substituted  $x\text{Ba}_{0.95}\text{Sr}_{0.05}\text{TiO}_3-(1-x)\text{BiFe}_{0.9}\text{Re}_{0.1}\text{O}_3$  Perovskite Ceramics”, Ph. D. Thesis, Department of Physics, Bangladesh University of Engineering and Technology, 2016.

## CHAPTER 4

### EXPERIMENTAL TECHNIQUES

The basic principles of the experimental setup used in this thesis will be introduced in this chapter. A detailed review of how such techniques are used for further improvement of the dielectric properties of  $\text{LaAlO}_3$  based ceramics will also be discussed.

#### 4.1 Structural and Morphological Characterization

Phase identification and structural analysis of the investigated samples are carried out by using X-ray diffractometer. Surface morphology of all the samples is investigated by using the Field Emission Scanning Electron Microscope (FESEM). The basic principles of these techniques are discussed in the following sections.

##### 4.1.1 X-ray diffraction

X-ray diffraction (XRD) is considered as a one of the most crucial non-destructive tools for analyzing all kinds of objects ranging from fluids to powders and solids. XRD is an indispensable technique for the characterization of novel materials. XRD methods are widely used to identify crystalline phases of various materials and superior in elucidating the three dimensional atomic structure of crystalline materials. The basic properties and functions of solids largely depend upon the crystal structures. Therefore, X-ray diffraction technique is an essential means in materials research, development and production.

X-ray diffraction is a phenomenon in which the atoms of a crystalline solid, by virtue of their uniform atomic spacing, cause interference pattern of the waves present in an incident beam of X-rays. Crystalline solids are generally periodic or regular arrays of atoms. X-rays can be

regarded as waves of electromagnetic radiation. The X-ray waves are scattered primarily by the electrons of the atom. It can be considered just like an ocean wave which is striking a lighthouse producing secondary circular waves originating from the lighthouse [1]. Similarly, an X-ray strikes an electron of an atom and produces spherical secondary waves emanating from the electron. This phenomenon is generally called elastic scattering and the lighthouse/electron is known as the scatterer. A periodic array of scatterers generates a periodic array of spherical waves. Through the destructive interference these waves cancel one another out in most directions. However, in a few specific directions they are added constructively which is determined by Bragg's law [2],

$$2d \sin\theta = n\lambda \quad (4.1)$$

Where  $d$  denotes the spacing between diffracting planes,  $n$  is an integer,  $\theta$  is the incident angle, and  $\lambda$  stands for the wavelength of the incident X-ray beam. These specific directions appear as spots on the diffraction pattern which is known as reflections [1]. An example of X-ray diffraction mechanism is shown in Fig. 4.1.

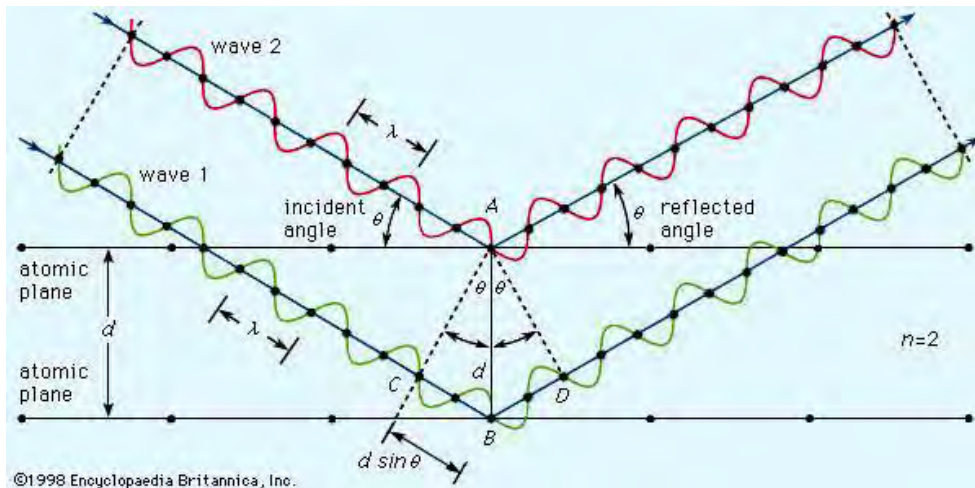


Fig. 4.1: Graphical representation of X-ray diffraction technique [3].

For producing significant diffraction, the wavelength of the striking wave should be similar in size with the spacing between the scatterers. X-rays are typically used to generate the diffraction pattern because the wavelength of X-ray is typically the same order of magnitude (1-100 angstroms) with the spacing between planes in the crystalline solid [1]. According to the Bragg's law, diffraction is only possible when  $\lambda \leq 2d$  [2]. This is the reason why visible light can not be used to determine the crystal structure of a material. For cubic structure  $d$  is given by,

$$\frac{1}{d^2} = \frac{h^2+k^2+l^2}{a^2} \quad (4.2)$$

Combining the two equations a relation can be obtained which defines the diffraction angle for any set of planes for a given  $\lambda$  if the following condition is satisfied,

$$\sin^2\theta = \frac{\lambda^2(h^2+k^2+l^2)}{4a^2} \quad (4.3)$$

Similarly, we can have relations for other crystal systems such as tetragonal, orthorhombic etc.

In this thesis, the crystal structure and phase purity of the studied compositions are investigated by using an advanced X-ray diffractometer (Model-Philips PANalytical X'PERT-PRO, Cu-K $\alpha$  is used as target with incident wavelength,  $\lambda = 1.540598 \text{ \AA}$ ). A schematic diagram for X-ray powder diffraction (XRD) experiment is shown in Fig. 4.2. A typical X-ray diffractometer is shown in Fig. 4.3.

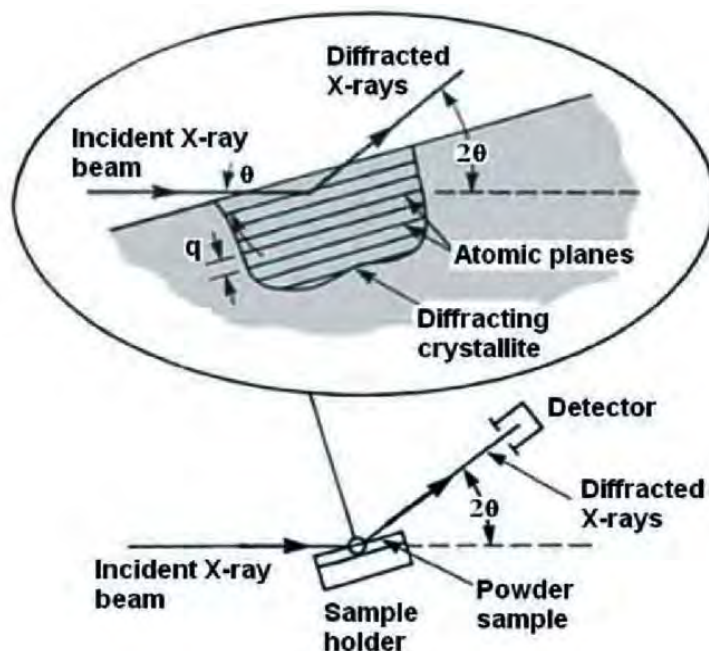


Fig. 4.2: Schematic diagram for a typical X-ray powder diffraction experiment [4].



Fig. 4.3: A typical X-ray diffractometer used for XRD [5].

The average crystallite size of the selected compositions is estimated from the width of the XRD peak by using the Scherrer equation given as follows,

$$D = \frac{0.9\lambda}{\beta \cos\theta} \quad (4.4)$$

Where  $D$  denotes the average crystallite size,  $\lambda$  is the wavelength of X-ray,  $\theta$  is the angle of the incident beam and  $\beta$  is the line broadening at half the maximum intensity (FWHM), after subtracting the instrumental line broadening, in radians. From the XRD data the lattice parameter of a cubic structural sample can be calculated by using Eq. (4.2). However, for a hexagonal structure the following equation is used.

$$\frac{1}{d^2} = \frac{4}{3} \left( \frac{h^2 + hk + k^2}{a^2} \right) + \frac{l^2}{c^2} \quad (4.5)$$

Now for determining the precise lattice parameter of a sample the Nelson-Riley method is used [6]. The Nelson-Riley function is given by,

$$F(\theta) = \frac{1}{2} \left[ \frac{\cos^2\theta}{\sin\theta} + \frac{\cos^2\theta}{\theta} \right] \quad (4.6)$$

The values of lattice constant of all the peaks for a sample are plotted against  $F(\theta)$ . Then by using a least square fit method exact lattice parameter can be determined. The point where the least square fit straight line cut the y-axis (i.e. at  $F(\theta) = 0$ ) is the actual lattice parameter of the sample.

#### 4.1.2 Microstructural studies by SEM/FESEM

The surface morphology of the sintered samples can be investigated by using a high resolution optical microscope, Scanning Electron Microscope (SEM), Field Emission Scanning Electron Microscope (FESEM) and Transmission Electron Microscope (TEM). Scanning Electron

Microscopy (SEM) has been a powerful and popular tool for materials surface characterization. Electrons are used in electron microscope just like as the light or optical microscope which uses visible light for imaging. A scanning electron microscope (SEM) is a microstructure analysis tool which generates image of a sample by scanning the surface of the sample with a focused beam of electrons. The type of signals generated in SEM varies and can include characteristic X-rays, secondary electrons, and back scattered electrons. Fig. 4.4 shows the type of signals produced in SEM and the area from which they are produced. The most general SEM mode is the detection of secondary electrons that are emitted by the atoms of the sample excited by the incident electron beam. The resolution of SEM image is better than that of a light microscope since the wavelength of electrons is much smaller than the wavelength of light. The resolution of SEM image can be better than one nanometer [7].

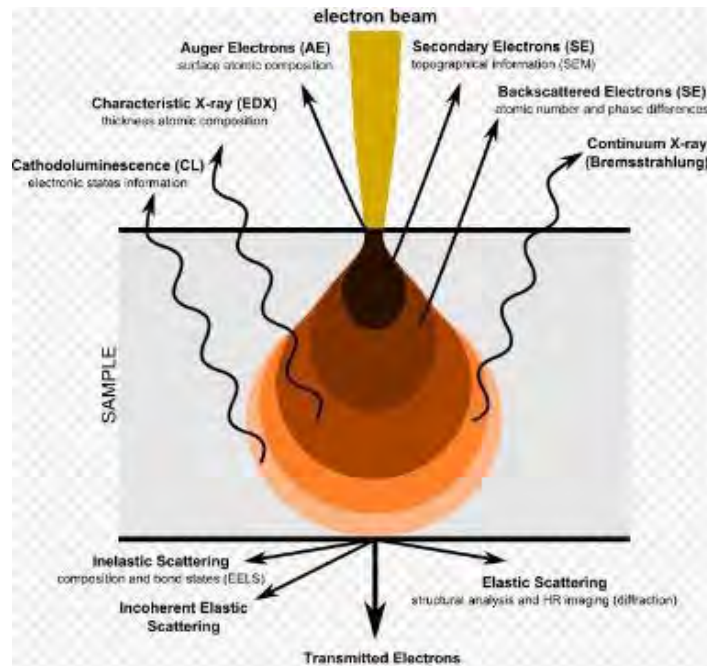


Fig. 4.4: Various types of signals which are generated by electron-matter interactions [8].



In a typical SEM, an electron gun is fitted with a tungsten filament cathode from which an electron beam is emitted. Because of having highest melting point and lowest vapor pressure of all metals tungsten is generally used in thermionic electron gun. The electron beam, which typically has an energy ranging from 0.2 KeV to 40 KeV, is focused by one or two condenser lenses to a spot about 0.4 nm to 5 nm in diameter. The beam passes through pairs of scanning coils or pairs of deflector plates in the electron column, typically in the final lens, which deflect the beam in the  $x$  and  $y$  axes so that it scans in a raster fashion over a rectangular area of the sample surface [7]. When the primary electron beam interacts with the sample, the electrons lose energy by repeated random scattering and absorption within a teardrop-shaped volume of the specimen known as the interaction volume, which extends from less than 100 nm to approximately 5  $\mu\text{m}$  into the surface. The energy exchange between the sample and electron beam results in the reflection of high-energy electrons by elastic scattering, emission of secondary electrons by inelastic scattering and the emission of electromagnetic radiation, each of which can be detected by specialized detectors. Electronic amplifier is used to amplify the signals, which are displayed as variations in brightness on a computer monitor. Each pixel of computer video memory is synchronized with the position of the beam on the specimen in the microscope, and the resulting image is, therefore, a distribution map of the intensity of the signal being emitted from the scanned area of the specimen [7]. For SEM, the sample is first made conductive for current. This is done by coating the sample with an extremely thin layer (1.5 - 3.0 nm) of gold or gold-palladium.

Field emission scanning electron microscope (FESEM) is another microstructure analysis tool just like as SEM, provides many useful information from the surface of a sample with higher resolution and much greater energy range than that of SEM. As like as SEM electron beam is used for scanning the sample surface. The main difference between a typical SEM and FESEM is the electron beam generation system. A field emission gun is used as a source of electrons in FESEM that produces extremely focused electron beam. For this reason, spatial resolution is improved greatly that enables the function to be performed at very low potentials (0.02-5 KV) [9].



Fig. 4.5: Field emission scanning electron microscope (FESEM) setup.

In FESEM, Electrons are emitted from a field emission source. They are accelerated in a high electrical field gradient. Within the high vacuum column these so-called primary electrons are focused and deflected by electronic lenses to produce a narrow scan beam that bombards the object. As a result secondary electrons are emitted from every spot on the object. The velocity and angle of these secondary electrons are related to the surface structure of the sample. A detector catches the secondary electrons and produces an electronic signal which is amplified and transformed to a video scan-image that can be seen on a monitor or to a digital image that can be saved and processed further.

The average grain size is evaluated by using the linear intercept technique through the relation,  $D = 1.56L$  [10]; where  $D$  stands for average grain size, and  $L$  is the average intercept length over a large number of grains as measured on the plane of the sample. For finding out the average intercept length several random vertical and horizontal lines are drawn on the micrograph of the selected sample. For ensuring the greater accuracy, at least fifty intercept lengths are measured in different places for each sample. Then the numbers of intercept length are counted and measured the length along the line traversed. Finally, the average grain size is evaluated.

#### **4.2 Density and Porosity Calculation**

The bulk density of the sintered polished pellet shaped samples can be measured by using the Archimedes method. In this method, at first weight ( $W_d$ ) of each fully dried pellet is measured by using a precision balance. Then the pellet shaped sample is inserted into the beaker that is filled with distilled water. Then the beaker is placed in a small hanger and the saturated weight ( $W_s$ ) of the pellet is measured. By using these two weights the density of the pellet shaped specimen can be calculated as follows,

$$\rho_B = \frac{W_d}{W_d - W_S} \times \text{Density of water} \quad (4.7)$$

However, in this thesis the experimental or bulk density of the selected compositions is calculated by using the following relation,

$$\rho_{exp} = \frac{M}{\pi r^2 h} \quad (4.8)$$

Where  $r$  is the radius of the pellet shaped sample and  $h$  is the thickness of the pellet. The theoretical density of all the pellet shaped specimens is evaluated by using the following relation,

$$\rho_{th} = \frac{ZM}{N_A V} \quad (4.9)$$

Where  $Z$  denotes the number of formula unit per unit cell,  $M$  is the molecular weight,  $N_A$  is defined as the Avogadro's number ( $6.023 \times 10^{23}$  /mole), and  $V$  is the volume of the unit cell.

The porosity of all the selected compositions is evaluated by using the following expression,

$$P(\%) = \left( \frac{\rho_{th} \times \rho_B}{\rho_{th}} \right) \times 100 \quad (4.10)$$

Where  $\rho_{th}$  and  $\rho_B$  is defined as the theoretical and bulk (experimental) density, respectively.

### 4.3 Dielectric Properties Measurement

A dielectric material is typically an insulator which is polarized when subjected to an applied electric field. Basically the study of dielectric properties involves the storage and dissipation of electric and magnetic energy in materials. Typically the measurement of dielectric constant involves the measurement of capacitance  $C_o$  of a test capacitor with vacuum between its plates. Then using the same capacitor and maintaining the same distance between its plates, the

capacitance  $C$  with a dielectric material between the plates is measured. The relative permittivity can now be calculated as,

$$\epsilon_r = \frac{C}{C_0} \quad (4.11)$$

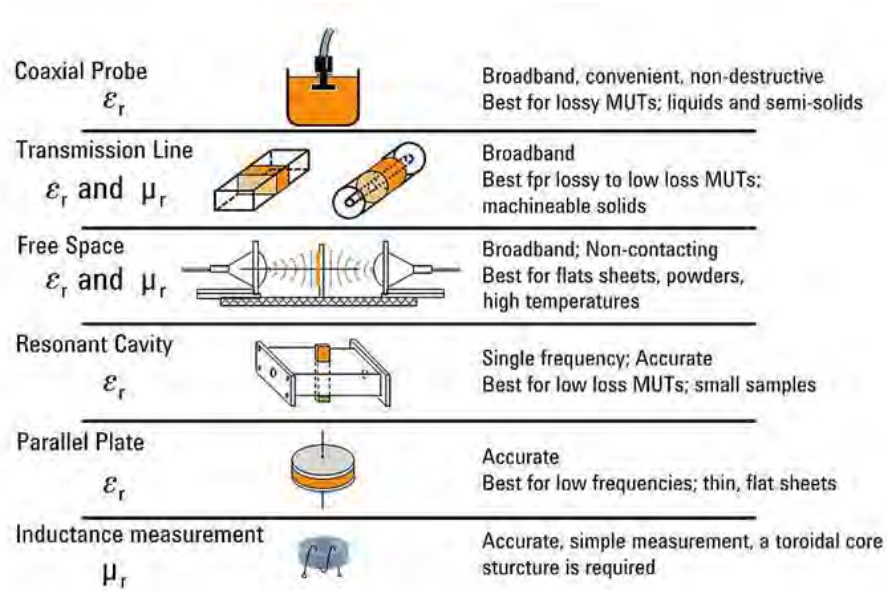


Fig. 4.6: Some techniques for the measurement of dielectric properties [11].

There are several methods available for measuring the dielectric properties of a material. The instruments that are used to employ those techniques have some common parts such as, test fixtures to hold the specimen under investigation, precise instrumental section and software that makes the whole measurement process easier and display the results. Some key instruments are the network analyzer, impedance analyzer, LCR meters etc. Some techniques for the measurement of dielectric properties are shown in Fig. 4.6.

In the present study, a precision impedance analyzer is used for investigating the dielectric properties of the selected samples. The basic function and working principle of an impedance analyzer is discussed below.

### 4.3.1 Impedance Analyzer

Impedance analyzer is the most widely used instrument in dielectric measurement on a small scale. It offers an all-in-one approach for the measurement of capacitance. The instrument is used to measure the parasitic resistance and capacitance, and the dielectric constant can be evaluated if the physical dimensions of the parallel plate capacitor are known. A typical diagram of an impedance analyzer is illustrated in Fig. 4.7.

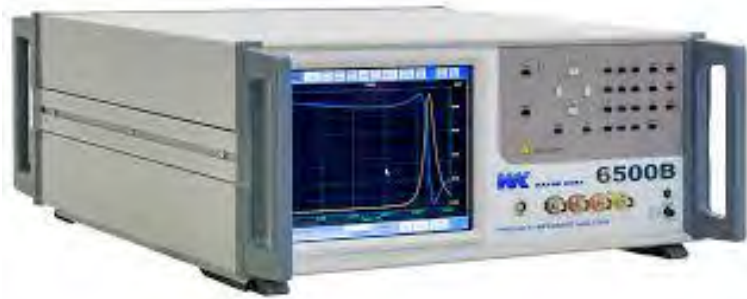


Fig. 4.7: A typical diagram of an impedance analyzer.

### 4.3.2 Theory and working principle of Impedance Analyzer

By applying a comparatively small sinusoidal signal of amplitude  $A$  and frequency  $f$  to the capacitor, the displacement current  $I$  through the capacitor and the voltage  $V$  across the capacitor can be measured by using an Impedance Analyzer and find the complex impedance  $Z$  from the Ohm's Law [12]:

$$\frac{V}{I} = Z = R - jX = Z \angle \theta^0 \quad (4.12)$$

$$X = \frac{1}{2\pi fC} \quad (4.13)$$

When the capacitance under test is small, the reactance  $X$  will be large and possibly affected by a parasitic resistance. On the other hand, if the capacitance under test is typically large then the reactance will be small and likely to be affected by a series resistance. For making the above two equations simple, the admittance  $Y$  is found instead of the impedance.

$$\frac{I}{V} = \frac{1}{Z} = Y \quad (4.14)$$

$$Y = G + jB = Y \angle \varphi^0 \quad (4.15)$$

$$|Y| = \sqrt{(G^2 + B^2)} \quad (4.16)$$

$$B = 2\pi fC \quad (4.17)$$

$$R_p = \frac{1}{G} \quad (4.18)$$

In the above equations,  $B$  is the susceptance measured in Siemens and  $G$  stands for the conductance measured also in Siemens. All of these equations are done inside the Impedance Analyzer and the capacitance  $C$  is displayed along with the parasitic parallel resistance  $R_p$ . Other useful parameters includes the quality factor  $Q$  and the dissipation or loss factor  $D$ . These two parameters provide a metric for the ratio of parasitic resistance and capacitance. The quality factor can be expressed as,

$$Q = \frac{1}{D} = \frac{|B|}{G} \quad (4.19)$$

If the capacitor is ideal then no parasitic resistance will present. As a result, the quality factor  $Q$  will be infinity. Hence, under this condition low dissipation factor and high quality factor is mostly desirable. The value of the dielectric constant  $\epsilon'$  can easily be evaluated by using the parallel plate capacitor equation when the capacitance is found.

$$\varepsilon' = \frac{Cd}{\varepsilon_0 A} \quad (4.20)$$

Where  $C$  is the capacitance of the dielectric measured in ‘ $F$ ’,  $d$  is the thickness of the pellet shaped sample measured in ‘ $m$ ’,  $\varepsilon_0$  is the dielectric permittivity of free space ( $8.854 \times 10^{-12}$  F/m) and  $A$  is the cross-sectional area of the electrode measured in ‘ $m^2$ ’.

### 4.3.3 Dielectric measurement techniques

In this thesis, the measurements of dynamic (dielectric and electrical) transport properties are performed by using a precision Impedance Analyzer (Wayne Kerr Impedance Analyzer, 6500B) as shown in Fig. 4.8. For electrical and dielectric measurement, the pellet shaped samples are first polished to remove roughness of the surface and contamination of any other oxides on the surface during the sintering process. Both sides of the samples are then painted with conducting silver paste for ensuring the good electrical contacts as illustrated in Fig. 4.9. The real part of dielectric constant of the selected samples is then calculated by using the following relation [13],

$$\varepsilon' = \frac{C}{C_0} \quad (4.21)$$

Where  $C$  is the capacitance of the sample measured by the Impedance Analyzer and  $C_0$  is the capacitance of the same capacitor without the dielectric material.  $C_0$  is derived geometrically as follows,

$$C_0 = \frac{\varepsilon_0 A}{d} \quad (4.22)$$

Where  $A (= \pi r^2)$  is the cross-sectional area of the electrode.





Fig. 4.8: Experimental setup of Wayne Kerr Impedance Analyzer (6500B).

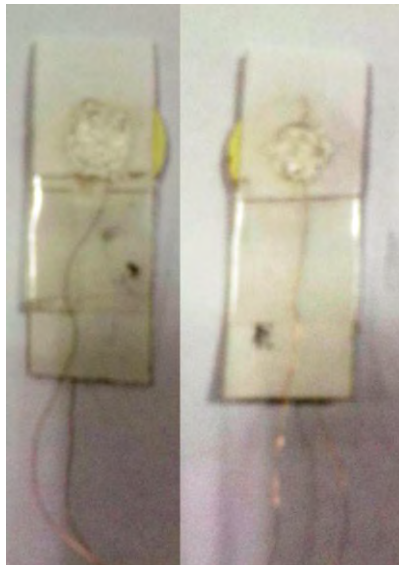


Fig. 4.9: Silver paste painted two probe arrangements on the sintered sample.

The imaginary part of dielectric constant is calculated by using the following relation,

$$\varepsilon'' = \varepsilon' \tan \delta_E \quad (4.23)$$

Where ' $\tan \delta_E$ ' is known as the loss tangent or dissipation factor  $D$ .

#### 4.3.4 Measurement of ac-conductivity

For understanding the mechanism of conduction the ac-conductivity of all the selected compositions are determined at room temperature for a wide range of frequency. The ac-conductivity can be calculated according to the following relation [14],

$$\sigma_{ac} = \frac{d}{(A \times R_{ac})} \quad (4.24)$$

Where  $R_{ac}$  is the ac resistance. The electrical conductivity of most of the materials is expressed as,

$$\sigma(\omega, T) = \sigma_{dc}(T) + \sigma_{ac}(\omega, T) \quad (4.25)$$

Where  $\sigma_{dc}$  defines the dc-conductivity which depends only upon the temperature and  $\sigma_{ac}$  is the ac-conductivity which depends both on the frequency and temperature. The frequency dependent ac-conductivity can be expressed by the empirical formula,

$$\sigma_{ac}(\omega, T) = A\omega^n \quad (4.26)$$

Where  $A$  and  $n$  both are constants which depend on temperature as well as composition. The constant  $n$  is dimensionless and  $A$  has units of  $\sigma_{ac}$ . The ac-conductivity of all the sintered samples are evaluated from the dielectric constant data by using the following expression [15],

$$\sigma_{ac} = \varepsilon' \varepsilon_0 \omega \tan \delta \quad (4.27)$$

Where  $\omega (= 2\pi f)$  defines the angular frequency.

#### 4.4 Impedance Spectroscopy

The complex impedance spectroscopy is a powerful tool to investigate the electrical properties of the complex perovskite oxides [16-17]. The main advantages of the techniques are i) it involves relatively simple electrical measurements that can readily be automated ii) the measurements can be implemented by using arbitrary electrodes, iii) the results can be often correlated with the properties such as composition, microstructure, defects, dielectric properties, chemical reaction etc. of the sample, iv) the resistance of the grain boundaries and that of grains can be easily separated in most of the polycrystalline samples.

AC measurements are often made with a Wheatstone bridge type of apparatus (Impedance analyzer or LCR meter) in which the resistance  $R$  and capacitance  $C$  of the sample are measured and balanced against variable resistors and capacitors. The impedance  $|Z|$  and the phase difference ( $\theta$ ) between the voltage and current are measured as a function of frequency for the given sample and the technique is called impedance spectroscopy. Analysis of the data is carried out by plotting the imaginary part of the impedance  $Z'' = |Z| \cos \theta$  against the real part  $Z' = |Z| \sin \theta$  on a complex plane called the impedance plot. An impedance plot with linear scale is used to analyze the equivalent circuit as follows. Impedance plot of a pure resistor is a point on real axis and that of pure capacitor is a straight line coinciding with the imaginary axis. The impedance of a parallel RC combination is expressed by the following relation:

$$Z^* = Z' - jZ'' = \frac{R}{(1 + j\omega RC)} \quad (4.28)$$

After simplification, one gets

$$(Z' - \frac{R}{2})^2 + (Z'')^2 = (\frac{R}{2})^2 \quad (4.29)$$

Which represents the equation of a circle with radius  $R/2$  and center at  $(R/2, 0)$ . Thus, a plot of  $Z'$  vs.  $Z''$  (as parametric function of  $\omega$ ) will result in a semicircle (Fig. 4.10) of radius  $R/2$ . This plot is often called a Nyquist plot. The time constant of the simple circuit is defined as

$$\tau = RC = \frac{1}{\omega_0} \quad (4.30)$$

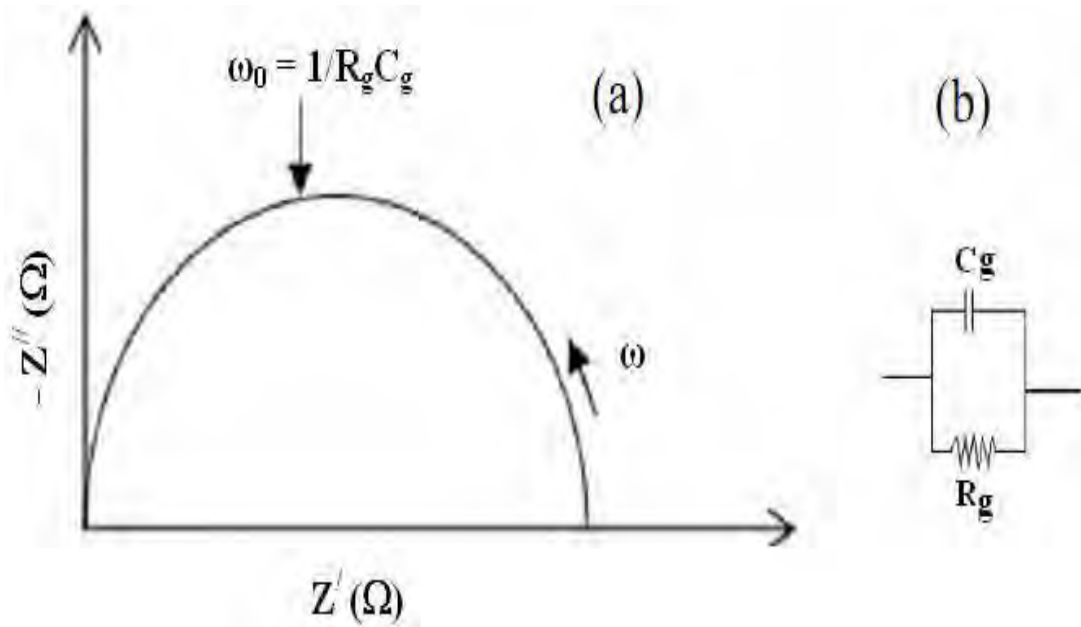


Fig. 4.10: (a) The impedance plot for a circuit of a resistor and a capacitor in parallel and (b) the corresponding equivalent circuit [17].

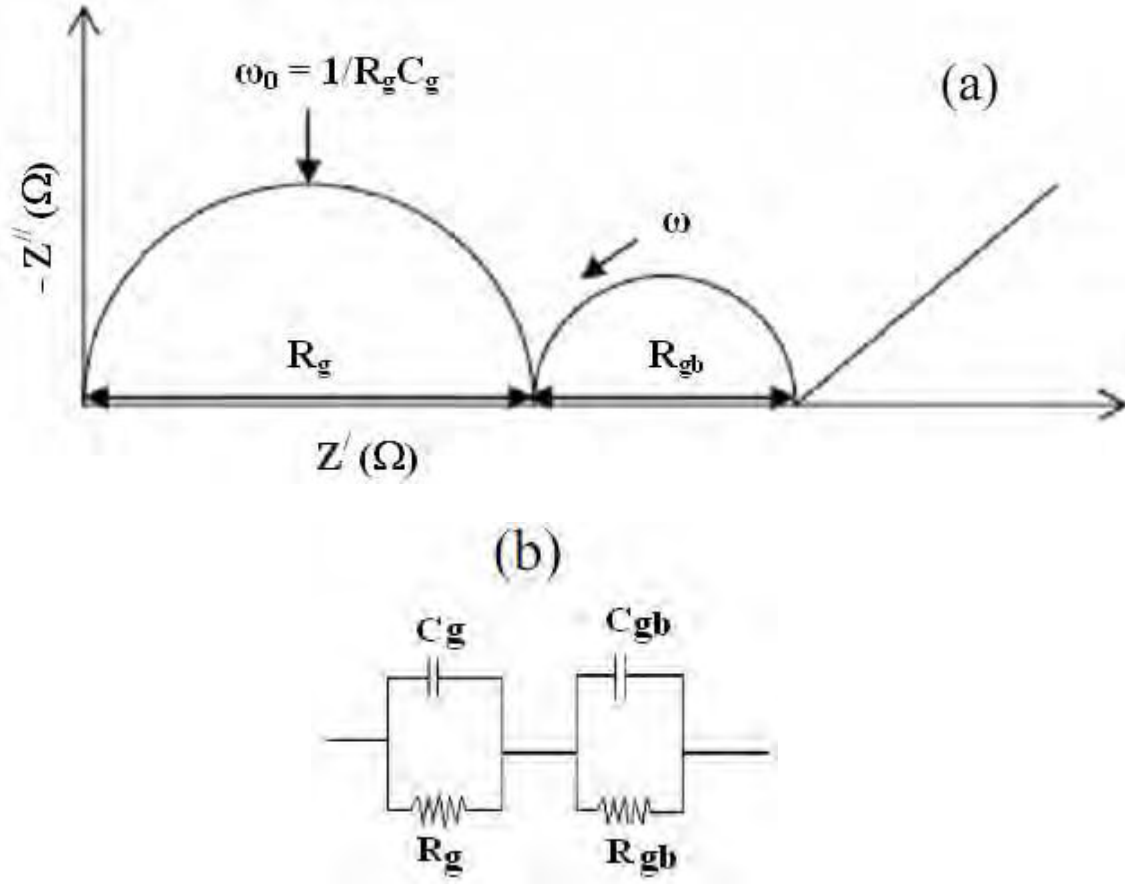


Fig. 4.11: (a) The impedance plot for an ideal polycrystalline sample and (b) the corresponding equivalent circuit [17].

This corresponds to the relaxation time of the sample and the characteristic frequency lies at the peak of the semi-circle. In an ideal polycrystalline material, the impedance plot exhibits an arc at high frequency corresponds to the bulk property of the sample, an arc at low frequency corresponds to the grain boundary behavior and a spike at the lowest frequency corresponds to the electrode effect. Fig. 4.11 (a) shows a typical impedance plot for a polycrystalline material and Fig. 4.11 (b) represented the equivalent circuit.

In this thesis, a precision Impedance Analyzer (Wayne Kerr Impedance Analyzer, 6500B) is used for the measurement of real ( $Z'$ ) and imaginary ( $Z''$ ) part of the complex impedance as a function of frequency at room temperature.

#### 4.5 Modulus Spectroscopy

The study of complex modulus spectroscopy provides crucial information about the distribution parameters of different micro regions in the polycrystalline sample such as grain, grain boundary and electrode interface. This technique is very effective in separating the contributions of different factors such as grain boundary effect, bulk effect and interfaces. It is also useful for separating the components having similar resistance but quite different capacitance. The real and imaginary part of the electric modulus are obtained from the impedance data according to the following relations [18],

$$M' = \frac{\varepsilon}{(\varepsilon'^2 + \varepsilon''^2)} = \omega C_0 Z'' \quad (4.31)$$

$$M'' = \frac{\varepsilon''}{(\varepsilon'^2 + \varepsilon''^2)} = \omega C_0 Z' \quad (4.32)$$

#### 4.6 Complex permeability measurement

Measurements of permeability basically correspond to the measurements of the change in self-inductance of a coil in presence of the magnetic core [19]. The behavior of a self-inductance can be explained as follows:

Let us consider an ideal loss less air coil of inductance  $L_0$ . On insertion of a magnetic core with permeability  $\mu$ , the inductance will be  $\mu L_0$ . The complex impedance  $Z$  of this coil [20] can be expressed as follows:

$$Z = R + jX = J\omega L_0\mu = J\omega L_0(\mu' - J\mu'') \quad (4.33)$$

Where the resistive and reactive parts are given by,

$$R = \omega L_0\mu'' \quad (4.34)$$

$$X = \omega L_0\mu' \quad (4.35)$$

Here  $\omega (= 2\pi f)$  defines the angular frequency.

The frequency dependent complex permeability of the selected compositions is investigated by using a precision impedance analyzer (Wayne Kerr Impedance Analyzer, 6500B). All the measurements are carried out at room temperature in the frequency range 20 Hz to 120 MHz. The real and imaginary parts of the complex initial permeability are determined by using the following expressions [20],

$$\mu'_i = \frac{L_s}{L_0} \quad (4.36)$$

$$\mu_i = \mu'_i \tan\delta \quad (4.37)$$

Where  $L_s$  defines the self-inductance of the sample core.  $L_0$  is the inductance of the winding coil without the sample core which is derived geometrically by using the following relation,

$$L_0 = \frac{\mu_0 N^2 S}{\pi \bar{d}} \quad (4.38)$$

Where  $N$  is the number of turns of the coil ( $N = 4$ ),  $S$  denotes the area of cross section of the toroidal shaped sample and  $\bar{d}$  is the mean diameter of the toroidal sample. The cross sectional area of the toroid shaped sample can be calculated as follows,

$$S = d \times h \quad (4.39)$$

Where

$$d = \frac{d_2 - d_1}{2} \quad (4.40)$$

Here  $d_1$  is the inner diameter of the sample core and  $d_2$  is the outer diameter of the sample core.  $h$  is the thickness of the sample core.

The mean diameter of the toroid shaped sample can be calculated as,

$$\bar{d} = \frac{d_1 + d_2}{2} \quad (4.41)$$

The relative quality factor (RQF) is evaluated by using the following relation,

$$RQF = \frac{\mu'_i}{\tan \delta} \quad (4.42)$$

Where  $\tan \delta_M$  (Quality factor;  $Q = 1/\tan \delta_M$ ) is the loss factor.

## References

- [1] "X-Ray Crystallography." Wikipedia, Wikimedia Foundation, [en.wikipedia.org/wiki/X-ray-crystallography](https://en.wikipedia.org/wiki/X-ray_crystallography), 9 Jan. 2019.
- [2] Bragg, W.H. and Bragg, W.L., "The reflection of X-rays by crystals," Proc. R. Soc. Lond. A, vol. 88 (605), pp. 428-438, 1913.



- [3] Britannica, The Editors of Encyclopaedia. “Bragg Law.” Encyclopædia Britannica, Encyclopædia Britannica, Inc., [www.britannica.com/science/Bragg-law](http://www.britannica.com/science/Bragg-law), 30 Dec. 2016.
- [4] Brundle, C.R., Evans, C.A. and Wilson, S. Encyclopedia of Materials Characterization Butterworth, 1992.
- [5] “Empyrean.” Prolab Systems, [prolabsystems.com/wp/product/empyrean/](http://prolabsystems.com/wp/product/empyrean/).
- [6] Nelson, J.B. and Riley, D.P., “An experimental investigation of extrapolation methods in the derivation of accurate unit-cell dimensions of crystals,” Proceedings of the Physical Society, vol. 57 (3), pp. 160, 1945.
- [7] “Scanning Electron Microscope.” Wikipedia, Wikimedia Foundation, [en.wikipedia.org/wiki/Scanning-electron-microscope](http://en.wikipedia.org/wiki/Scanning-electron-microscope), 8 Jan. 2019.
- [8] “SEM: Types of Electrons, Their Detection and the Information They Provide.” Blog, [blog.phenom-world.com/sem-electrons-detection-provide-information](http://blog.phenom-world.com/sem-electrons-detection-provide-information).
- [9] “Field Emission Scanning Electron Microscopy : Electron Microscopy Service.” UPV, [www.upv.es/entidades/SME/info/859071normali.html](http://www.upv.es/entidades/SME/info/859071normali.html).
- [10] Mendelson, M.I., “Average grain size in polycrystalline ceramics,” J. Am. Ceram. Soc., vol. 52 (8), pp. 443-446, 1969.
- [11] MA Business Ltd. “Six Techniques for Measuring Dielectric Properties”, New Electronics, [www.newelectronics.co.uk/electronics-technology/six-techniques-for-measuringdielectric-properties/152591/](http://www.newelectronics.co.uk/electronics-technology/six-techniques-for-measuringdielectric-properties/152591/), 9 Mar. 2017.
- [12] Shah, M. R., “Dielectric properties of alkaline earth (D = Ba, Sr, Ca) and rare earth (T = La, Nd) substituted polycrystalline  $D_{1-x}T_x(Ti_{0.5}Fe_{0.5})O_3$  perovskite”, Ph. D. Thesis, Department of Physics, Bangladesh University of Engineering and Technology, 2013.

- [13] Goldman, A., "Handbook of modern ferromagnetic materials", Springer Science & Business Media, Vol. 505, 2012.
- [14] Hossen, M. B., "Study of physical, magnetic and transport properties of cations substituted NiCuZn based spinel ferrites", Ph. D. Thesis, Department of Physics, Bangladesh University of Engineering and Technology, 2015.
- [15] Momin, A.A., Parvin, R. and Hossain, A.A., "Structural, morphological and magnetic properties variation of nickel-manganese ferrites with lithium substitution", J. Magn. Mater., vol. 423, pp. 124-132, 2017.
- [16] Barsoukov, E. and Macdonald, J. R., "Impedance Spectroscopy Theory, Experiments and Applications", 2nd edition (Hoboken, NJ: Wiley) 34-46, 2005.
- [17] Macdonald, J. R., "Impedance Spectroscopy", Wiley, New York, 1987.
- [18] Rahman, M.A. and Hossain, A.A., "Relaxation mechanism of (x)  $Mn_{0.45}Ni_{0.05}Zn_{0.50}Fe_2O_4 + (1-x) BaZr_{0.52}Ti_{0.48}O_3$  multiferroic materials", Phys. Scr., vol. 89 (11), pp. 115811, 2014.
- [19] Rafique, M., "Study of the Magnetoelectric Properties of Multiferroic Thin Films and Composites for Device Applications", Ph. D. Thesis, Department of Physics, COMSATS Institute of Information Technology, 2014.
- [20] Goldman, A., "Handbook of modern ferromagnetic materials", Kulwer Acad. Pub, Boston, U.S.A, 1999.

## CHAPTER 5

## RESULTS AND DISCUSSION

## 5.1 Structural Analysis

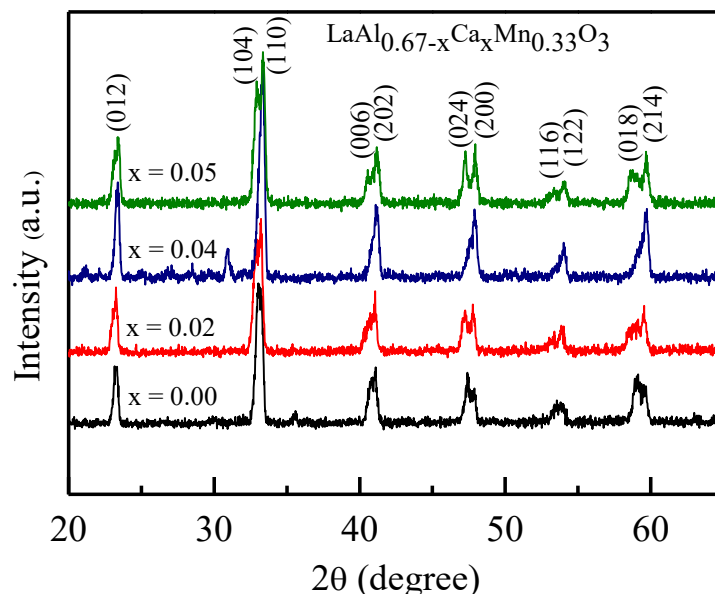


Fig. 5.1: XRD pattern of  $\text{LaAl}_{0.67-x}\text{Ca}_x\text{Mn}_{0.33}\text{O}_3$  ceramics sintered at 1723 K.

The XRD patterns of various  $\text{LaAl}_{0.67-x}\text{Ca}_x\text{Mn}_{0.33}\text{O}_3$  ( $x = 0.00, 0.02, 0.04, 0.05$ ) sintered at 1723 K are shown in Fig. 5.1. The XRD patterns indicate that all specimens are single phase perovskite structure and no second phase peaks are detected. This implies that Ca and Mn atoms have entered into crystalline lattice structure to form a homogeneous solid solution. The XRD patterns are in good agreement with a rhombohedrally distorted perovskite structure which is equivalent to hexagonal symmetry [1]. As shown in Fig. 5.1, the splitting of the peak is observed for different values of doping content. The splitting peak is the characteristic of rhombohedral structure and Peaks are indexed with JCPDS card number 031-0022 [2]. It is also observed that the diffraction peaks for all the compositions are shifted to the lower angles with the increase of Ca content. This may be due to the replacement of smaller  $\text{Al}^{3+}$  (0.535 Å) by the

larger  $\text{Ca}^{2+}$  (1.00 Å) which causes the increasing of interplaner spacing between the lattices [3]. The variation trend of the crystal lattice is related to the variation of dopant ion's radius. Since the radii of  $\text{Mn}^{4+}$  (six coordination, 0.53 Å) and  $\text{Ca}^{2+}$  (six coordination, 1.00 Å) are closer to that of  $\text{Al}^{3+}$  (six coordination, 0.535 Å), the dopants would substitute B sites of the  $\text{LaAlO}_3$  lattice. Since the radius of  $\text{Ca}^{2+}$  is larger than that of  $\text{Al}^{3+}$ , the substitution of  $\text{Al}^{3+}$  by  $\text{Ca}^{2+}$  leads to the expansion of the lattice. The lattice parameters 'a' and 'c' are calculated following the formula of hexagonal equivalent for rhombohedrally distorted structure [4]. The lattice parameters are found to be  $a = b = 5.3280$  to  $5.3923$  Å and  $c = 13.2624$  to  $13.8768$  Å.

## 5.2 Density and Porosity

Density plays an important role in controlling the microstructural and the dielectric properties of the polycrystalline materials. Fig. 5.2 show the variation of density and porosity of various  $\text{LaAl}_{0.67-x}\text{Ca}_x\text{Mn}_{0.33}\text{O}_3$  ceramics sintered at 1723 K as a function of Ca content. It is seen that both theoretical density,  $\rho_x$ , and bulk density,  $\rho_B$ , decrease with the addition of Ca. The decrease in density with the increase of Ca content is attributed to the fact that the molecular weight. The substitution of Al by Ca leads to a variation in bonding among the elements and makes a change in interatomic distance which in turn makes a contribution to expand the unit cell volume and decrease the density. It also appears that the value of  $\rho_B$  for all the compositions is lower than that of the corresponding  $\rho_x$ . This may be due to the presence of pores in the bulk samples which may be formed and developed during sintering.

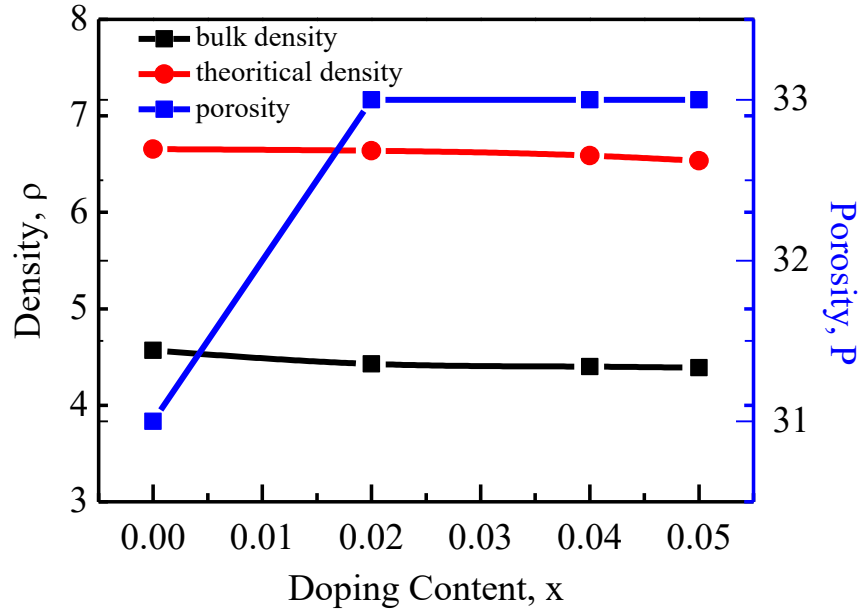


Fig. 5.2: variation of density and porosity with Ca content of various  $\text{LaAl}_{0.67-x}\text{Ca}_x\text{Mn}_{0.33}\text{O}_3$  ceramics.

Table 5.1: Data of Theoretical density, Bulk density and Porosity of various  $\text{LaAl}_{0.67-x}\text{Ca}_x\text{Mn}_{0.33}\text{O}_3$  ceramics.

| Doping content, x | Theoretical density, $\rho_{th}$ (g/cm <sup>3</sup> ) | Bulk density, $\rho_B$ (g/cm <sup>3</sup> ) | Porosity, P (%) |
|-------------------|---|---|-----------------|
| 0.00              | 6.655   | 4.57  | 31              |
| 0.02              | 6.638   | 4.43  | 33              |
| 0.04              | 6.588   | 4.40  | 33              |
| 0.05              | 6.534   | 4.39  | 33              |

Generally, grain boundaries are grown over the pores by the force generated through the thermal energy during the sintering process. As a result, pore volume is decreased and the samples become more dense with the increase in  $T_s$ . Porosity in ceramic sample is generated basically from two sources, intergranular porosity and intragranular porosity [5]. The intergranular porosity depends upon the average grain size. However, some pores are trapped within the ceramic sample due to the very high driving energy at higher sintering temperature.

### 5.3 Morphological Analysis

The microstructure of ceramics strongly influences their electrical and magnetic properties, so it is necessary to determine the average grain size  $D$  and the type of grain growth of the samples. The FESEM micrographs of various  $\text{LaAl}_{0.67-x}\text{Ca}_x\text{Mn}_{0.33}\text{O}_3$  ceramics sintered at 1723 K with different magnifications are shown in Fig. 5.3, 5.4 and 5.5. All the samples show a dense microstructure.

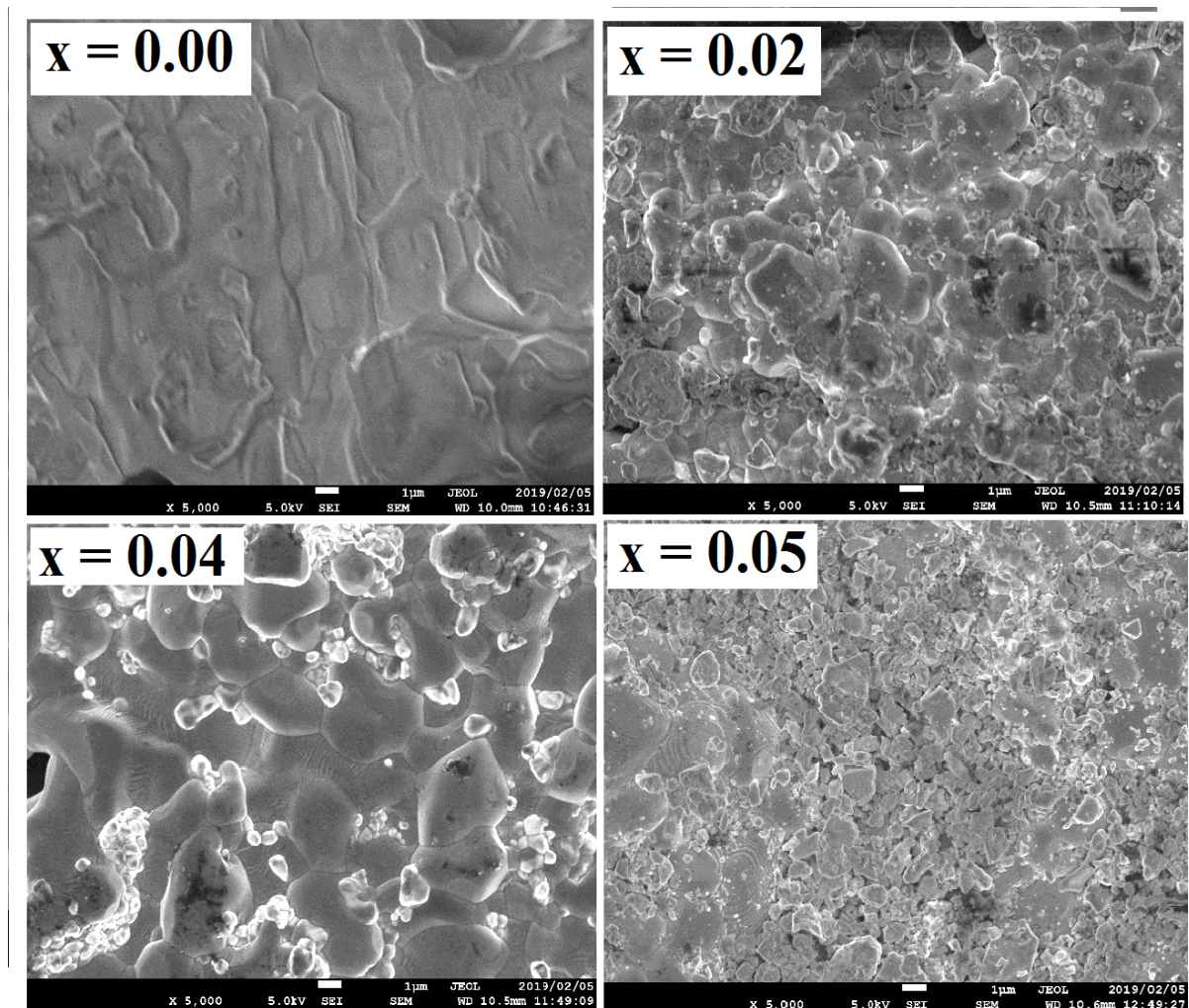


Fig. 5.3: FESEM micrographs (magnification 5,000 times) of various  $\text{LaAl}_{0.67-x}\text{Ca}_x\text{Mn}_{0.33}\text{O}_3$  ceramics sintered at 1723 K.

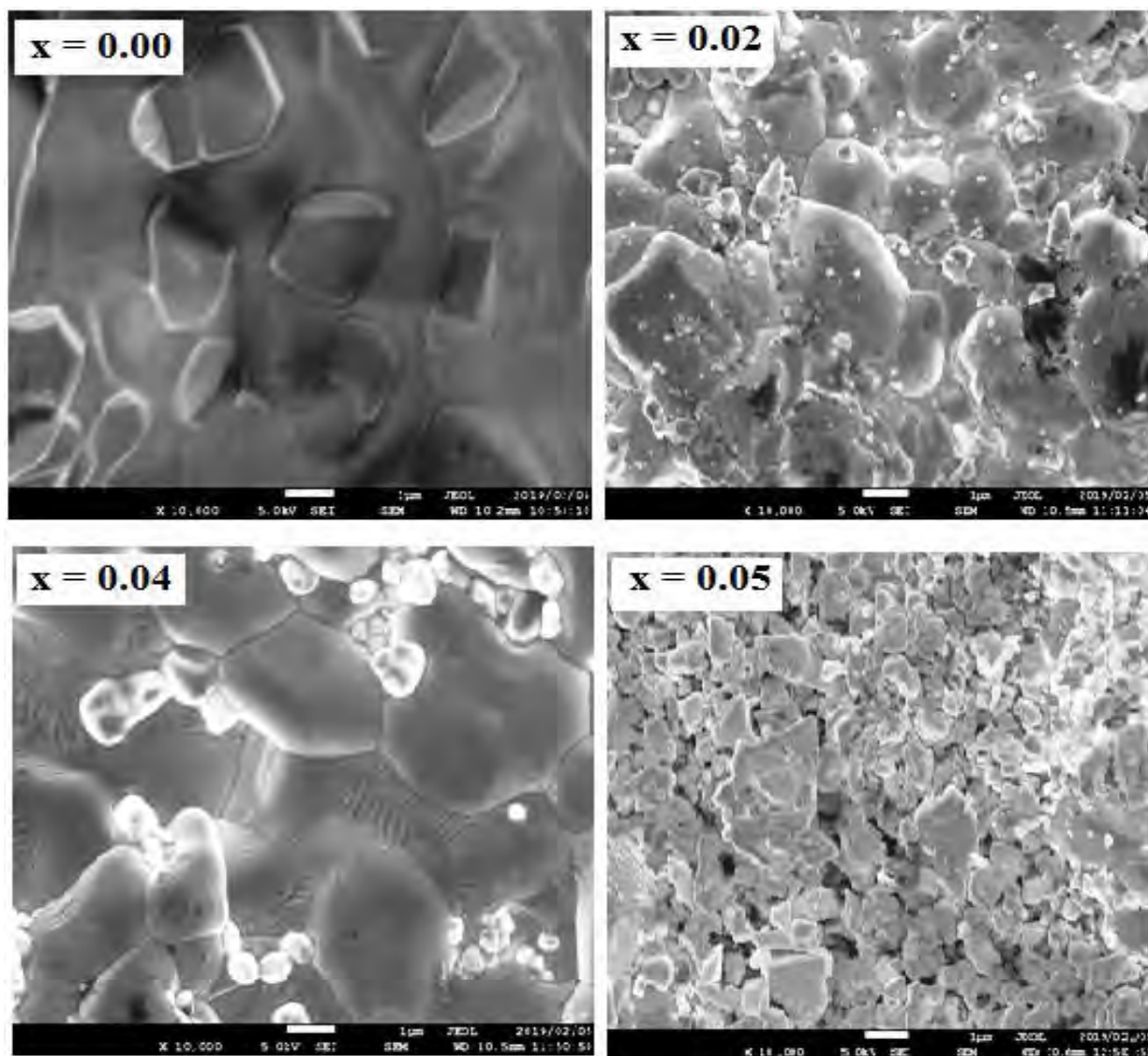


Fig. 5.4: FESEM micrographs (magnification 10,000 times) of various  $\text{LaAl}_{0.67-x}\text{Ca}_x\text{Mn}_{0.33}\text{O}_3$  ceramics sintered at 1723 K.



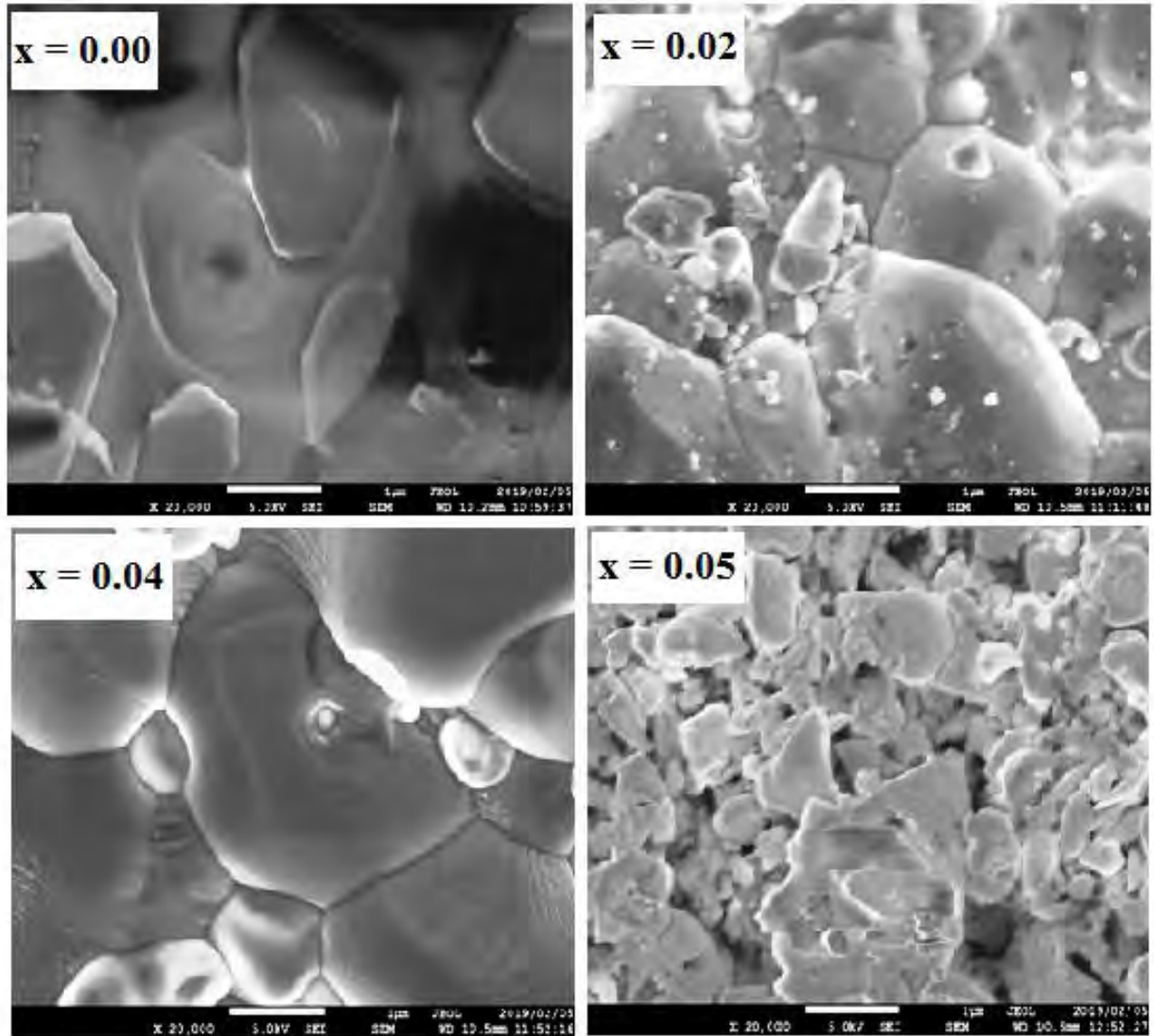


Fig. 5.5: FESEM micrographs (magnification 20,000 times) of various  $\text{LaAl}_{0.67-x}\text{Ca}_x\text{Mn}_{0.33}\text{O}_3$  ceramics sintered at 1723 K.

For the sample with  $x=0.00$ , [see Fig. 5.3, 5.4, 5.5], the liquid phase seemed to appear in the grain boundary region during sintering but no second phase was found from XRD. This kind of liquid phase sintering of the  $\text{LaAl}_{0.67-x}\text{Ca}_x\text{Mn}_{0.33}\text{O}_3$  ( $x=0.00$ ) ceramic may be due to the low melting point of Al [6]. The Ca doping leads to a large change in the microstructure of the ceramics. The  $\text{LaAl}_{0.67-x}\text{Ca}_x\text{Mn}_{0.33}\text{O}_3$  ceramics containing Ca showed a clean grain boundary.



The value of  $D$  of different compositions was obtained by using the linear intercept method. For Ca doping ( $x = 0.02, 0.04$ ) the observed  $D$  values are  $1.60 \mu\text{m}$  and  $2.24 \mu\text{m}$ , respectively. The increase of average grain size which could be attributed to  $\text{Ca}^{2+}$  have higher ionic radius than  $\text{Al}^{3+}$ . For  $x = 0.05$  the average grain size ( $1.32 \mu\text{m}$ ) decreases because in this case significant amount of  $\text{Ca}^{2+}$  reside at the grain boundaries which hamper the grain growth and may be increased in strain on the grains [7], consequently, leads to decrease of  $D$ . On the other hand, Ca and Mn co-doping may also avoid the formation of a liquid phase during the sintering process, which leads to a perfect grain boundary.

## 5.4 Dielectric Properties

### 5.4.1 Dielectric constant

Frequency dependent real part of dielectric constant ( $\epsilon'$ ) of  $\text{LaAl}_{0.67-x}\text{Ca}_x\text{Mn}_{0.33}\text{O}_3$  ceramics sintered at 1723 K which shown in Fig. 5.6. It is evident that at lower frequency all the compositions exhibit higher values of dielectric constant. The permittivity is gradually decreased with the increase in frequency and becomes zero at very high frequency. Such frequency dependent dielectric behavior can be explained by Koops theory dependent on the Maxwell-Wagner model for inhomogeneous crystal structure [8-10]. This model proposed that a typical dielectric medium is composed of well conducting grains that are generally separated by resistive (poorly conducting) grain boundaries. When an external electric field is applied on a dielectric medium the charge carriers begin to migrate through the conducting grain and are piled up at the resistive grain boundaries. As a result, large polarization takes place within the dielectric medium resulting colossal permittivity. In this case the poorly conducting grain

boundaries contribute to the higher value of permittivity at lower frequency.  $\text{LaAl}_{0.67-x}\text{Ca}_x\text{Mn}_{0.33}\text{O}_3$  ceramics shows colossal permittivity up to frequency  $10^6$  Hz.

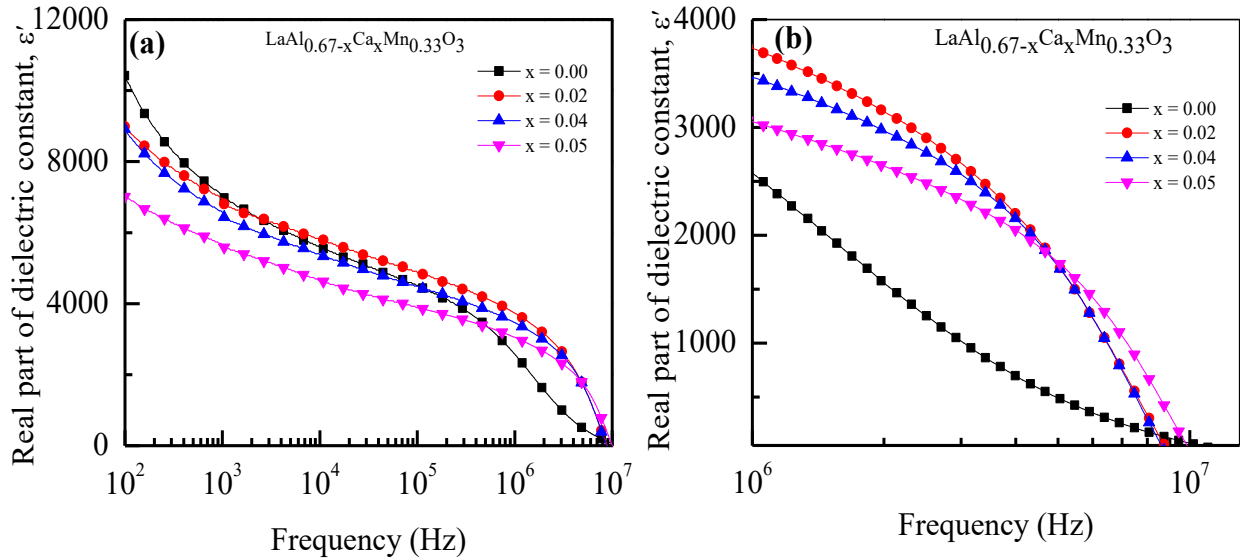


Fig 5.6: Variation of dielectric constant as a function of frequency (a)  $10^2$ - $10^7$  Hz (b)  $10^6$ - $10^7$  Hz of  $\text{LaAl}_{0.67-x}\text{Ca}_x\text{Mn}_{0.33}\text{O}_3$  ceramics sintered at 1723 K.

Different types of polarization mechanism are also responsible for the higher values of permittivity at low frequency region. In the low frequency region all of the four polarization mechanisms (space-charge, dipolar, ionic and electronic polarization) contribute to the total polarization in the compound resulting high dielectric constant. But with the increase in frequency (i.e., at high frequency region) the contribution of some of the above-mentioned polarization mechanism to the total polarization is terminated resulting lower values of permittivity. However, the polarization is affected by some other factors such as structural homogeneity, stoichiometry, grain size, density and porosity of the samples. In the present study, it is observed that the values of  $\epsilon'$  decrease with the increase of Ca content as shown in

Fig.5.6. The decrease of  $\varepsilon'$  with Ca content may be explained on the basis of cation or oxygen vacancies present in the materials. The substitution  $\text{Al}^{3+}$  by  $\text{Ca}^{2+}$  at the lattice site B of  $\text{ABO}_3$  perovskite structure, there is a strong possibility of creation of cation or oxygen vacancies. These vacancies are created in order to maintain localized charge neutrality because of different valence states of the cations that are occupying the lattice sites A and B in the perovskite structure [11-12].

#### 5.4.2 Dielectric loss factor

The variation of  $\tan\delta_E$  with frequency of various  $\text{LaAl}_{0.67-x}\text{Ca}_x\text{Mn}_{0.33}\text{O}_3$  sintered at 1723 K is shown in Fig. 5.7. From the figure it is seen that  $\tan\delta_E$  sharply decreases as frequency increases in the low frequency region (less than  $10^4$  Hz, varies with compositions), while in the high frequency region (greater than  $10^6$  Hz, varies with compositions),  $\tan\delta_E$  also increases with the increase in frequency. However, in the intermediate frequencies, the values of  $\tan\delta_E$  are minimum which indicates that the compositions are of good quality material in this range. The higher values of  $\tan\delta_E$  at very lower frequencies can be explained on the basis that the low conductivity of grain boundaries is more effective in these frequencies. Therefore, more energy is required for the exchange of electron between  $\text{Mn}^{4+} \leftrightarrow \text{Mn}^{2+}$  ions; as a result, the loss is high. Again, the  $\tan\delta_E$  is found to increase with the increase in frequency after  $10^6$  Hz (varies with compositions).

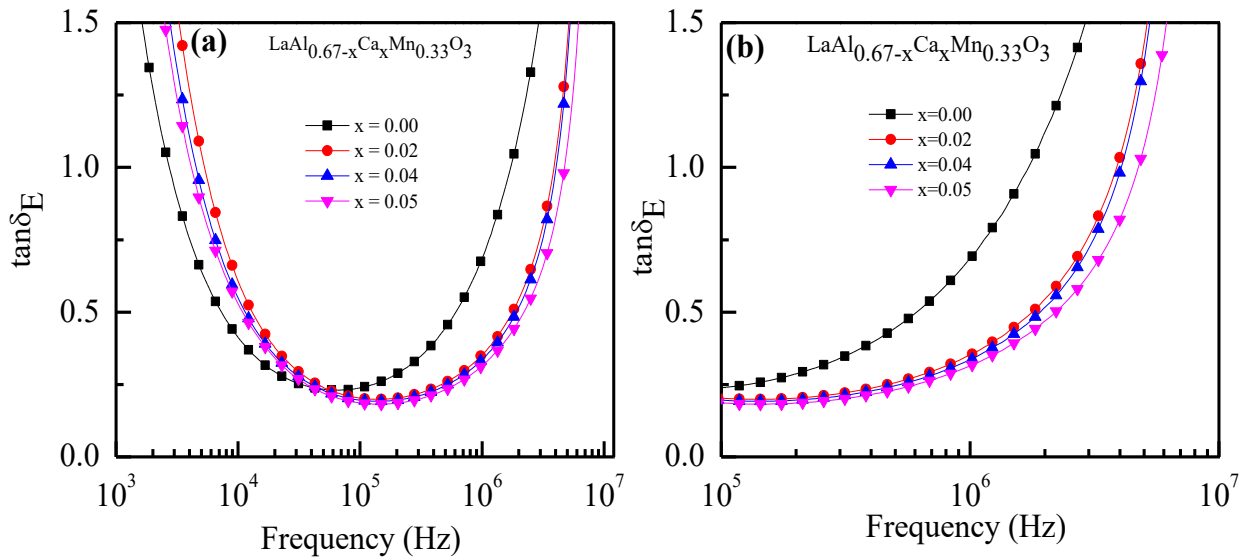


Fig.5.7: Frequency dependence of dielectric loss tangent ( $\tan \delta$ ) (a)  $10^3$ - $10^7$  Hz (b)  $10^5$ - $10^7$  Hz of  $\text{LaAl}_{0.67-x}\text{Ca}_x\text{Mn}_{0.33}\text{O}_3$  ceramics sintered at 1723 K.

This behavior may be explained on the ground that the dipoles which are formed due to impurities or inhomogeneous structure are able to follow the frequency of the applied electric field at lower frequency; therefore, small energy is required by the dipole to orient itself for polarization resulting in low loss of energy. However, with the increase in frequency, the dipoles lag behind the frequency of the applied electric field. Therefore, more energy is required for orientation of dipoles; as a result the loss is high at higher frequencies.

### 5.4.3 Complex impedance spectra analysis

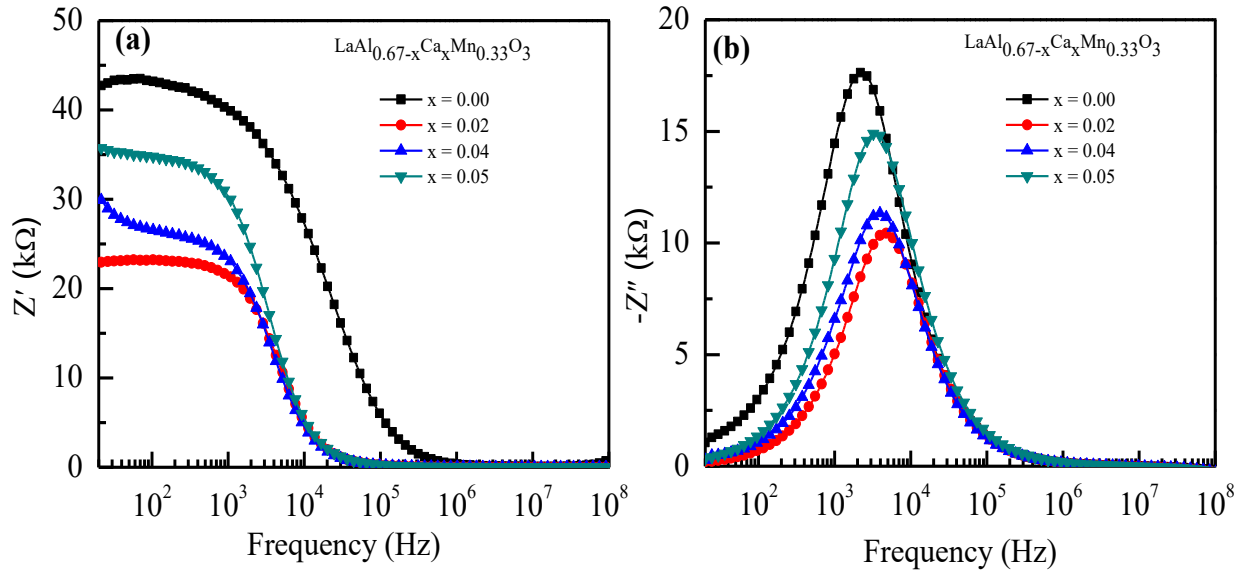


Fig 5.8: Variation of (a)  $Z'$  and (b)  $Z''$ , as a function of frequency of  $\text{LaAl}_{0.67-x}\text{Ca}_x\text{Mn}_{0.33}\text{O}_3$  ceramics sintered at 1723 K.

Complex impedance spectroscopy is a powerful tool to characterize many of the electrical properties of materials. It may be used to explore the dynamics of mobile or bound charges in the bulk or interfacial regions. The impedance behavior is described by the classical model known as Debye model. Fig 5.8 (a) show the variation of  $Z'$  with frequency of  $\text{LaAl}_{0.67-x}\text{Ca}_x\text{Mn}_{0.33}\text{O}_3$  ceramics. It is observed that the value of  $Z'$  gradually decreases with increasing frequency up to a certain limiting frequency ( $\approx 10^4$  Hz). The decrease in  $Z'$  indicates that the conduction is increasing with frequency and above this frequency ( $\approx 10^4$  Hz) it becomes almost frequency independent. The higher values of  $Z'$  at lower frequencies means the polarization in the relaxors is larger because at lower frequency all kinds of polarization is present. It is also observed that the value of  $Z'$  for all compositions coincide at higher frequencies. The merger of

$Z'$  at higher frequencies indicates possible release of space charge polarization [18-19]. On the other hand, with increasing Ca concentration, the values of  $Z'$  decrease in the low frequency ranges (up to a certain frequency  $\approx 10^4$  Hz) and then they appear to merge in the high frequency region. This indicates that the frequency at which the space charge becomes free also depends upon the Ca concentration.

Fig. 5.8 (b) shows the variation of  $Z''$  with frequency of various compositions. The variation of  $Z''$  with frequency exhibits a peak at all compositions. At higher frequency, it also decreases with increasing frequency due to the reduction of loss in the resistive part of the sample. This plot is useful for the determination of relaxation frequency ( $f_r$ ). Relaxation occurs in resistive materials due to the presence of immobile charges in  $\text{LaAl}_{0.67-x}\text{Ca}_x\text{Mn}_{0.33}\text{O}_3$  ceramics. As shown in Fig. 5.8 (b), the relaxation peak is found shifting towards higher frequency with the increase of Ca content.

The complex modulus spectroscopy is a very convenient tool to determine, analyze and interpret the electric transport properties in the materials having the smallest capacitance. The modulus spectra are particularly useful for separating spectral components of the materials having similar resistance but different capacitance. The complex electric modulus is represented by the following expression:

$$\begin{aligned} M^*(\omega) &= J(\omega C_o)Z^* \\ &= M' + jM'' \end{aligned}$$

where,  $M' = \omega C_o Z''$  and  $M'' = \omega C_o Z'$ , where the symbols have their usual meanings.

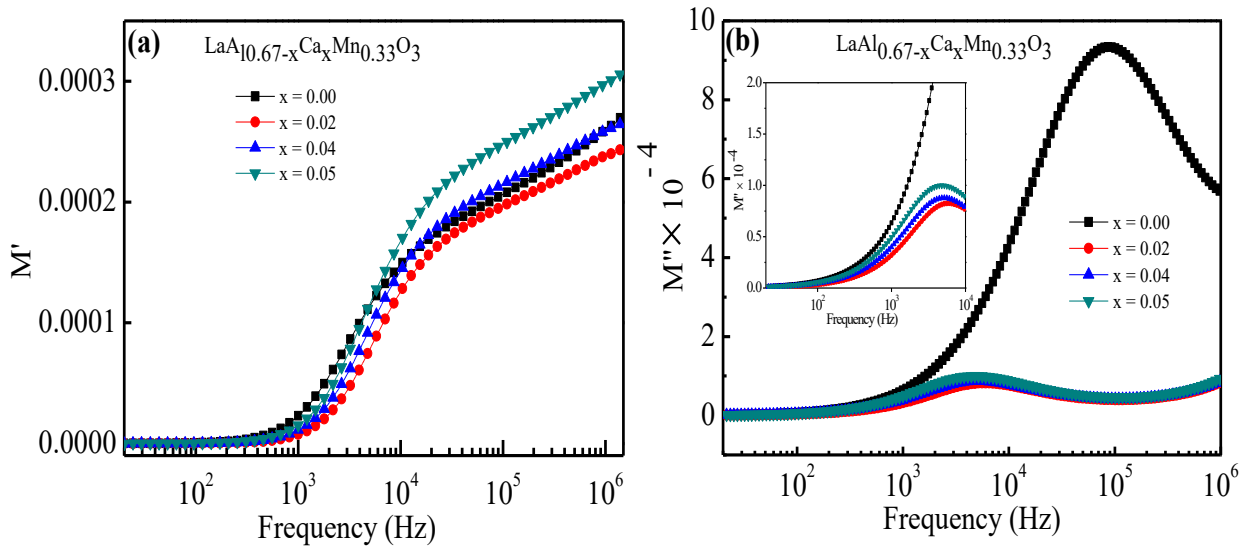


Fig. 5.9: Variation of (a)  $M'$  and (b)  $M''$ , as a function of frequency of  $\text{LaAl}_{0.67-x}\text{Ca}_x\text{Mn}_{0.33}\text{O}_3$  ceramics sintered at 1723 K.

Fig. 5.9(a) shows the variation of real part of modulus ( $M'$ ) with frequency of various compositions. The value of  $M'$  is found to be very low (nearly zero) at low frequencies and it increases with the increase in frequency. The magnitude of  $M'$  is very small in the low-frequency region revealing the ease of polaron hopping and negligibly small contribution of electrode effect [20-21]. After a certain frequency ( $10^3$  Hz) the value of  $M'$  increases rapidly with frequency for all the samples which is attributed to the inability of some of the dipoles to follow the alternating electric field at higher frequency. This continuous dispersion on increasing frequency may be contributed to the conduction phenomena due to short range mobility of charge carriers. It is possibly related to the lack of restoring force leading the mobility of the charge carriers under the action of an induced electric field [22].

The variation of imaginary part of electric modulus ( $M''$ ) with frequency is shown in Fig. 5.9(b). It exhibits a peak at the frequency above  $10^3$  Hz. These peaks indicate the transition from long-range to short range mobility of charge carriers with the increase in frequency. The frequency region below the peak maximum determines the range in which charge carriers are mobile over long distance whereas the region above peak maxima establishes the charge carriers are confined to potential well.

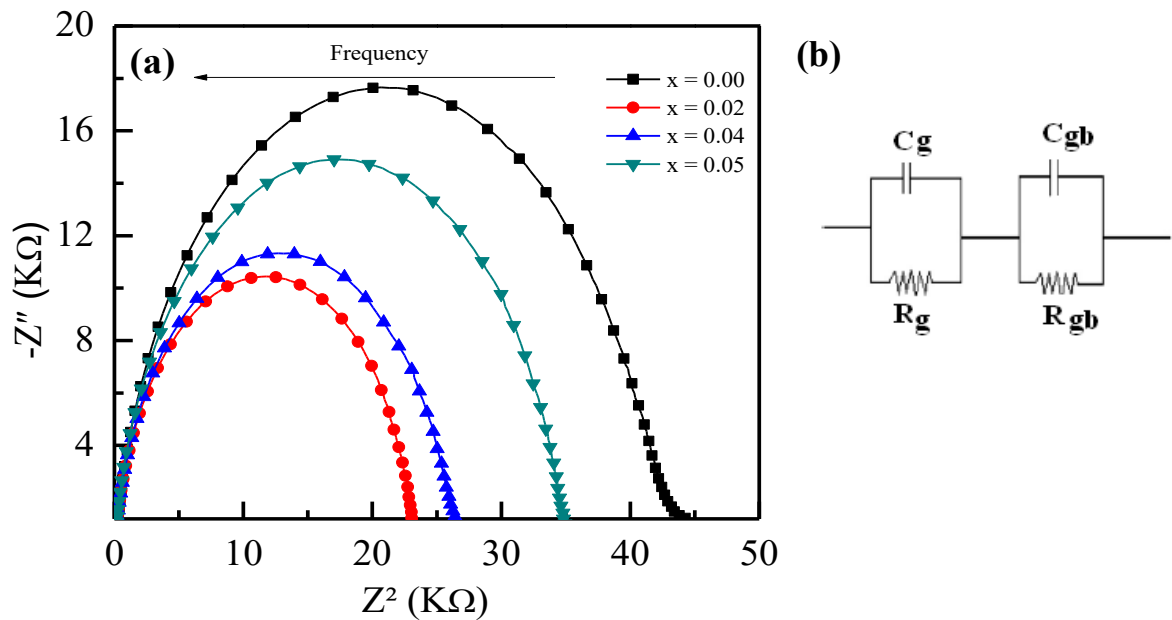


Fig. 5.10: (a) cole-cole plot ( $Z''$  vs  $Z'$ ) of various  $\text{LaAl}_{0.67-x}\text{Ca}_x\text{Mn}_{0.33}\text{O}_3$  ceramics sintered at 1723 K. (b) Equivalent circuit model.

The dielectric properties of polycrystalline materials would arise due to contributions from intra-grain, inter-grain and electrode processes [23]. The intra-grain and inter-grain processes depend upon the constituents and the processing parameters. Therefore, to understand the effect of additives and the processing parameters, the intra-grain (i.e. grain,  $g$ ), inter-grain (i.e. grain-boundary,  $g_b$ ) and electrode contributions have to be separated. The method of complex



impedance analysis has emerged as a very powerful tool for this. In this method, the imaginary part,  $Z''$ , of the experimentally measured impedance:  $Z^* = Z' - jZ''$  of the material, is plotted as a function of real part,  $Z'$ , over a range of frequencies. If the contributions from all the three sources mentioned above (intra-grain, inter-grain and electrode) have single but different of relaxation time, then three semi-circular arcs with their centers on the  $Z'$  axes are obtained. The arc with highest frequency range passing through the origin represents the grains effect; the one with the intermediate frequency range gives the contributions from grain boundaries while the arc with lowest frequency range represents the contributions from the electrodes interface. Electrodes interface are highly capacitive in nature and generally occurs only at very lower frequencies. The results of these contributions are obtained from the intercepts of the arcs on  $Z'$  axes.

Fig. 5.10(b) shows the equivalent circuit consists of three parallel RC circuits ( $R_g$  &  $C_g$  and  $R_{gb}$  &  $C_{gb}$ ) connected in series. These RC elements correspond to grains and grain boundaries interface in order of decreasing frequency. Each RC element of the equivalent circuit gives rise to a semicircle. From Fig. 5.10(a), All compositions exhibit a single semicircular arc starting from the origin. The absence of second semicircle in the complex impedance plots indicates that the materials have only grain boundary effect to the conductivity mechanism. It is also realized that patterns of the semicircular arc are changing with composition which implies a modification of the resistance/reactance ratio with the changing of Ca content.

### 5.4.4 AC conductivity

Fig. 5.11 shows the variation of  $\sigma_{ac}$  with frequency. The value of  $\sigma_{ac}$  at lower frequency is found almost constant whereas after a certain frequency ( $>10^4$  Hz)  $\sigma_{ac}$  increases very fast. The variation of  $\sigma_{ac}$  with frequency follows the Jonscher's power law [13]. In low frequency region, which corresponds to  $\sigma_{dc}$ , the conductivity is almost independent of frequency because at lower frequencies the resistive grain boundaries are more active according to the Maxwell-Wagner double layer model [14, 15] for dielectrics. On the other hand, in the high frequency region, this is known as hopping region,  $\sigma_{ac}$  increases faster than that of  $\sigma_{dc}$  because at higher frequencies the conductive grains become more active thereby increases hopping of charge carriers and contribute to rise in conductivity.

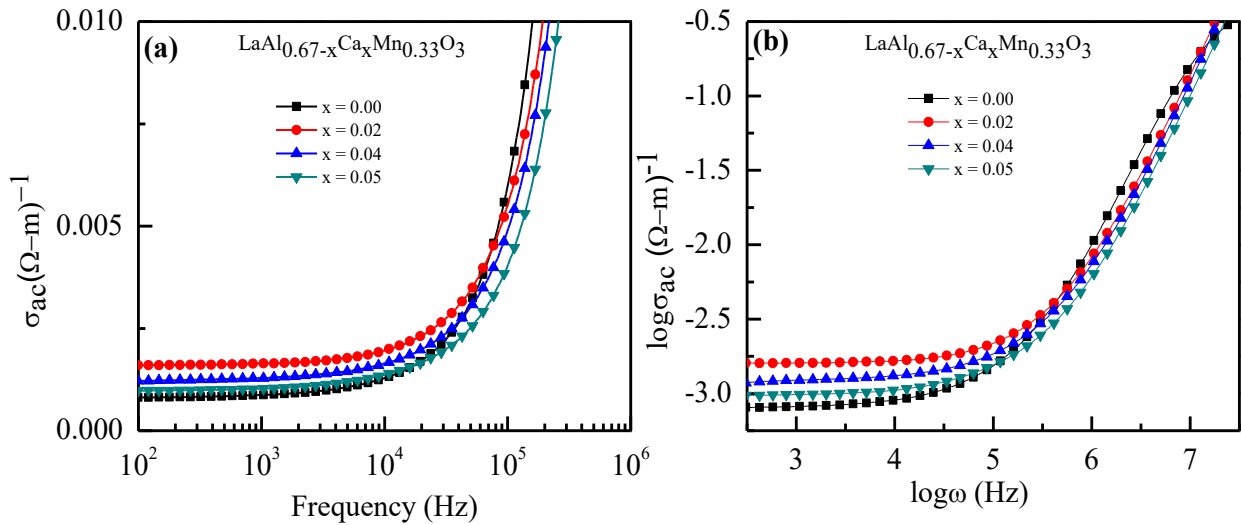


Fig. 5.11: (a) Variation of  $\sigma_{ac}$  with frequency, (b) plots of  $\log\sigma_{ac}$  versus  $\log\omega$  of  $\text{LaAl}_{0.67-x}\text{Ca}_x\text{Mn}_{0.33}\text{O}_3$  ceramics.

Thus, in the low frequency region, where the conductivity is almost constant, the transport phenomenon takes place through penetrating process. While, in the high frequency region, where the conductivity increases strongly with frequency, the transport phenomena continue by hopping carriers that arise from the substituted elements. Variation of  $\sigma_{ac}$  as a function of frequency also can be explained on the basis of polaron hopping mechanism as discussed by Austin and Mott [16]. In large polaron model,  $\sigma_{ac}$  decreases with the increase of frequency while in small polaron hopping mechanism, the  $\sigma_{ac}$  increases with the increase of frequency [17].

### 5.5 Complex initial permeability

Fig. 5.12 (a) and (b) shows the variation of  $\mu'_i$  and  $\tan\delta_M$  with frequency of various  $\text{LaAl}_{0.67-x}\text{Ca}_x\text{Mn}_{0.33}\text{O}_3$  ceramics within the range of frequency of 10 kHz – 100 MHz at room temperature respectively. As shown in Fig. 5.12 (a), the value of  $\mu'_i$  for all the compositions remains almost constant up to certain frequency and then decreases with increasing frequency.  $\mu'_i$  decreases with frequency which is due to the fact that at higher frequencies, pinning points are found to be originated at the surface of the samples from the impurities of grains and intragranular pores. The pinning points exist both at lower as well as higher frequency. At higher frequency, the motion of domain wall is obstructed more by the pinning points because of rapidly changing magnetic field. This phenomenon in turn obstructs the motion of spin and domain walls and the contribution of their motion towards the increment of permeability decreases and thereby the permeability decreases. On the other hand, the arrangement of the magnetic moment can follow the variation of external magnetic field for a longer time during the process of magnetization and thus the value of  $\mu'_i$  may shows stable value for a certain period of time [24]. Stable value of  $\mu'_i$  with frequency is important and it has potential

applications in several electrical devices such as broad band transformer and wide band read-write head for video recording etc [25, 26].

It is also seen from the figure that the value of  $\mu'_i$  is decreases for ( $x = 0.02, 0.05$ ) and for ( $x = 0.04$ ) increases and finally decreases. It is difficult to explain compositional dependence of  $\mu'_i$  for the case of polycrystalline materials because  $\mu'_i$  is sensitive to many factors. The value of  $\mu'_i$  depends on stoichiometry, composition, average grain size, impurity, coercivity, density and porosity etc. The permeability of polycrystalline materials is related to two different magnetizing mechanisms: spin rotation and domain wall motion [27-29], which can be described as follows:  $\mu_i = 1 + \chi_w + \chi_{spin}$  where  $\chi_w$  is the domain wall susceptibility;  $\chi_{spin}$  is intrinsic rotational susceptibility.  $\chi_w$  and  $\chi_{spin}$  may be written as :  $\chi_w = \frac{3\pi M_s^2 D}{4\gamma}$  and  $\chi_{spin} = \frac{2\pi M_s^2}{K}$  with  $M_s$  saturation magnetization,  $K$  the total anisotropy,  $D$  the average grain diameter, and  $\gamma$  the domain wall energy. Therefore in the present case, variation of the initial permeability is strongly influenced by its grain size and  $P$ .

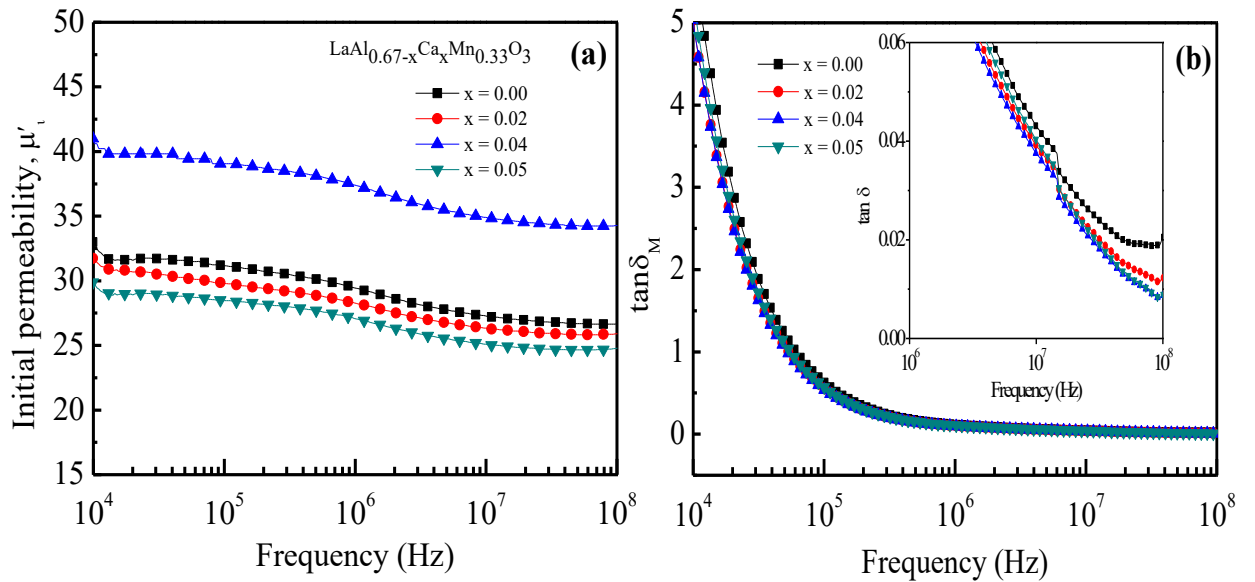


Fig. 5.12: variation of (a)  $\mu'_i$  (b)  $\tan \delta_M$  with frequency of various  $\text{LaAl}_{0.67-x}\text{Ca}_x\text{Mn}_{0.33}\text{O}_3$  ceramics.

The plot of  $\tan\delta_M$  as a function of frequency is shown in Fig. 5.12 (b). It is observed that  $\tan\delta_M$  decreases with increasing frequency and remains constant after 1 MHz frequency. The decrease of  $\tan\delta_M$  with frequency might be attributed to spin inversion losses as suggested by Gama and Rezende [30] or due to the reduction of activity of space charges because space charges cannot follow the rapid variation of the field at high frequency. The values of  $\tan\delta_M$  for all the compositions are found decreasing very significantly and it may be due to the reduction of imperfection after the addition of Ca.

The Relative quality factor (RQF) is generally used as a measure of performance of materials for real world applications. The variation of RQF with frequency of the studied compositions is illustrated in Fig. 5.13. It is evident that the value of RQF increases with the increase in frequency for all the compositions. This implies that with the increase in frequency the utility of the studied compositions is enhanced.

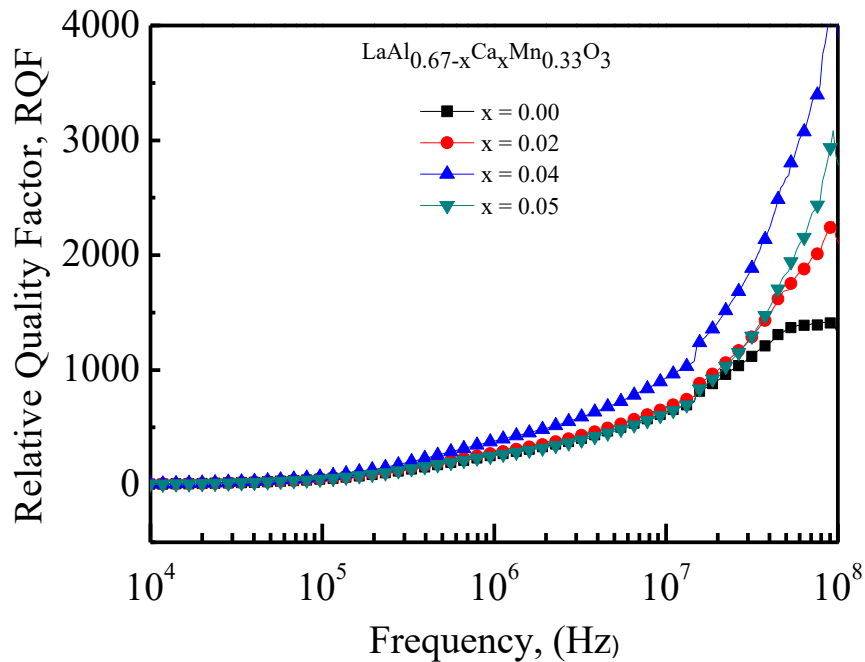


Fig. 5.13: The variations of Relative Quality factors ( $Q$ -factor) with frequency of various  $\text{LaAl}_{0.67-x}\text{Ca}_x\text{Mn}_{0.33}\text{O}_3$  ceramics.

**References**

- [1] Mansour, Al-Haj, “X-ray diffraction and magnetization studies of BiFeO<sub>3</sub> multiferroic compounds substituted by Sm<sup>3+</sup>, Gd<sup>3+</sup>, Ca<sup>2+</sup>”, *Cryst. Res. Technol.*, Vol. 45, pp. 89-93, 2010.
- [2] Lima, E., Villafuerte-Castrejón, M.E., Saniger, J., Lara, V., Sánchez-Sánchez, J.E. and Javier Álvarez, L., “Lanthanum influence on EuAlO<sub>3</sub> perovskite structural properties: Experimental and molecular dynamics studies”, *Advances in Materials Science and Engineering*, 2012.
- [3] Luo, T., Liu, Z., Zhang, F. and Li, Y., “Colossal permittivity and the polarization mechanism of (Mg, Mn) co-doped LaGaO<sub>3</sub> ceramics”, *Journal of Applied Physics*, 123(12), p.124108, 2018.
- [4] Uniyal, P., Lotey, G.S., Gautam, A., Verma, N.K. and Yadav, K.L., “Multiferroic Properties of (Bi<sub>0.9</sub>Gd<sub>0.1</sub>FeO)<sub>1-x</sub>(BaTiO<sub>3</sub>)<sub>x</sub> Ceramics”, *Journal of Superconductivity and Novel Magnetism*, 27(2), pp.569-574, 2014.
- [5] Sattar, A.A., El-Sayed, H.M., El-Shokrofy, K.M. and El-Tabey, M.M., “Improvement of the magnetic properties of Mn-Ni-Zn Ferrite by the non magnetic Al-Ion substitution”, *J. Appl. Sci.*, vol. 5(1), pp. 162-168, 2005.
- [6] Shao, H., Liu, Z., Jian, G., Ma, M. and Li, Y., “Effects of Mn<sup>2+</sup> doping on the microwave dielectric properties of Ti<sub>1-x</sub>Cu<sub>x/3</sub>Nb<sub>2x/3</sub>O<sub>2</sub> ceramics”, *Ceramics International*, 43(16), pp.13895-13900, 2017.

- [7] Angadi VJ, Choudhury L, Sadhana K, Liu HL, Sandhya R, Matteppanavar S, et al. “Structural, electrical and magnetic properties of Sc<sup>3+</sup> doped Mn-Zn ferrite nanoparticles”, *J Magn Magn Mater*; 424:1–11, 2017.
- [8] Koops, C.G., “On the dispersion of resistivity and dielectric constant of some semiconductors at audio frequencies”, *Phys. Rev.*, vol. 83(1), pp. 121, 1951.
- [9] Maxwell, J. C. *Electricity and Magnetism*. Oxford University Press, London, 1973.
- [10] Wagner, K.W., “Zur theorie der unvollkommenen dielektrika,” *Ann. Phys.*, vol. 345(5), pp. 817-855, 1913.
- [11] Buscaglia, M. T., Buscaglia, V., Viviani, M., Nanni, P., and Hanuskova, M., “Influence of foreign ions on the crystal structure of BaTiO<sub>3</sub>”, *J. Euro. Ceram. Soc.*, **20**, 1997-2007, 2000.
- [12] Parkash, O., Kumar, D., Dwivedi, R. K., Srivastava, K. K., Singh, P., and Singh, S., “Effect of simultaneous substitution of La and Mn on dielectric behavior of barium titanate ceramic”, *J. Mater. Sci.*, **42**, 5490-5496, 2007.
- [13] Jonscher, A. K., “The ‘universal’ dielectric response”, *Nature*, Vol. 267, pp. 673-679, 1977.
- [14] Maxwell, J. C., “A Treatise on Electricity and Magnetism”, Clarendon Press, Oxford, 1982.
- [15] Wagner, K., “On the theory of imperfect dielectrics”, *J. Ann. Phys.*, Vol. 40, pp.817-855, 1913.
- [16] Austin, I. G. and Mott, N. F., “Polarons in crystalline and non-crystalline materials”, *Adv. Phys.*, Vol. 18, pp. 41–103, 1969.

- [17] Khandekar, M. S., Kambale, R. C., Patil, J. Y., Kolekar, Y. D. and Suryavanshi, S. S., “Effect of calcination temperature on the structural and electrical properties of cobalt ferrite synthesized by combustion method”, *J. Alloy. Compd.*, Vol. 509, pp. 1861-1865, 2011.
- [18] Behera, B., Nayak, P. and Choudhary, R. N. P., “Structural and electrical properties of  $\text{KCa}_2\text{Nb}_5\text{O}_{15}$  ceramics”, *Cent. Eur. J. Phys.*, Vol. 6, pp. 289-295, 2008.
- [19] Plocharski, J. and Wieczorek, W., “Electrochemical stability and ionic conductivity of some polymerlic based electrolytes”, *Solid State Ion.*, Vol. 28–30, pp. 979-983, 1988.
- [20] Kaiser, M., “Electrical conductivity and complex electric modulus of titanium doped nickel–zinc ferrites”, *Physica B*, vol. 407, pp. 606-613, 2012.
- [21] Choudhary, R. N. P., Pradhan, D. K., Tirado, C. M., Bonilla, G. E. and Katiyar, R. S., “Effect of La substitution on structural and electrical properties of  $\text{Ba}(\text{Fe}_{2/3}\text{W}_{1/3})\text{O}_3$  nanoceramics”, *J. Mater. Sci.*, vol. 42, pp. 7423-7432, 2007.
- [22] Macedo, P. B., Moynihan, C. T. and Bose, R., “The conductivity of the super ionic glass samples increases after irradiation and conductors”, *Phys. Chem. Glasses*, Vol. 13, pp. 171-179, 1972.
- [23] Pandey, L., Katare, R., Parkash, O., and Kumar, D., “Evidence of two ferroelectric PTCR components in valence-compensated ceramic system  $\text{Ba}_{1-x}\text{La}_x\text{Ti}_{1-x}\text{Co}_x\text{O}_3$ ”, *Bul. Mater. Sci.*, **20**, 933-947, 1997.
- [24] Yu, M., Hu, J., Liu, J. and Li, S., “Electromagnetic properties of multiferroic magnetoelectric  $\text{BaTiO}_3\text{-Co}_x\text{Fe}_{3-x}\text{O}_4$  core–shell particles obtained by homogeneous coprecipitation”, *J. Magn. Magn. Mater.*, Vol. 326, pp. 31-34, 2013.



- [25] Kumar, P., Sharmab, S. K., Knobel, M. and Singh, M., “Effect of  $\text{La}^{3+}$  doping on the electric, dielectric and magnetic properties of cobalt ferrite processed by co-precipitation technique”, *J. Alloy. Compd.*, Vol. 508, pp. 115-118, 2010.
- [26] Verma, A. and Chatterjee, R., “Effect of zinc concentration on the structural, electrical and magnetic properties of mixed Mn–Zn and Ni–Zn ferrites synthesized by the citrate precursor technique”, *J. Magn. Magn. Mater.*, Vol. 306, pp. 313-320, 2006.
- [27] Mahmud, S.T., Hossain, A. K. M. A., Hakim, A. K. M. Abdul, Seki, M., Kawai, T. and Tabata, H., “Influence of microstructure on the complex permeability of spinel type Ni–Zn ferrite”, *J. Magn. Magn. Mater.*, Vol. 305, pp. 269–274, 2006.
- [28] Jun, Hu and Mi, Yan, “Preparation of high permeability Ni-Cu-Zn ferrite”, *J. Zhejiang Univ. Sci.*, Vol. 6B (6), pp. 580-583, 2005.
- [29] Tsutaoka, T., Ueshima, M., Tokunaga, T., Nakamura, T. and Hatakeyama, K., “Frequency dispersion and temperature variation of complex permeability of Ni-Zn ferrite composite materials”, *J. Appl. Phys.*, Vol. 78(6), pp. 3983-3991, 1995.
- [30] Gama, A. M. and Rezende, M. C., “Complex permeability and permittivity variation of radar absorbing materials based on MnZn ferrite in microwave frequencies”, *Mat. Res.*, Vol. 16, pp. 997-1001, 2013.

## CHAPTER 6

### CONCLUSIONS

The present research work mainly deals with the investigation of structural, dielectric and electrical properties of (Ca, Mn) co-doped LaAlO<sub>3</sub> ceramics. The disk-shaped and toroid shaped samples prepared by the standard solid state reaction technique were sintered at 1723 K for 5 h. Different experiments were carried out and the results were carefully analyzed to monitor the changes in structure, dielectric and electrical properties of the samples. This chapter presents a concise summary based on the results and discussion presented in the previous chapter and also suggests the scope for the further work.

The conclusions drawn from the present investigations are as follows:

#### 6.1 Conclusions

- The polycrystalline samples of LaAl<sub>0.67-x</sub>Ca<sub>x</sub>Mn<sub>0.33</sub>O<sub>3</sub> (x=0.00, 0.02, 0.04, 0.05) have been successfully synthesized by the standard solid state reaction technique.
- The XRD results indicate that all samples are of single phase perovskite structure and no trace of second phase is found.
- The XRD patterns are in good agreement with a rhombohedrally distorted perovskite structure which is equivalent to hexagonal symmetry.
- The lattice parameters 'a' and 'c' of various LaAl<sub>0.67-x</sub>Ca<sub>x</sub>Mn<sub>0.33</sub>O<sub>3</sub> increase with the increase in Ca content.
- The value of both  $\rho_x$  and  $\rho_B$  decreased with the addition of Ca in LaAlO<sub>3</sub> ceramics. The value of  $\rho_x$  was found to be higher than that of  $\rho_B$ . Density decreased with the addition of Ca content which might be attributed to the fact that the molecular weight.

- Microstructure of the ceramics was observed by FESEM, For the sample ( $x= 0.00$ ) the liquid phase seemed to appear in the grain boundary due to the formation of low melting point manganese containing an intermediate compound during sintering. The average grain size are found to increase for ( $x= 0.02, 0.04$ ) with the increase in Ca content due to difference in ionic radii but for ( $x= 0.05$ ) the average grain size decreases because in this case significant amount of  $\text{Ca}^{2+}$  reside at the grain boundaries.
- The variation of dielectric constant ( $\epsilon'$ ) was measured at room temperature in the frequency range 20 Hz to 120 MHz. At lower frequencies, the higher values of  $\epsilon'$  are observed due to the contributions from all four mechanisms of polarization to the total polarization.  $\text{LaAl}_{0.67-x}\text{Ca}_x\text{Mn}_{0.33}\text{O}_3$  ceramics shows colossal permittivity up to frequency  $10^6$  Hz and then starts decreasing and becomes independent of frequency for all of the compositions. This phenomenon can be explained by the Koops theory based on Maxwell–Wagner model.
- The values of dielectric loss tangent ( $\tan\delta_E$ ) sharply decrease as frequency increases in the low frequency region. While in the high frequency region,  $\tan\delta_E$  increases with the increase in frequency. However, in the intermediate frequencies, the values of  $\tan\delta_E$  are minimum which indicates that the compositions are of good quality material in this range.
- The value of  $Z'$  gradually decreases with increasing frequency up to a certain limiting frequency ( $\approx 10^4$  Hz). The decrease in  $Z'$  indicates that the conduction is increasing with frequency and above this frequency ( $\approx 10^4$  Hz) it becomes almost frequency independent. The variation of  $Z''$  with frequency exhibits a peak at all compositions. The relaxation peak is found shifting towards higher frequency with the increase of Ca content.

- The real part of modulus ( $M'$ ) is found to be very low (nearly zero) at low frequencies and it increases with the increase in frequency and The variation of imaginary part of electric modulus ( $M''$ ) with frequency, it exhibits a peak at the frequency above  $10^3$  Hz.
- The complex impedance plot (i.e a plot drawn between imaginary ( $Z''$ ) and real parts ( $Z'$ ) of the impedance) exhibits a single semicircular arc of all the compositions of  $\text{LaAl}_{0.67-x}\text{Ca}_x\text{Mn}_{0.33}\text{O}_3$  ceramics. The absence of second semicircle in the complex impedance plots indicates that the materials have only grain boundary effect to the conductivity mechanism.
- The ac-conductivity ( $\sigma_{ac}$ ) at lower frequency is found almost constant whereas after a certain frequency ( $>10^4$  Hz)  $\sigma_{ac}$  increases very fast.
- The value of  $\mu'_i$  for all the compositions remains almost constant up to certain frequency and then decreases with increasing frequency. In the present case, variation of the initial permeability is strongly influenced by its grain size and  $P$ . It is observed that  $\tan \delta_M$  decreases with increasing frequency and remains constant after 1 MHz frequency. The decrease of  $\tan \delta_M$  with frequency due to the reduction of activity of space charges because space charges cannot follow the rapid variation of the field at high frequency. The Relative quality factor (RQF) implies that with the increase in frequency the utility of the studied compositions is enhanced.

## 6.2 Recommendations for the further work

Following recommendations are made for further extension of the present work:

- Ferroelectric, piezoelectric and pyroelectric characterization of the samples may be studied.
- Investigation of temperature dependent electromagnetic properties.
- Transmission electron micrographs (TEM) analysis may be studied for proper understanding of the domain.
- Other preparation techniques (e.g., sol-gel, co-precipitation and auto-combustion etc.) may be followed to prepare the samples for comparing the properties of the present study.